# Measurement of the exit characteristics of light from optical multimode plastic fibres

von
Simon Nieswand

Masterarbeit in Physik

vorgelegt der

Fakultät für Mathematik, Informatik und Naturwissenschaften

der Rheinisch-Westfälischen Technischen Hochschule Aachen

Dezember 2014

Erstellt im

III. Physikalischen Institut A

Univ.-Prof. Dr. Thomas Hebbeker

Erstgutachter

Univ.-Prof. Dr. Thomas Hebbeker
III. Physikalisches Institut A
RWTH Aachen

Zweitgutachter

PD Dr. Oliver Pooth
III. Physikalisches Institut B
RWTH Aachen

## Zusammenfassung

Optische Multimode-Kunststofffasern sind wesentlicher Bestandteil vieler Detektoren, welche in modernen Teilchenphysik-Experimenten verwendet werden. Um eine effiziente Faserauslese mit minimalen Verlusten der in der Regel geringen Mengen an gesammeltem und transportiertem Licht zu gewährleisten, müssen die Eigenschaften des am Ende der Faser austretenden Lichts bestimmt und verstanden werden. Zu diesem Zweck wurden im Rahmen dieser Arbeit zwei Messaufbauten entwickelt. Eine dieser Aufbauten ermöglicht die Vermessung der räumlichen Verteilung des Faserlichts bei minimalen Abständen von bis zu etwa $10\,\mu$m von der Faser-Endfläche. Der zweite Aufbau wird verwendet, um den Lichtaustritt unter Austrittswinkeln zwischen 0° und 90° mit einer Winkelakzeptanz von 2° zu untersuchen. Der Aufbau der Versuchsanordnungen und die Messergebnisse für Fasern mit sowohl runder als auch quadratischer Querschnittsfläche und unterschiedlicher Anzahl von Faser-Claddings werden in dieser Arbeit vorgestellt.
Die Messergebnisse wurden des Weiteren mit Faser-Simulationen verglichen, welche mithife einer spezialisierten Simulations-Software für Geant4 erstellt wurden. Es wird gezeigt, wie dieser Vergleich zur Überprüfung und Verbesserung der Funktionsweise des Software-Packets genutzt wurde.

## Abstract

Optical multimode plastic fibres are an essential part of many detectors used in modern particle physics experiments. To assure an efficient fibre readout with minimal losses of the usually small amounts of light collected and propagated inside the fibres, one has to determine and understand the light exit characteristics at the fibre end. For this purpose, two experimental setups were developed in the course of this thesis. One of the setups allows the measurement of the spatial fibre light distribution at a distance down to approximately $10\,\mu$m from the fibre end surface. The other setup is used for the examination of the fibre light output at different exiting angles. With the help of this setup, the angular light distribution for angles between 0° and 90° can be examined with an acceptance of 2°. The design of the experimental setups as well as the measurement results for round and square multimode fibres with different numbers of claddings are presented in this thesis.
It is further shown how a comparison of the measured results to simulated data obtained with a specialised toolkit for Geant4 was used to verify and improve the functionality of the simulation software.

# Contents

# 1 Introduction

In order to deepen our understanding of the laws of nature, experimental and theoretical physicists all over the world work together to develop and test new theories using observations made with the help of many different modern particle physics experiments. Those are designed to search for hints of new physics phenomena.
The detectors in those setups often make use of different types of optical plastic fibre: The detector itself may consist - partially or as a whole - of scintillating fibres which emit light after being permeated by charged particles. An example for such a detector can be seen in figure 1.1 which shows the a layer cross section of the Electromagnetic Calorimeter of the AMS-02 experiment composed of scintillating fibre layers embedded in lead [1].

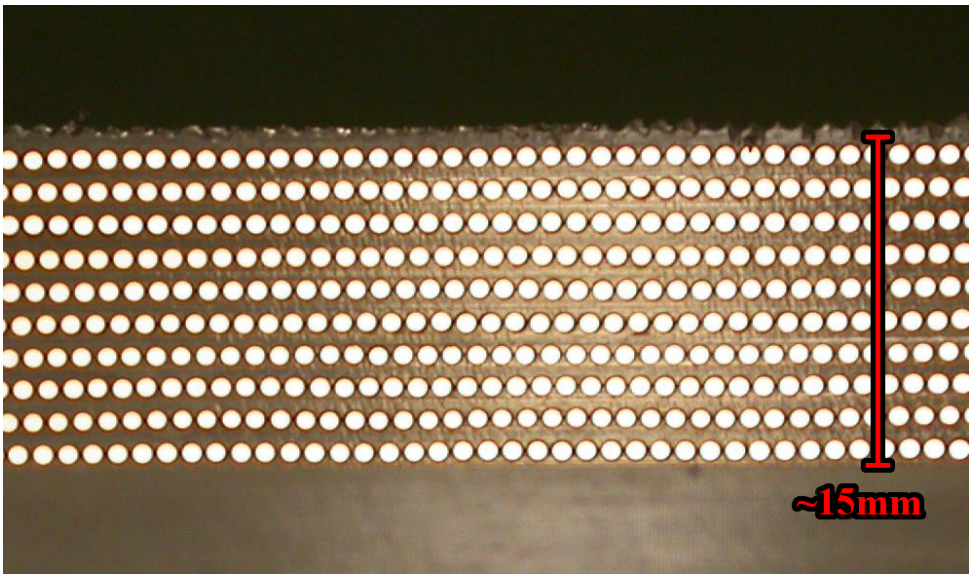


**Figure 1.1:** Cross section of a layer of the electromagnetic calorimeter used in the AMS-02 experiment. It consists of scintillating fibres embedded in lead. Image taken from [1].

So called wavelength-shifting (WLS) fibres are used to collect light from one or more detectors and - as the name implies - shift its wavelength to another region of the spectrum. Figure 1.2 shows four loops of WLS fibre attached to a scintillator tile as it is used in the Hadron Outer Calorimeter of the CMS experiment at the Large Hadron Collider (LHC) [2].
Finally, clear optical fibres are used for the transport of collected light from the detector to a readout sensor which allows a separation of those two components.

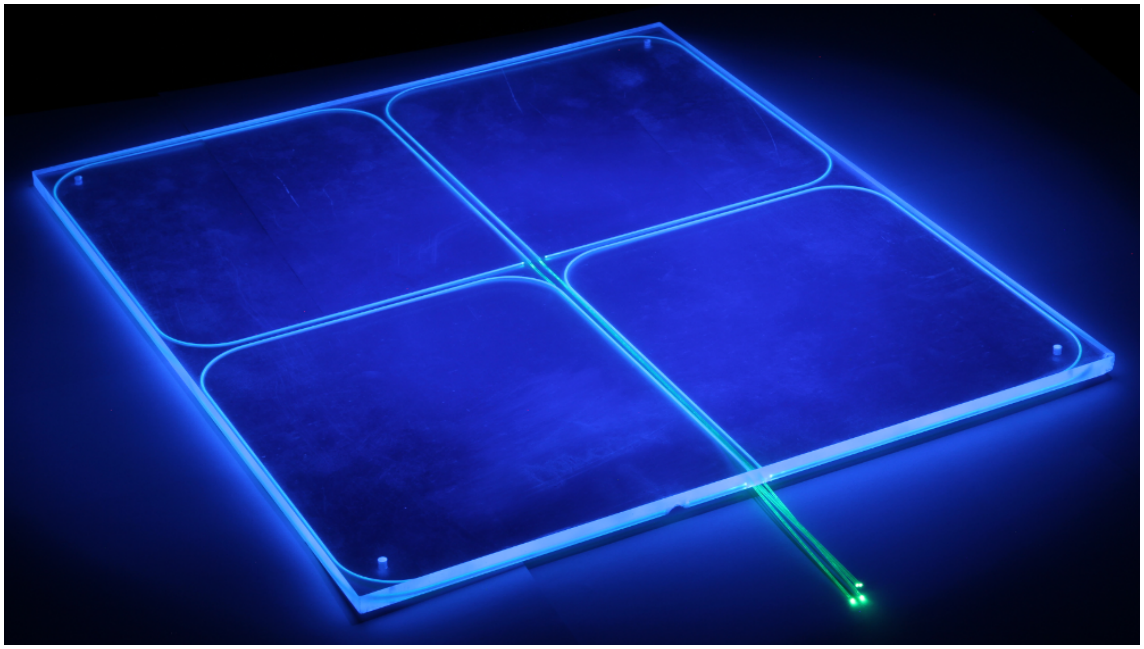

**Figure 1.2:** Looped WLS fibres on a scintillator tile from the Hadron Outer Calorimeter of the CMS experiment [3].

Optical fibres are typically made out of glass or plastic. Plastic fibres are often preferred, if light in the visible spectrum is to be collected and transported. In contrast to glass fibres, they are cheaper, more durable and easier to handle and assemble. However, their main advantage is that even with a large fibre diameter in the order of millimetres - which is needed to collect a maximum of energy from passing particles or light from an adjoining scintillator - plastic fibres are flexible and their shape may be adapted to the respective detector's dimensions (see fig. 1.2).

The light signals transported by optical fibres are detected and measured with the help of photo sensitive sensors. Commonly used photon detectors are silicon photomultipliers (SiPMs). An SiPM (see fig. 1.3) consists of an array of avalanche photo-diodes (called cells) operated in Geiger-mode [5, 6]. In this mode, the reverse bias voltage attached to the diodes is sufficient for both electron- and hole-induced avalanches. This allows for the counting of single photons. However, in Geiger-mode each cell works digitally meaning that one, two or even more photons hitting one cell simultaneously produce the same signal and therefore cannot be distinguished.
For an efficient readout of optical fibres with SiPMs, it is therefore important that the light from the fibre illuminates all SiPM cells as homogeneously as possible. Thus, the possibility of multiple cell hits is reduced and the dynamic range of the SiPM signal (which is the sum over all cell signals) is maximized. Therefore, the spatial light distribution at the fibre end surface has to be determined. With this knowledge, light mixers for an optimal

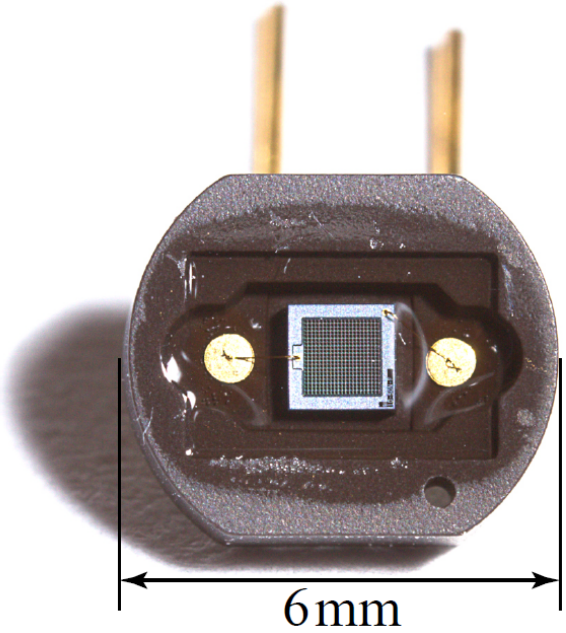


**Figure 1.3:** Photo of a Hamamatsu SiPM (model: S10362-100C) with 900 digitally working cells (single photon detection possible) on an 1 mm$^2$ active area. Taken from [4].

coupling of the fibre to a given detector can be designed or may be rendered unnecessary. Especially for the detection of small light signals, the readout efficiency benefits from the omission of light mixers, since those could lead to a signal attenuation.
The angular distribution of the light has to be taken into account, too. Photons that exit a fibre at large angles might miss the readout sensor if there is a gap between fibre end and sensor. A protective resin covering the sensor's active area could create such a gap. The angular light distribution is further important when considering that the photon detection efficiency (PDE) of the readout sensor might depend on the incidence angle of the detected photons. It was shown in [7] that for an SiPM manufactured by Hamamatsu the relative PDE deceeds 90% for incidence angles larger than 75°. This renders the SiPM partially blind for those photons and diminishes the readout efficiency.

Studies on the spatial light distribution of optical fibres were performed by Baumbaugh et. al. [8]. The published results[1] show a fairly homogeneous light distribution for one of the measured fibres (see fig. 1.4). However, this data was obtained using a CCD sensor approximately 500 $\mu$m away from the fibre end. This gap causes a dispersion of the light distribution between fibre and CCD. The obtained spatial distribution does therefore not represent the actual conditions at the fibre end. In addition, the angular light distribution

[1] Unfortunately, it seems that not a lot of research has been done on this topic and the shown plot - however bad its quality might be - represents the only usable research results.

was not measured which prevents a reconstruction of the actual spatial distribution.

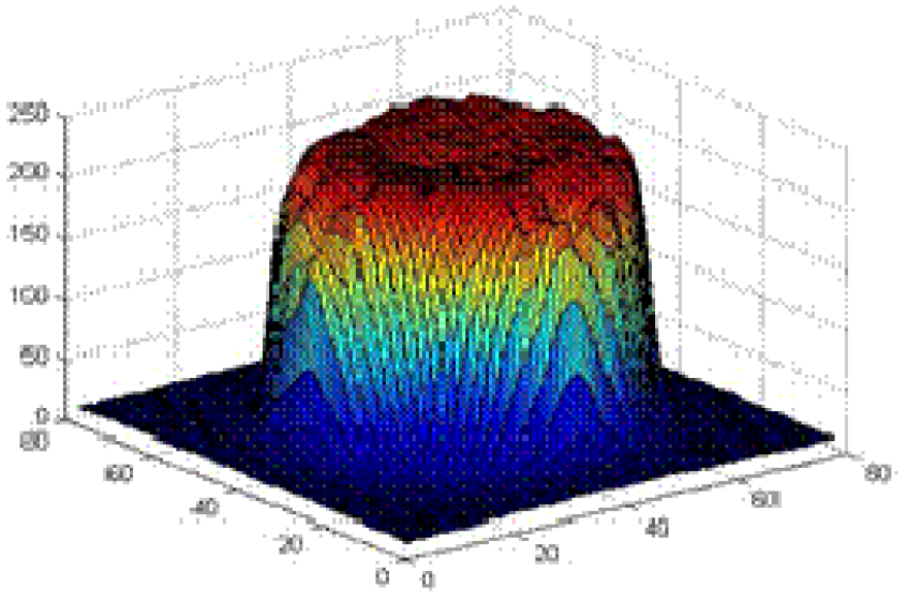


**Figure 1.4:** Spatial light distribution in arbitrary units on a CCD sensor approx. 500 $\mu$m away from the end of a round optical fibre (manufacturer: Kuraray). Plot taken from [8].

For a more precise measurement of the spatial and angular distribution of light exiting optical fibres, two setups were constructed in the course of this thesis. They were then used to study optical multimode fibres of different types and geometries.

The measured results were further compared to simulated data obtained using the GODDeSS[2] package for the Geant4 toolkit [9]. GODDeSS was developed to supply physicists with helpful tools to design and simulate scintillator tiles and optical fibres inside the Geant4 framework [10]. Since a reliable detector simulation is an essential part of every modern particle physics experiment, it is necessary for each part of the simulation to work correctly. The comparison between simulated and measured data was conducted to assure a proper functionality of the fibre simulation in GODDeSS.

This thesis continues with a closer look at the light propagation inside optical fibres in chapter 2. In chapter 3 the developed experimental setups are presented. It follows the description of the data acquisition and analysis in chapter 4. The results of the comparison between measurements and simulation are shown in chapter 5. Finally, chapter 6 contains a summarising conclusion of this thesis and gives a short outlook on possible improvements and further applications of the developed setups.

[2]Geant4 Objects for Detailed Detectors with Scintillators and SiPMs. URL: https://forge.physik.rwth-aachen.de/projects/goddess-package

# 2 Optical Multimode Plastic Fibres

Since optical fibres use total internal reflection to trap and propagate light, this phenomenon is explained in the first section of this chapter. Following, the basic design and the different types of optical fibres are introduced in section 2.2. The closing section describes the propagation characteristics of light in fibres with different geometrical properties.

## 2.1 Total Internal Reflection

When a ray of light transits from one medium into another, its direction will change dependent on the incident angle $\alpha_{\text{in}}$ between light ray and the interface normal and the refractive indices of the two media $n_{\text{in}}$ and $n_{\text{out}}$ (see fig. 2.1a).

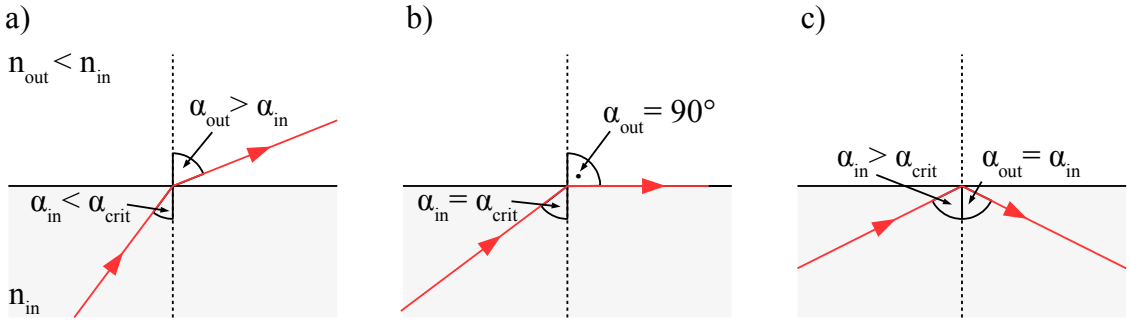


**Figure 2.1:** Schematics of light propagation at the interface between to media with different refractive indices $n_{\text{in}}$ and $n_{\text{out}} < n_{\text{in}}$. For steep incidence angles $\alpha_{\text{in}}$, the light ray transits into the second medium at an angle $\alpha_{\text{out}} > \alpha_{\text{in}}$ (a). For angles exceeding the critical angle $\alpha_{\text{crit}}$ for total internal reflection (b) the ray is reflected back into the medium at $\alpha_{\text{out}} = \alpha_{\text{in}}$ (c).

The deflection is given by Snell's law [11]:

$$n_{\text{in}} \cdot \sin(\alpha_{\text{in}}) = n_{\text{out}} \cdot \sin(\alpha_{\text{out}}) \Leftrightarrow \alpha_{\text{out}} = \arcsin\left(\frac{n_{\text{in}}}{n_{\text{out}}} \cdot \sin(\alpha_{\text{in}})\right) \quad . \tag{2.1}$$

If $n_{\text{out}}$ is lower than $n_{\text{in}}$, the ray will be deflected away from the interface normal ($\alpha_{\text{out}} > \alpha_{\text{in}}$). For incidence angles large enough, $\alpha_{\text{out}}$ exceeds 90° and the ray of light is reflected back into the outgoing medium with $\alpha_{\text{out}} = \alpha_{\text{in}}$ (see fig. 2.1b and c). The reflectance - the percentage of the ray's amplitude that is reflected at the interface - is 100% for those rays. This phenomenon is called total internal reflection (TIR). The critical angle $\alpha_{\text{crit}}$ for TIR can be calculated using eq. 2.1 and $\sin(\alpha_{\text{out}} = 90°) = 1$:

$$n_{\text{in}} \cdot \sin(\alpha_{\text{crit}}) = n_{\text{out}} \cdot \sin(90°) \Leftrightarrow \alpha_{\text{crit}} = \arcsin\left(\frac{n_{\text{out}}}{n_{\text{in}}}\right) \quad . \tag{2.2}$$

All rays with steeper incidence angles will only be reflected partially. Their reflectance $R$ is described by the Fresnel equation for unpolarised light at an interface between two media:

$$R = \frac{R_{\parallel} + R_{\perp}}{2} \tag{2.3}$$

with

$$R_{\parallel} = \left|\frac{n_{\text{out}} \cdot \cos(\alpha_{\text{in}}) - n_{\text{in}} \cdot \cos(\alpha_{\text{out}})}{n_{\text{out}} \cdot \cos(\alpha_{\text{in}}) + n_{\text{in}} \cdot \cos(\alpha_{\text{out}})}\right|^2 \tag{2.4}$$

and

$$R_{\perp} = \left|\frac{n_{\text{in}} \cdot \cos(\alpha_{\text{in}}) - n_{\text{out}} \cdot \cos(\alpha_{\text{out}})}{n_{\text{in}} \cdot \cos(\alpha_{\text{in}}) + n_{\text{out}} \cdot \cos(\alpha_{\text{out}})}\right|^2 \tag{2.5}$$

being the reflectance of light polarised parallel and perpendicular to the plane of incidence [11]. Considering that light transport in optical fibres is achieved by many internal reflections, rays that only get reflected partially will not propagate (long) inside the fibre due to repeated transmission losses at each reflection.

## 2.2 Basic Design and Types of Optical Multimode Plastic Fibres

A basic optical plastic fibre consists of two components: the fibre core and one or more claddings. The fibre geometry governs the light propagation inside the fibre and is given by fibre shape, diameter, and the number of claddings. The cross section usually has either a round or a square shape. Figure 2.2 shows schematics of two fibres with different geometries.

The core is usually a long polystyrene (PS) or polymethylmethacrylate (PMMA) strand. For core diameters much larger than the wavelength of the transported light a large variety of light modes can be propagated. Those fibres are therefore called multimode fibres. Their core diameter typically ranges between 50 $\mu$m and 2 mm. In this case, limitations on the propagable modes due to the wavelike nature of light can be neglected and the trajectory of light inside the fibres can be described in a good approximation using geometrical optics.

A cladding is a layer surrounding the fibre core with a thickness of typically a few percent of the fibre radius. Its refractive index $n_{\text{clad}}$ is lower than $n_{\text{core}}$. Typical materials for claddings of plastic fibres are PMMA or fluorinated polymer (FP). An optical fibre may have multiple claddings each with a lower refractive index than the underlying one. The claddings provide interfaces with decreasing refractive indices allowing repeated TIR which is used to confine and propagate light inside fibre. Fibres with only one cladding are called singleclad fibres while those with additional claddings are referred to as multiclad fibres.

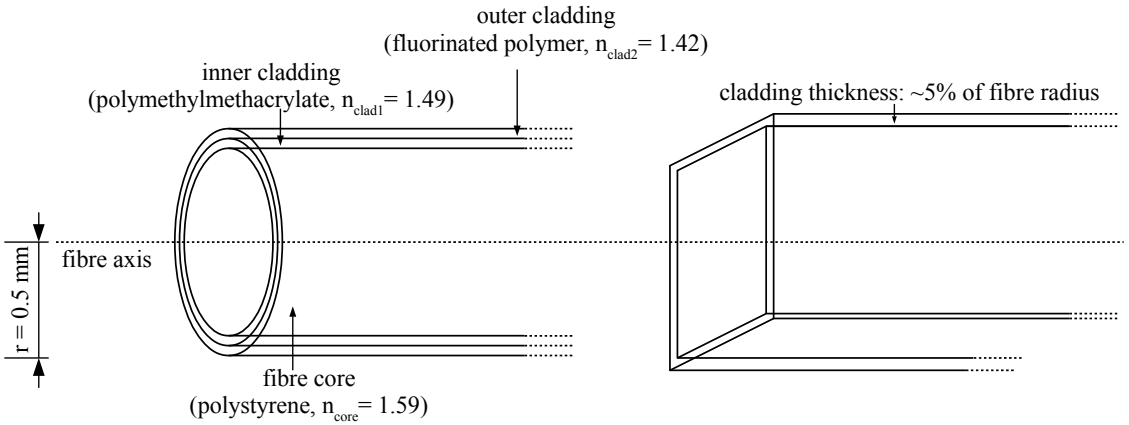


**Figure 2.2:** Schematics of a round multiclad fibre (left) as well as a square singleclad fibre (right). The presented materials, refractive indices and dimensions are typical for plastic multimode fibres.

In this thesis, multiclad always relates to fibres with two claddings.
There a three types of optical fibre sharing this fundamental design: standard light guides, scintillating fibres and wavelength-shifting (WLS) fibres. The difference between those types is their application in particle detectors and how light is coupled into the fibre.
As the name implies, light guides or light guiding fibres are used to transport light signals from one end of the fibre to the opposing one. They usually have an attenuation length in the order of $15 - 30\,\mathrm{m}$ which is longer than for the other two fibre types [12]. For those, a typical value for the attenuation length is $3.5\,\mathrm{m}$ [13, 14]. For light guides, the light is coupled directly into the fibre through one of the end surfaces (see fig. 2.3). As figure 2.4 shows, light guides are not able to trap light inside the fibre if it enters through the cladding, because TIR cannot be achieved at the opposing core-cladding interface.

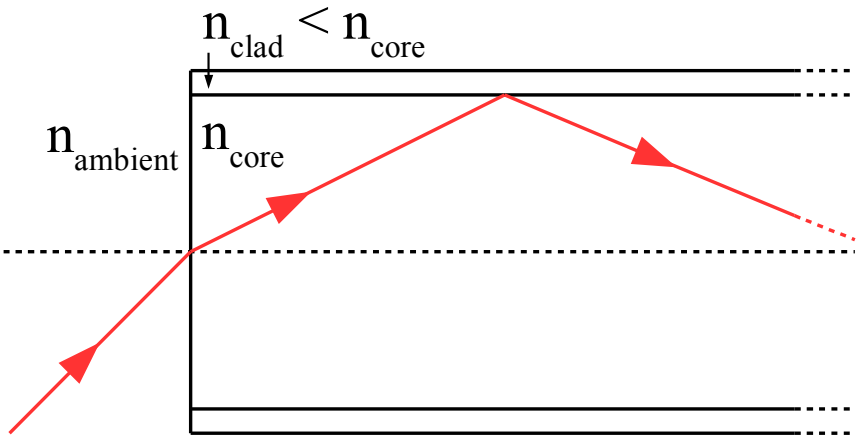


**Figure 2.3:** Example of light coupling at the fibre end surface of a light guiding fibre.

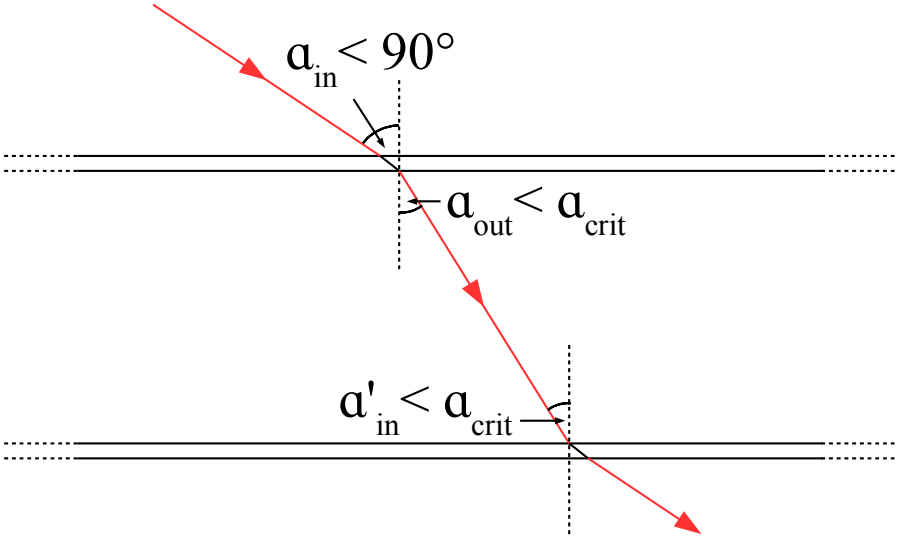


**Figure 2.4:** Schematic of a light ray entering a light guiding fibre through the cladding and leaving at the opposing side since TIR cannot be achieved.

Scintillating fibres detect the passage of charged particles or photons and guide the induced light towards a photon detector or a light guiding fibre. To do so, their core is doped with an organic scintillating material. It consists of aromatic molecules with one or more carbon ring structures called benzene rings. The rings contain de-localised electrons in $\pi$-orbitals. Those electrons can be easily excited by charged particles or photons. The de-excitation of the electrons happens under isotropic emission of scintillation photons [15, 16].
Figure 2.5 shows the indirect coupling of light into a scintillating fibre. Only a fraction of the scintillation light can be trapped inside the fibre via TIR. This fraction corresponds to the trapping efficiency of a fibre. Typical values for multimode fibres with a diameter of 1 mm are about 5 % for round fibres and approximately 4 % for square ones [13].
Finally, WLS fibres are used to collect light from an adjoining detector and guide it towards a readout sensor or a light guide. They are therefore usually embedded into the detector material. Similar to scintillating fibres, the light is induced indirectly into the fibre. In this case, the core is doped with fluorescing molecules absorbing the photons from the detector. After non-radiative transitions, the de-exciting electrons emit isotropically distributed photons of a greater wavelength and, therefore, lower energy [17]. If a fluorescence photon is not trapped inside the fibre and re-enters the adjoining detector, the wavelength shift prevents an undesired further excitation of the detector (optical crosstalk). Furthermore, the absorption through the fluorescing dopant renders the WLS fibre untransparent for the light from the detector. This prevents an interference[1] with the wavelength-shifted signal at the fibre readout.

[1] Here, interference is meant in the sense of creating a background signal, not optical.

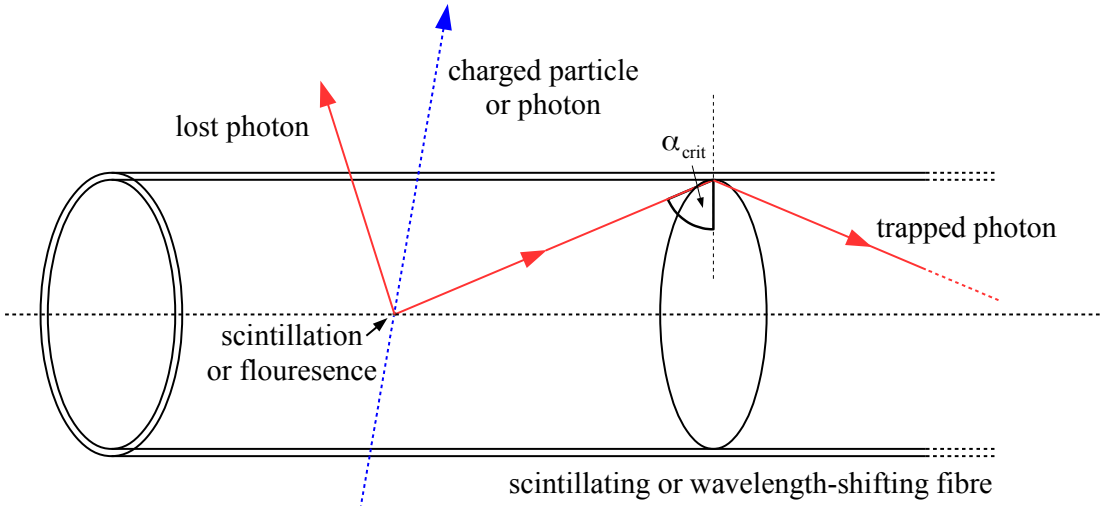


**Figure 2.5:** Schematic of indirect light coupling into a scintillating or wavelength-shifting fibre. Scintillation or fluorescence photons are emitted caused by the passage of a charged particle or photon through the fibre core. They are trapped inside the fibre if there incidence angle at the core-cladding interface is larger than the critical angle $\alpha_{\text{crit}}$ for total internal reflection (cf. 2.1).

## 2.3 Light Propagation and Exit Characteristics

### 2.3.1 Round Fibres

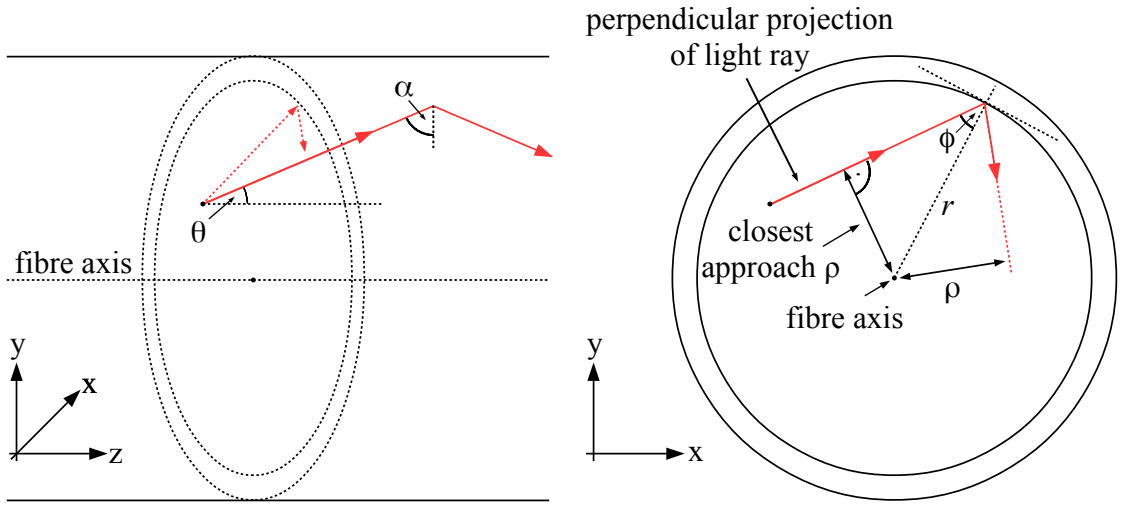


**Figure 2.6:** Schematic of a light ray inside a round optical fibre. The left image shows the polar angle $\theta$ of the ray as well as the incidence angle $\alpha$ at the core-cladding interface. The right image presents a projection of the ray in a plane perpendicular to the fibre axis and features the construction of the ray's closest approach $\rho$ to the fibre centre and the corresponding perpendicular incidence angle $\phi$. Note hat $\alpha$ is a combination of both $\theta$ and $\phi$ (see eq. 2.7).

Light rays inside round fibres can be described by their polar angle $\theta$ towards the fibre axis and their minimal approach $\rho$ towards the fibre center (see fig. 2.6). $\rho$ determines the perpendicular component $\phi$ of the incidence angle which is given by

$$\sin(\phi) = \frac{\rho}{r} \tag{2.6}$$

with $r$ being the radius of the fibre core.
The component of the incidence angle parallel to the fibre axis is simply $90° - \theta$. The combined incident angle $\alpha$ can be calculated using equation 2.7 [18].

$$\cos(\alpha) = \sin(\theta) \cdot \cos(\phi) = \sin(\theta) \cdot \sqrt{1 - \left(\frac{\rho}{r}\right)^2} \quad . \tag{2.7}$$

The rays of light are divided into two classes: meridional rays and skew rays. They are depicted in figure 2.7.

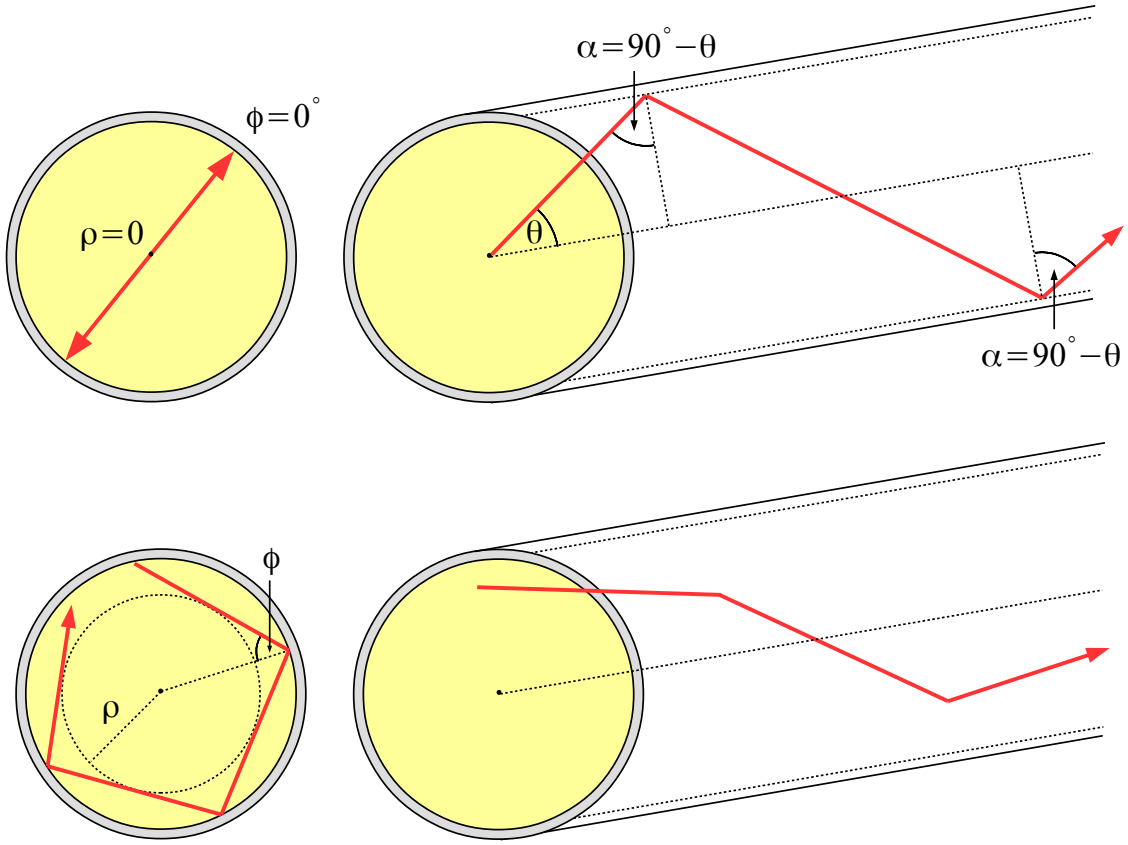


**Figure 2.7:** Propagation of meridional rays (top) and skew rays (bottom) in round optical fibres. It can be seen that meridional rays propagate inside a constant plane while skew rays spiral along the fibre. Figures adopted from [18].

Meridional rays cross the fibre axis ($\rho = 0$) which leads to a perpendicular incidence angle of $\phi = 0°$. Therefore, they propagate inside a constant plane parallel to the fibre axis.

Skew rays, in contrast, spiral along the fibre with a minimal approach $\rho \neq 0$ to the fibre centre and a constant perpendicular incidence angle $\phi \neq 0°$.

The propagation of light rays inside the fibre core (so-called core modes) is limited by the critical angle $\alpha_{\text{crit}}^{\text{core}}$ for TIR at the core-cladding interface. Considering eq. 2.2, the critical angle is given by

$$\alpha_{\text{crit}}^{\text{core}} = \arcsin\left(\frac{n_{\text{clad1}}}{n_{\text{core}}}\right) \tag{2.8}$$

with $n_{\text{core}}$ and $n_{\text{clad1}}$ being the refractive indices of the fibre core and inner cladding, respectively. In the case of multiclad fibres, light rays that transit into the inner cladding because they hit the core-cladding interface at an angle too steep for TIR can still be trapped inside the fibre if they get reflected at the cladding-cladding interface. Those rays are called cladding modes and the limiting critical angle $\alpha_{\text{crit}}^{\text{clad}}$ is given by

$$\alpha_{\text{crit}}^{\text{clad}} = \arcsin\left(\frac{n_{\text{clad2}}}{n_{\text{clad1}}}\right) \tag{2.9}$$

with $n_{\text{clad2}}$ being the refractive index of the outer cladding.
Theoretically, additional light can be trapped inside a fibre via TIR on the cladding-air interface at the fibre surface. But in a use case this interface can not be assured over the whole length of a fibre. The surface of the fibre might come into contact with materials with refractive indices larger than $n_{\text{clad1}}$ or $n_{\text{clad2}}$, respectively, preventing TIR. Even without any contact, light rays entering the outer cladding are prone to sooner or later leak out of the fibre due to imperfections (like microscopic scratches) or contaminations of the cladding-air interface. Successful TIR is therefore limited by the refractive indices of the fibre claddings which lie in the order of $1.4 - 1.6$ for materials that proved suitable to be used as claddings for optical plastic fibres [19].

In general, light rays that propagate at larger polar angles get reflected more often and travel a longer effective length inside the fibre. Thus, the probability to get scattered at impurities of the fibre material and, therefore, leave the fibre is larger for those rays in comparison to light that travels at smaller angles with respect to the fibre axis.

As can be seen in equation 2.7, the incidence angle $\alpha$ of a meridional ray ($\phi = 0°$) depends only on the ray's polar angle $\theta$. The condition for TIR sets a maximal limit on the possible polar angles of propagable meridional rays. Figure 2.8 shows the construction of the maximal possible polar angles $\theta_{\text{max}}^{\text{core}}$ and $\theta_{\text{max}}^{\text{clad}}$ inside the fibre for meridional core and cladding modes, respectively. It follows

$$\theta_{\max}^{\text{core}} = 90° - \arcsin\left(\frac{n_{\text{clad1}}}{n_{\text{core}}}\right) \tag{2.10}$$

and

$$\theta_{\max}^{\text{clad}} = 90° - \arcsin\left(\frac{n_{\text{clad2}}}{n_{\text{core}}}\right) > \theta_{\max}^{\text{core}} \quad . \tag{2.11}$$

For skew rays, equation 2.7 shows that the incidence angle $\alpha$ increases with $\rho$ or $\phi$, respectively. Skew rays can therefore be propagated inside the fibre with larger polar angles than $\theta_{\max}^{\text{core}}$ and $\theta_{\max}^{\text{clad}}$ which only apply to meridional rays. The closer to the cladding the rays spiral, the larger the polar angles can be. Skew rays with large polar angles are therefore confined to the outer region of the fibre profile.

When exiting the fibre at the end, the light rays get deflected following Snell's law (eq. 2.1). If the end surface is perpendicular to the fibre axis (as is the case for the fibres examined in this thesis), the exiting polar angle $\delta$ towards the fibre axis only depends on the polar angle of the light ray inside the fibre. For a transition into air ($n_{\text{ambient}} = n_{\text{air}} \approx 1$) the exiting angle is given by

$$\delta = \arcsin\left(\frac{n_{\text{core}}}{n_{\text{air}}} \cdot \sin(\theta)\right) = \arcsin\left(n_{\text{core}} \cdot \sin(\theta)\right) \quad . \tag{2.12}$$

The maximal possible exiting angle $\delta_{\max}$ of meridional rays defines the so-called numerical aperture $\text{NA} = \sin(\delta_{\max})$ of a fibre. It is also called the acceptance angle of the fibre. The numerical aperture is commonly used to classify optical fibres or other optical components. It helps to estimate if a fibre can be used in an experimental setup with a given angular acceptance.

For singleclad fibres, the numerical aperture $\text{NA}_\text{s}$ is set by the exiting angle $\delta_{\max}^{\text{core}}$ of meridional core modes propagating at the maximal possible polar angle $\theta_{\max}^{\text{core}}$ (see fig. 2.9). It follows:

$$\begin{aligned}
\delta_{\max}^{\text{core}} &= \arcsin\left(n_{\text{core}} \cdot \sin(\theta_{\max}^{\text{core}})\right) \\
\Leftrightarrow \delta_{\max}^{\text{core}} &= \arcsin\left(n_{\text{core}} \cdot \cos(\alpha_{\text{crit}}^{\text{core}})\right) \\
\Leftrightarrow \delta_{\max}^{\text{core}} &= \arcsin\left(n_{\text{core}} \cdot \cos(\arcsin\left(\frac{n_{\text{clad1}}}{n_{\text{core}}}\right)\right) \\
\Leftrightarrow \delta_{\max}^{\text{core}} &= \arcsin\left(\sqrt{n_{\text{core}}^2 - n_{\text{clad1}}^2}\right)
\end{aligned}$$

and

$$\text{NA}_\text{s} = \sin(\delta_{\max}^{\text{core}}) = \sqrt{n_{\text{core}}^2 - n_{\text{clad1}}^2} \quad . \tag{2.13}$$

The numerical aperture $\mathrm{NA_m}$ of a multiclad fibre is limited by the maximal polar angle $\theta_{\mathrm{clad}}^{\mathrm{max}}$ of meridional cladding modes. It is

$$\delta_{\mathrm{max}}^{\mathrm{clad}} = \arcsin\left(\sqrt{n_{\mathrm{core}}^2 - n_{\mathrm{clad2}}^2}\right) > \delta_{\mathrm{max}}^{\mathrm{core}} \tag{2.14}$$

and

$$\mathrm{NA_m} = \sqrt{n_{\mathrm{core}}^2 - n_{\mathrm{clad2}}^2} > \mathrm{NA_s} \tag{2.15}$$

The additional layer therefore increases the numerical aperture of a fibre and allows for larger input (and exiting) angles of meridional rays. Those rays can leave the fibre at any point of the end surface since they do not have a closest approach to the fibre centre.

As mentioned before, skew rays can be propagated at larger polar angles and may therefore exit the fibre at angles exceeding $\delta_{\mathrm{max}}^{\mathrm{core}}$ (singleclad) or $\delta_{\mathrm{max}}^{\mathrm{clad}}$ (multiclad). The spiralling rays leave the fibre further away from the fibre centre ($\rho \neq 0$) and therefore add to the light output closer to the edges of the fibre end. Hence, an increase towards the fibre edges in the spatial light distribution at the end surface of round fibres is to be expected, if the skew rays are not suppressed by light losses due to the longer effective propagation length and increased number of reflections.

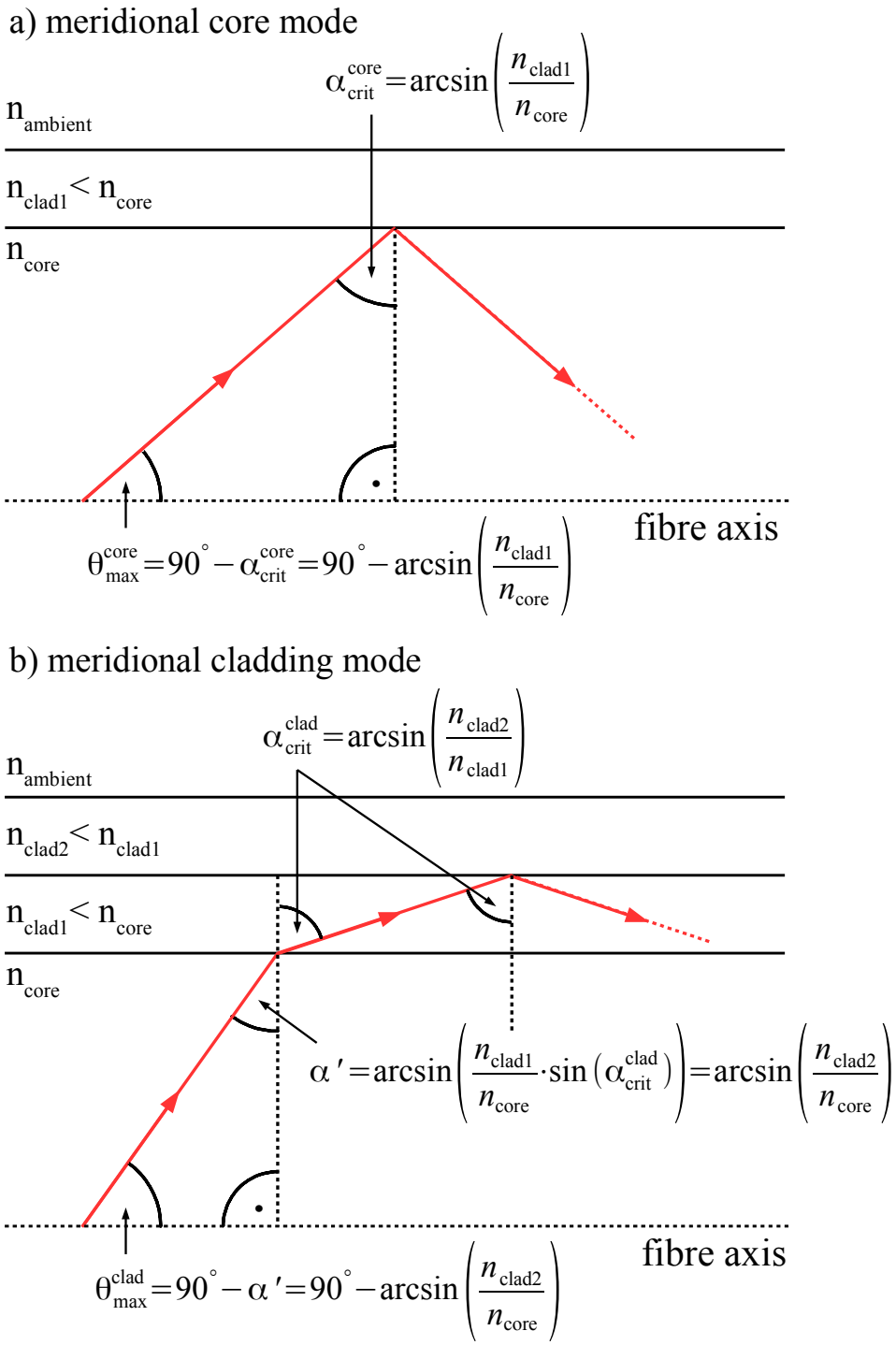


**Figure 2.8:** Top: Construction of the maximal possible polar angle $\theta_{max}^{core}$ of transportable meridional core modes set by the critical angle $\alpha_{crit}^{core}$ for TIR at the core-cladding interface of an optical fibre. Bottom: Similar construction of the maximal polar angle $\theta_{max}^{clad}$ for meridional cladding modes. Singleclad fibres are used in setups where smaller exiting angles are essential (gap between fibre and sensor, small angular acceptance of adjoining device, etc.). In the other case, multiclad fibres are preferred since they show a higher flexibility and durability than singleclad fibres with the same outermost refractive index [20].

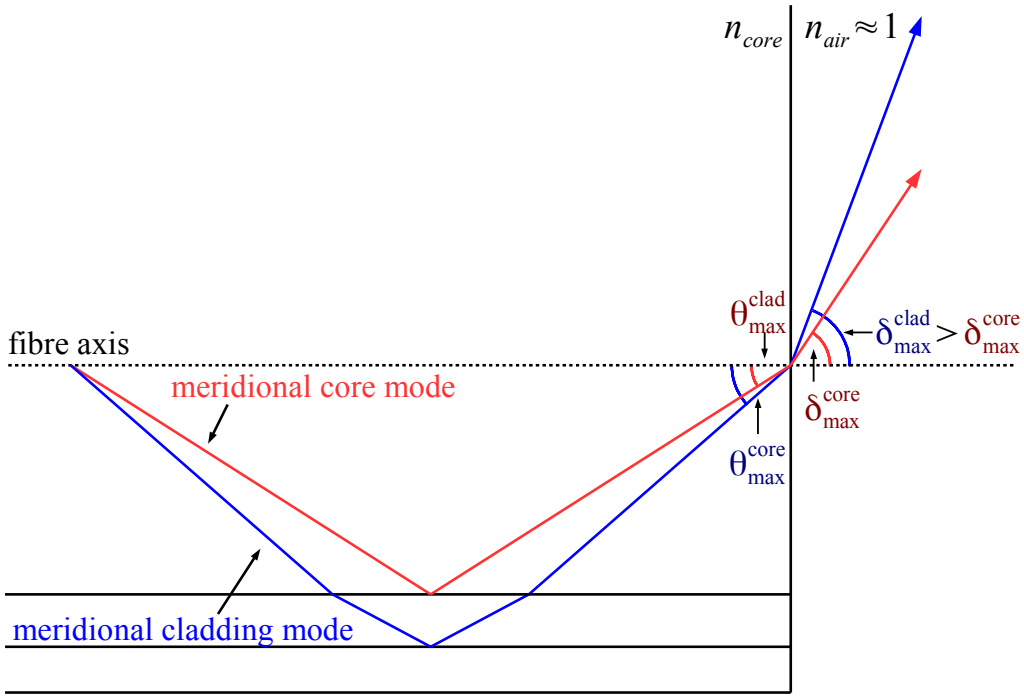


**Figure 2.9:** Schematic of the maximal possible exiting angles $\delta_{\max}^{\text{core}}$ and $\delta_{\max}^{\text{clad}}$ at the end surface of an optical fibre for meridional core modes (red) and cladding modes (blue), respectively. Since cladding modes propagate at larger polar angles inside the fibre, their exiting angles exceed those of core modes.

### 2.3.2 Square Fibres

Most of the considerations from the prior section on round fibres (core and cladding modes, numerical aperture etc.) can be adapted to fibres with a square cross section. However, there are differences in the propagation of meridional and skew rays leading to a distinct spatial light distribution at the fibre end.

Figure 2.10 depicts the perpendicular projection of meridional and skew rays inside a square optical fibre. Similar to round fibres, meridional rays have a perpendicular incident angle of $\phi = 0°$ and are therefore repeatedly reflected inside the same plane while travelling along the fibre. But here this plane lies parallel to one of the fibre edges and does not necessarily cross the fibre centre. Meridional rays may therefore have a constant minimal approach $\rho \neq 0$ to the fibre centre.

Skew rays have a perpendicular incident angle of $\phi \neq 0°$ or $\phi' = 90° - \phi \neq 0°$ depending on which of the orthogonal fibre edges the ray is reflected. The skew rays zig-zag across the entire fibre profile without a minimal approach $\rho$ to the centre. They are therefore not confined to a specific area of the fibre cross section like the skew rays spiralling inside the outer section of a round fibre.

Since both meridional and skew rays are distributed across the whole fibre profile, one expects a more homogeneous light output across the fibre's end surface than in the case of a round fibre.

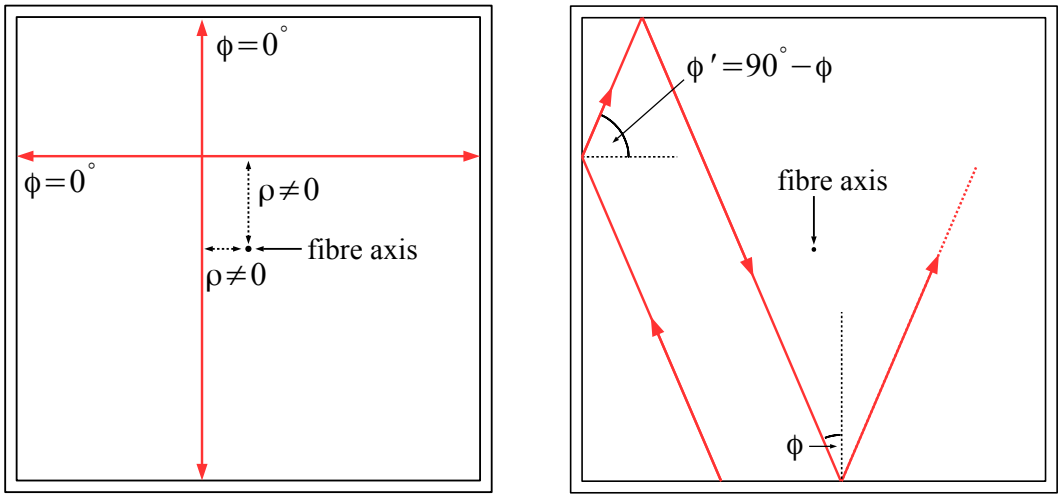


**Figure 2.10:** Perpendicular projection of meridional rays (left) and skew rays (right) inside a square optical fibre. It can be seen that meridional rays propagate inside planes with a constant closest approach $\rho$ to the fibre centre while skew rays zig-zag across the fibre profile.

# 3 Experimental Setup

In the course of this thesis, two setups for the examination of light from optical fibres were constructed. They were designed to measure the spatial and angular light distribution at the fibre end, respectively. Both setups can be divided into three main components: a light source at one fibre end, a unit to position and fixate the opposing one, and a readout system for the detection of light exiting the fibre. The first two components are the same in both cases. However, each experimental setup uses a distinct fibre readout system which is adapted to the respective measurement. The setup components are described and illustrated in the following sections.

## 3.1 Light Coupling

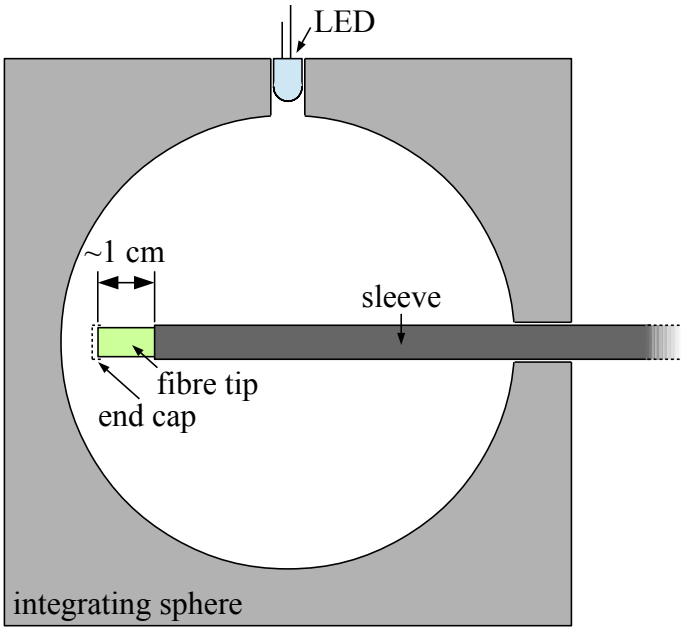


**Figure 3.1:** Schematic of the used light coupling system. The integrating sphere allows a homogeneous illumination of the exposed fibre tip. To prevent direct light coupling during the examination of WLS and scintillating fibres, an opaque plastic cap is placed on the fibre end surface.

In both setups the light source is an LED illuminating one of the fibre tips. In the case of WLS and scintillating fibres, a UV/blue LED with a peak wavelength of $\lambda_{\mathrm{UV}} = 396\,\mathrm{nm}$ resulted in a sufficient inducement of scintillation or florescence, respectively. For the examination of clear light guiding fibres a brighter green LED ($\lambda_{\mathrm{green}} = 508\,\mathrm{nm}$) was used

(for the LED spectra see appendix section A.1).
To prevent light coupling from other sources, the fibre is enclosed by an opaque plastic sleeve. Only the illuminated tip is left bare over a length of approx. 1 cm.
In the case of scintillating and WLS fibres, one is interested in the distribution of the induced scintillation and fluorescence photons (cf. section 2.2). To prevent propagation of primary light from the LED, the fibre's end surface is covered with a plastic cap. This way, primary photons may only enter the fibre through the cladding. If not absorbed by the respective dopant in the core and re-emitted with a different orientation, they merely pass through the fibre without getting trapped (see fig. 2.4).
The cap is removed in the case of clear light guides, so that the light from the LED may couple directly into the fibre's end surface.
To eliminate effects on the measured light distribution caused by inhomogeneities of the light source, an integrating sphere is used as a diffuser for the LED light. One port of the sphere holds the LED. The fibre tip is fed into the sphere through a port orthogonal to the LED preventing direct illumination of the end surface (see fig. 3.1). The LED is connected to a microcontroller board. It powers the LED and allows the adjustment of the source's brightness via pulse width modulation.

## 3.2 Fibre Positioning

For a precise examination of an optical fibre a stable fixation of said fibre and the ability to finely adjust its position and alignment is necessary. The fibre positioning unit assembled for the experimental setup (see fig. 3.4) accounts for those requirements.
The examined fibre is held inside a so-called fibre chuck. As can be seen in figure 3.2, the fibre chuck is an approx. 70 mm long, internally bored brass rod with plastic inlays. In combination with the chuck's screwable end caps, those inlays form a collet mechanism used to fixate the fibre. The chuck is attached to a fibre chuck rotator allowing a revolution of the fixed fibre around its optical axis (fig. 3.2).
The chuck rotator is mounted on a gimbal mount with two orthogonal and independently pivotable axes (fig. 3.3). The mount is used to align the fibre end parallel to the later described readout sensor. With the help of two micrometer screws the axes can be tilted up to $\pm 2.5°$.
An accurate positioning of the fibre is accomplished by attaching the gimbal mount to a combination of three linear translation stages. Each stage can be moved precisely by 26 mm with the help of a micrometer screw. The individual stages are joined orthogonally to each other, thus forming a three-axis translation stage. This allows a positioning of the fibre in three dimensions.
Figure 3.4 shows a photo of the fully assembled fibre positioning unit.

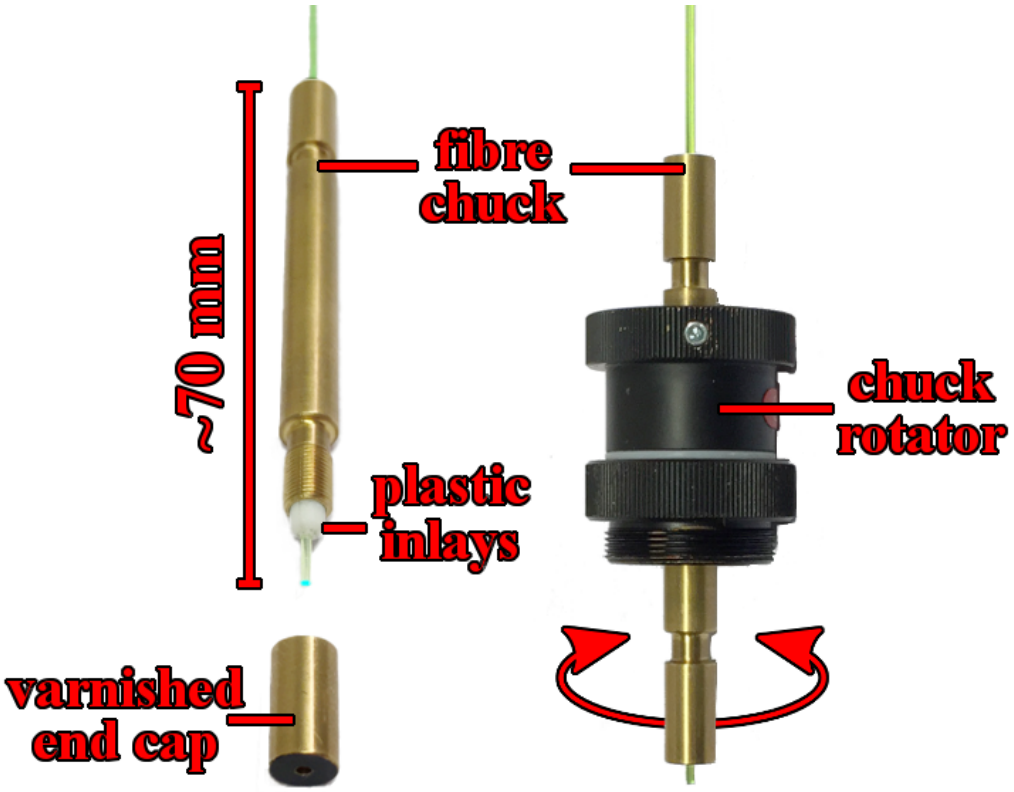


**Figure 3.2:** Left: The fibre chuck used to hold and fixate the examined fibres. Right: The fibre chuck inside the chuck rotator which allows a revolution of the fibre around its optical axis. The frontal surface of the chuck end cap that faces towards the readout system(s) (see section 3.3) is coated with matt black varnish to prevent interfering light reflexes at the metallic surface during the measurements.

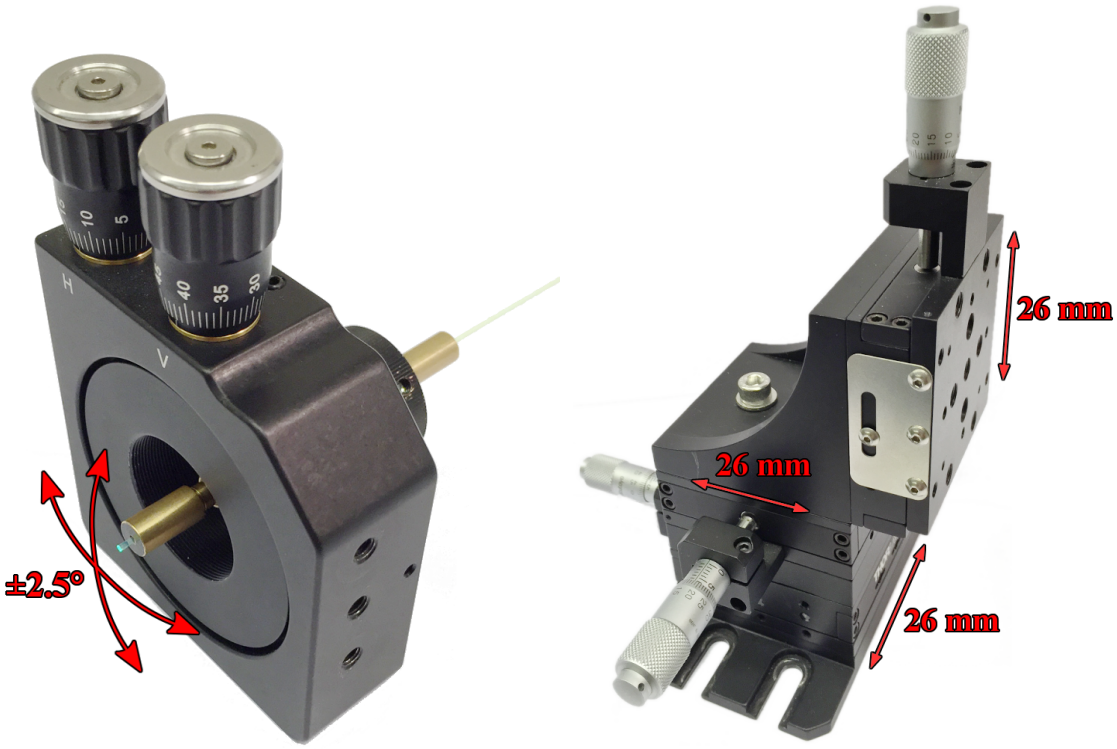


**Figure 3.3:** Gimbal mount and three-axis translation stage used to align and position the examined fibre end. The axes of the gimbal mount can be tilted up to ±2.5°. Each individual translation stage can be moved by 26 mm.

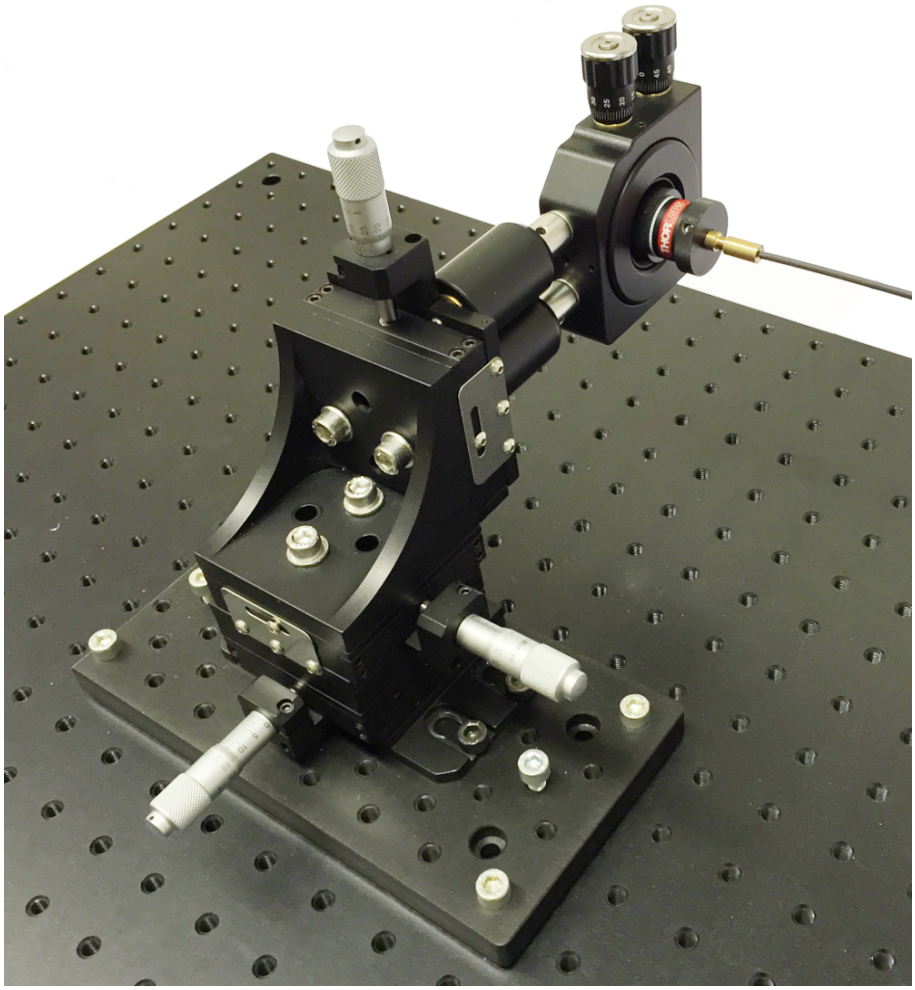

**Figure 3.4:** The fully assembled fibre positioning unit consisting of fibre chuck, chuck rotator, gimbal mount, and three-axis stage.

## 3.3 Fibre Readout

In both setups the core of the readout system consists of a digital photo camera. The fibre's light output is measured by taking pictures of the fibre end. However, the systems differ from another since they concentrate on different characteristics of the exiting light.

### 3.3.1 Readout System for the Measurement of the Spatial Light Distribution

The fibre readout for the determination of the spatial light distribution at the fibre end surface is done with a monochrome camera (ALccd IMG0S-M [21]) usually used for astronomical measurements. It features a CCD sensor (Sony ICX204AL-E [22]) with a resolution of 1024x768 pixels and a square pixel pitch of 4.65 $\mu$m. The readout system has a bit depths of 15 bits meaning that $2^{15} = 32768$ different levels of irradiance can be distinguished.
The camera is connected to a computer via USB and images are taken with the help of the EZPlanetary capturing software [23].

To get the correct picture of a fibre's spatial light distribution, one has to get the camera sensor as close to the fibre end as possible. The resolution of the spatial measurement is then set by the pixel pitch of the used sensor. Since light exits the fibre at different angles, a large gap between sensor and fibre would result in a severe dispersion of the spatial light profile. To achieve a close approach, parts of the camera's cover panel as well as the protective glass on the CCD sensor were removed (see fig. 3.5).
The distance between CCD sensor and fibre end is measured with the help of a specially designed LED board attached to the camera. As can be seen in figure 3.5, this board features four pairs of red[1] LEDs arranged in a cross-like pattern around the camera sensor. Each LED pair is used to cast fibre shadows from different altitudes onto the CCD. As the schematic in figure 3.6 shows, the displacement $\Delta$ of those shadows decreases towards smaller distances $d$ between fibre end and CCD sensor. The calculations presented in appendix section A.3 show that for close approaches, the shadow displacement depends linearly on the fibre distance. It follows:

$$\Delta(d) \approx x_\mathrm{f} \cdot \left( \frac{1}{D_1} - \frac{1}{D_2} \right) \cdot d \Rightarrow \Delta(d) \propto d \tag{3.1}$$

with $D_1$, $D_2$ being the vertical distance of the two LEDs from the CCD plane and $x_\mathrm{f}$ being the position of the illuminated fibre edge.
For unknown parameters $D_1$, $D_2$ and $x_\mathrm{f}$, the fibre distance cannot be calculated from a single measurement of the shadow displacement. However, the closest approach between sensor and fibre end can be determined by moving the camera step by step closer to the fibre and obtaining $\Delta$ for each step. The translation has to be started at a safe distance

[1] Red LEDs were chosen since they did not induce notable scintillation or fluorescence inside the WLS and scintillating fibre which would interfere with the identification of the shadow edges later on.

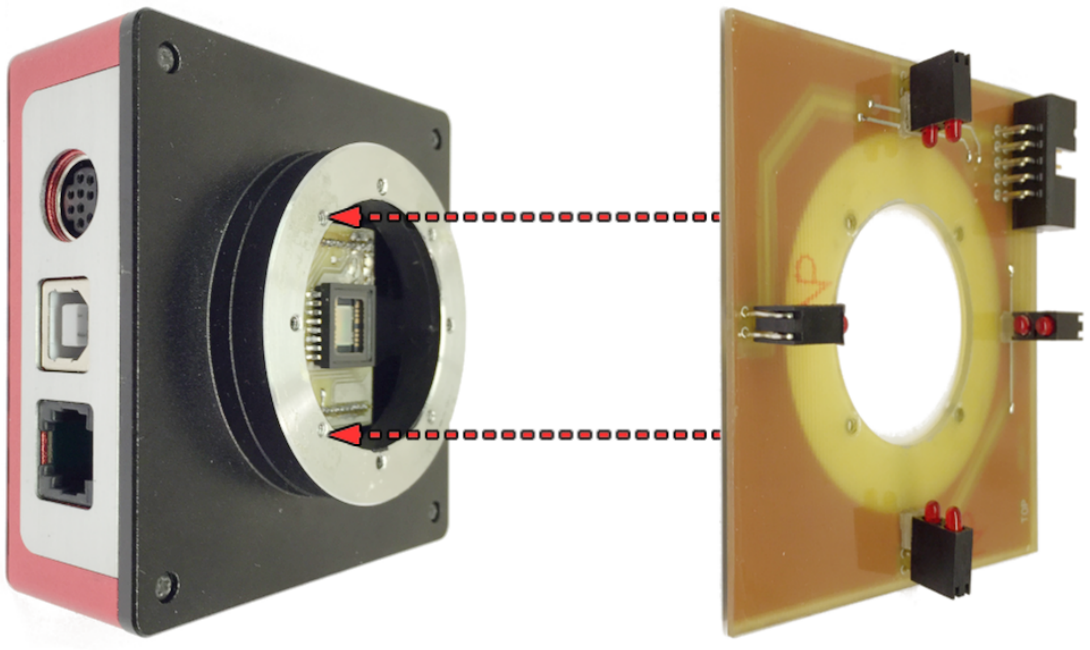

**Figure 3.5:** Left: The modified CCD camera used in the measurements of the spatial light distribution. To get the fibre end as close to the sensor as possible, parts of the cover panel as well as the sensor's cover glass are removed. Right: The LED board which is attached to the camera and used to determine the distance between sensor and examined fibre end.

between fibre and CCD in the order of 1 mm. This starting position is used as the point of reference for the sensor position $s$ during the following approach. Given the linear progression of the shadow displacement, the sensor position corresponding to $\Delta = 0$ (meaning contact between fibre and CCD) can be extrapolated from a linear fit. Then, the difference between extrapolated and current camera position reveals the absolute distance between the CCD and the illuminated fibre edge. More details on the implementation and limitations of the distance determination can be found in section 4.3.1.

The LED board features four pairs of LEDs to determine the distance towards four different points of the fibre end (see fig. 3.7). This is necessary to obtain the tilting of the fibre end relative to the CCD. A parallel adjustment is crucial for a minimal camera approach, because otherwise the unprotected sensitive area of the sensor might get damaged or destroyed by contact with the closest part of the tilted fibre end. Therefore, the arrangement of the four LED pairs corresponds to the axes of the previously described gimbal mount which allows the correction of a measured tilting.

For a precise and controllable translation of the camera relative to the fibre[2], the camera is

[2]Since the camera is smaller and weighs less than the fibre positioning system, the camera is moved

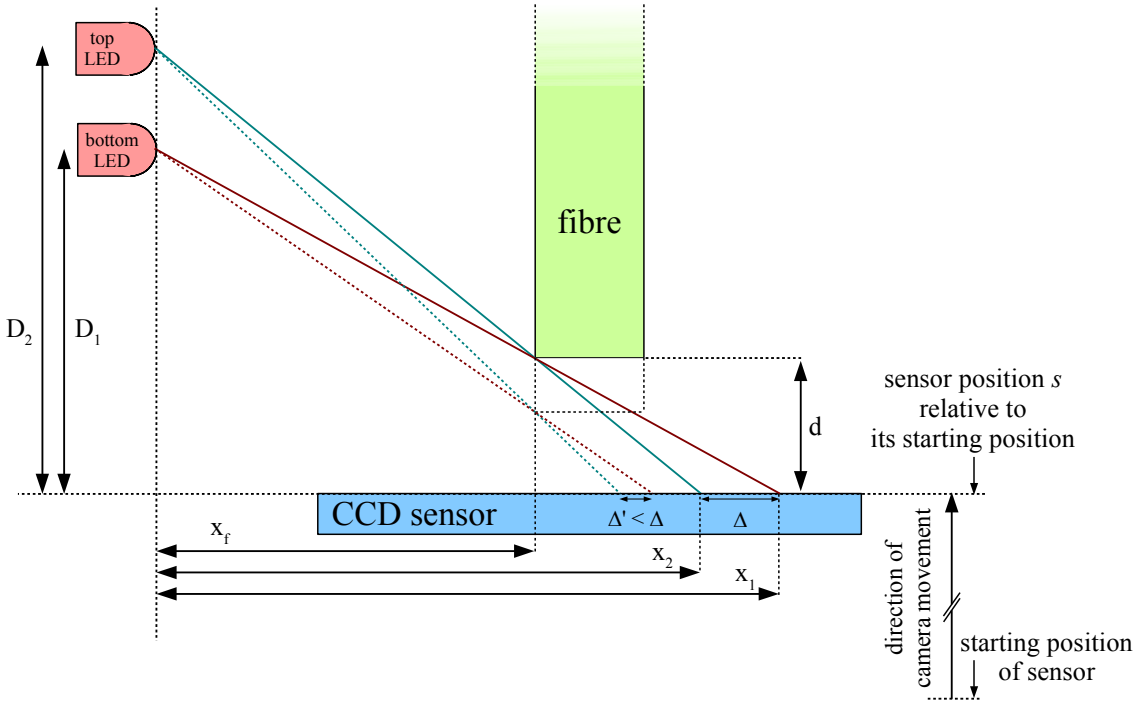


**Figure 3.6:** Schematic principle of the fibre distance determination via LEDs which cast shadows of the fibre onto the CCD sensor from different vertical distances. The shadow displacement $\Delta$ decreases with a closer approach of the fibre end towards the CCD sensor plane. Here $\Delta$ and $\Delta'$ are the shadow displacements for a greater and a smaller distance between fibre end and sensor, respectively. For a better visualisation the schematic shows how the shadow displacement changes if the fibre is moved towards the sensor plane. In the actual measurements it was easier to move camera and LEDs towards the fibre end with a piezo-driven translation stage. The image shows the direction of the camera movement. The sensor position $s$ is measured relative to its position at the start of the approach towards the fibre.

mounted on top of a piezo-driven translation stage (Newport CONEX-AG-LS25-27P [24]) with a minimal step size of 100 nm (see fig. 3.8). The stage position can be adjusted and determined with the help of a connected computer.
The assembled readout system is placed in front of the fibre positioning unit. The complete experimental setup for the spatial light distribution measurements as well as a closer view of the fibre end in front of the CCD sensor can be seen in figures 3.9 and 3.10.

towards the fibre instead of the other way around to achieve an accurate movement.

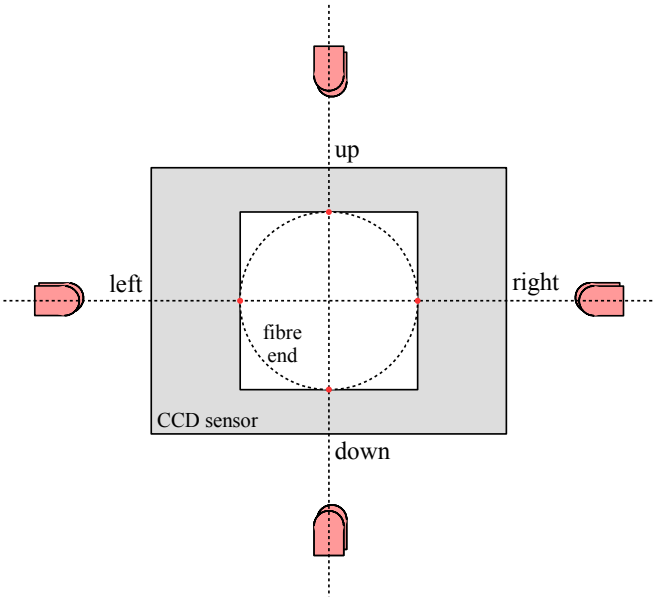


**Figure 3.7:** Schematic of the LED pair arrangement around the CCD sensor. The red dots indicate the points of the fibre edge for which the distance to the sensor is determined to obtain a possible tilting of the fibre end.

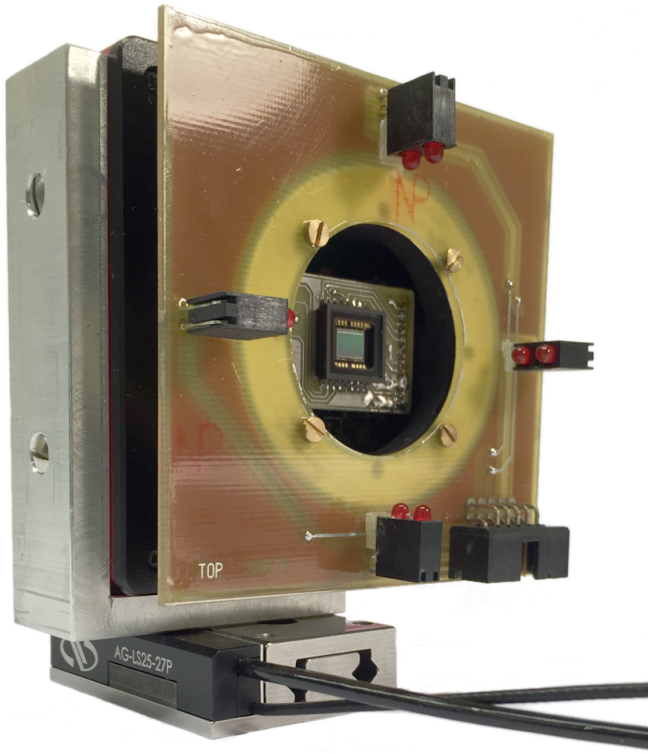


**Figure 3.8:** The CCD camera with attached LED board mounted on top of the piezo-driven translation stage.

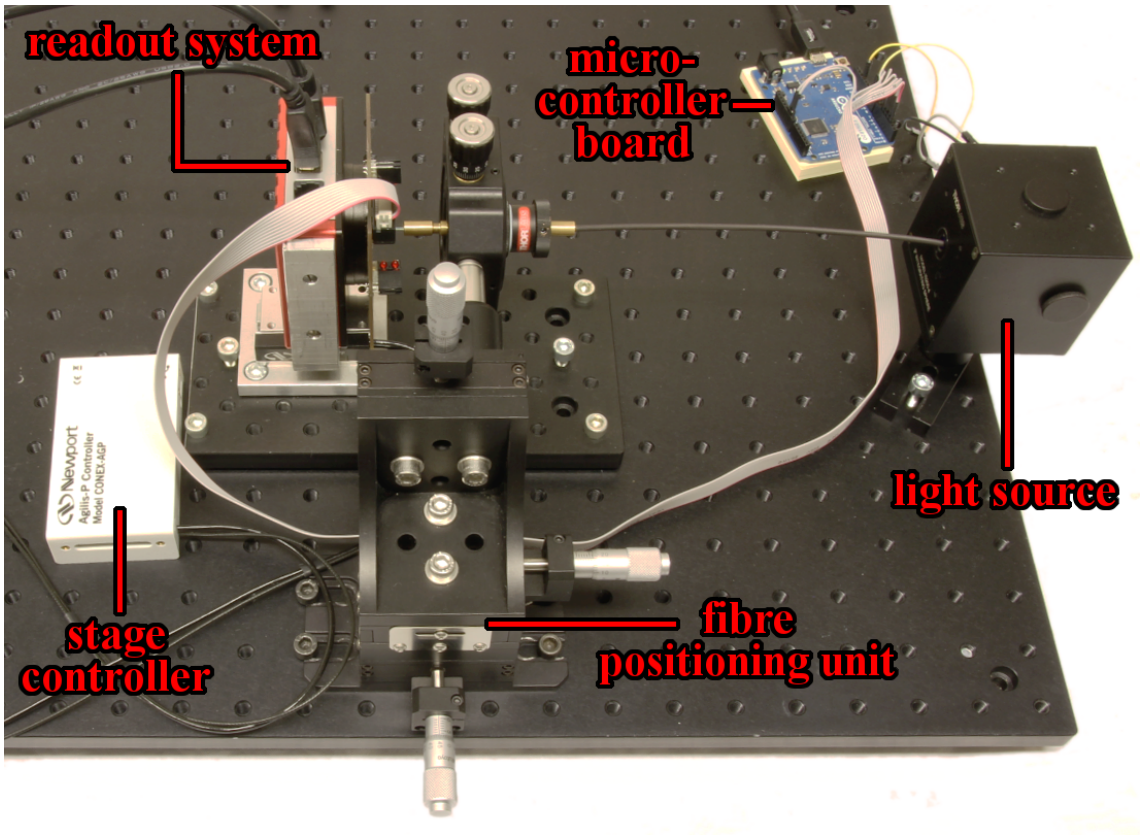


**Figure 3.9:** Photo of the experimental setup used to determine the spatial light distribution at the fibre end surface. The examined fibre is slightly bent due to its storage on a fibre spool.

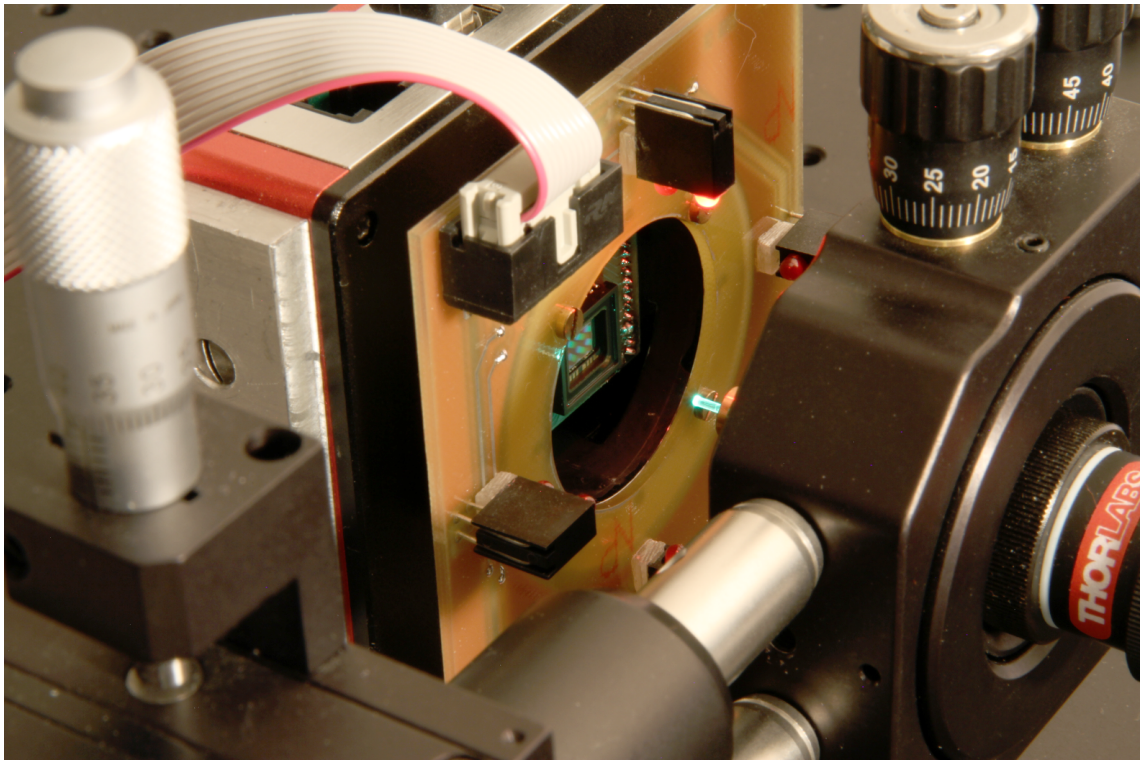


**Figure 3.10:** Close view of the readout system used for the measurement of the spatial light distribution at the fibre end surface. For a better view, the CCD camera is retracted.

### 3.3.2 Readout System for the Measurement of the Angular Light Distribution

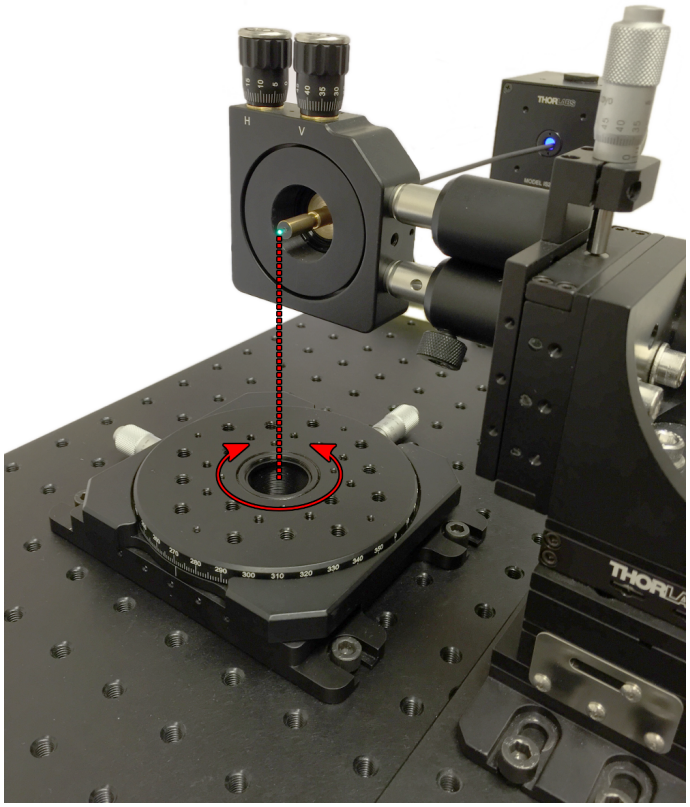

**Figure 3.11:** The fibre positioning unit placed next to a rotation stage so that the fibre end lies within the rotation axis. Thus, a camera system attached to the rotation stage can examine the fibre at different angles.

For the measurements of the angular distribution of light exiting an optical fibre a readout system able to examine the fibre end at different angles with respect to the surface normal is required. For this purposes, the fibre positioning unit is placed next to a rotation stage in a way that the fibre end lies within the rotation axis (see fig. 3.11).
Mounted onto the rotation stage is the camera system shown in figure 3.12. A monochrome CMOS camera (manufacturer: QHYCCD, model: QHY5L-II [25]) is used to take the pictures of the fibre end. If features a CMOS sensor (Aptina MT9M034 [26]) with a 1280x960 resolution and a square pixel pitch of 3.75 $\mu$m[3]. The bit depth of the readout system amounts to 11 bits.
For sharp and full frame images of the fibre end a macro-objective system is attached to the camera. The magnification of the lens tube can be changed continuously between 1×

[3]While the CMOS sensor features a smaller pixel pitch than the CCD sensor, it was not possible to use the camera in the measurements of the spatial light distribution, since the sensor could not be purchased without the cover glass. The CCD camera was not used for both setups since the camera system for the angular measurements was already fully assembled when the construction of the setup for the examination of the spatial light output distribution began.

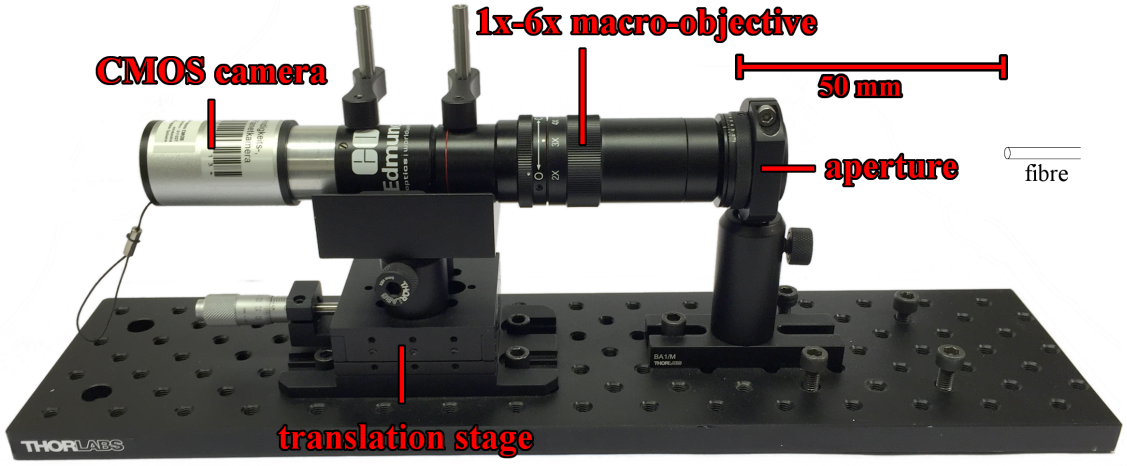


**Figure 3.12:** The camera system used in the measurements of the angular light distribution of optical fibres. The linear translation stage allows the fine adjustment of the distance between camera system and examined fibre end. The distance between the system's aperture and the examined fibre ends amounts to 50 mm.

and 6×. This, in combination with the small pixel pitch of the sensor, allows for an exact and detailed examination of the fibre end surface.
To lower the angular acceptance of the camera system, an adjustable aperture is placed in front of the lens tube. Thus, only light that travels almost parallel to the optical axis will be detected. The light's maximal deviation from this line sets the resolution of the angular light distribution measurements. As discussed further in section 4.4.1 the assembled setup achieves an angular acceptance of 2°.

The complete camera system is attached to the rotation stage so that the stage's rotation axis lies inside the focal plane 50 mm away from the aperture. This arrangement allows an examination of the fibre end at angles between 0° and 90°[4]. Figure 3.13 shows the experimental setup for the angular distribution measurements in full.

[4]Due to the placement of the fibre positioning unit (see fig. 3.13), the camera system could only be fully pivoted into one direction. Therefore the fibre end could not be observed at angles between −90° and +90°.

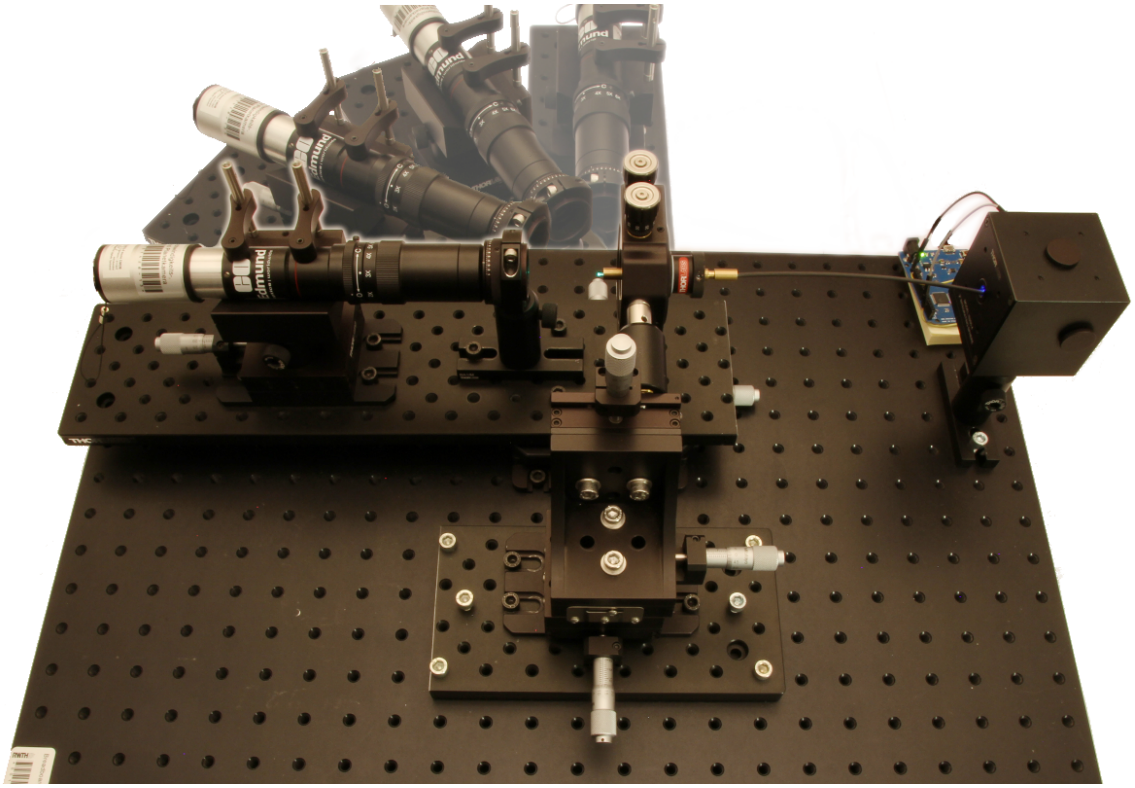

**Figure 3.13:** The fully assembled experimental setup used to determine the angular light distribution at the end surface of optical fibres. The camera can be rotated to examine the fibre end surface at angles up to 90°.

# 4 Measurements and Results

In the first section of this chapter, the examined fibres as well as their preparation for the measurements are presented. This section is followed by an explanation of how the images taken during the measurements were corrected for several possible sources of error. The concluding sections 4.3 and 4.4 cover the data acquisition and analysis for the two main measurements of this thesis.

## 4.1 Fibre Preparation

In the course of this thesis, three plastic multimode fibres with different geometrical properties (shape and number of claddings) were examined. The first fibre was a singleclad light guide with a round cross section (EdmundOptics EO-534S [27]). It consists of a clear PMMA core surrounded by an FP cladding. The second fibre was a round multiclad blue-to-green WLS fibre with two claddings around a PS core (Kuraray Y-11M [14]). The inner cladding is made of PMMA, the outer one of FP. It has a round cross section as well. Finally, the third examined fibre was a scintillating multiclad fibre with a square cross section (Saint Gobain BF-10MC [13]). The core and cladding materials are the same as for the WLS fibre. The emission spectra of the WLS and the scintillating fibre are shown in section A.2 of the appendix.
All fibres have a diameter of 1 mm. A comparative overview of the fibre properties is shown in table 4.1. For a better study of the differences between single- and multiclad fibres, it would have been preferable to examine further fibres like a square singleclad fibre or a pair of a single- and a multiclad fibre of the same type. Unfortunately, WLS and scintillating fibres (other than the examined multiclad fibres which were already in stock at our institute) could not be purchased during the work on this thesis. Clear light guides could be obtained, but only as singleclad fibres.

A major challenge encountered while preparing the fibres for the following measurements, was achieving a clean and undamaged fibre end surface. Several approaches for cutting the fibres with as little damage as possible to fibre core and cladding(s) were tested or considered. They ranged from cutting the fibre with a heated blade or a focussed laser beam to freezing the fibre in liquid nitrogen and then breaking or cutting it. Most of the approaches resulted in damaged fibre ends unsuitable for the desired quality of the end surfaces or were declared impractical by experts in the field of laser technology and plastic processing [28, 29].

| name | EO-534S | Y-11M | BCF-10MC |
|---|---|---|---|
| type | clear light guide | WLS | scintillating |
| shape | round | round | square |
| radius $r$ / mm | 0.5 | 0.5 | 0.5 |
| material core | PMMA | PS | PS |
| $n_{\text{core}}$ | 1.492 | 1.59 | 1.60 |
| material inner cladding | FP | PMMA | PMMA |
| $n_{\text{clad1}}$ | 1.402 | 1.49 | 1.49 |
| thickness $d_{\text{clad1}}$ / % of $r$ | 2 | 8 | 6 |
| material outer cladding | – | FP | FP |
| $n_{\text{clad2}}$ | – | 1.42 | 1.42 |
| thickness $d_{\text{clad2}}$ / % of $r$ | – | 4 | 6 |

**Table 4.1:** Properties of the optical fibres examined during this thesis [13, 14, 27]. For the square fibre the radius relates to half the edge length.

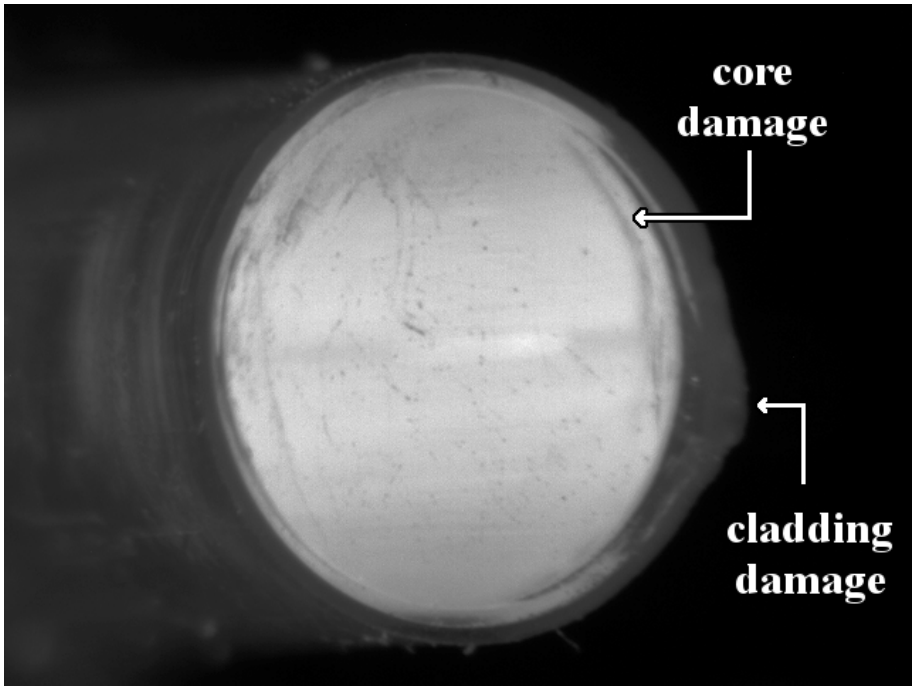


**Figure 4.1:** Photo of the milled and polished end surface of a multiclad WLS fibre. Taken with the camera system used for the determination of the angular fibre light distribution (see section 3.3.2). The camera system was slightly rotated to better show the inflicted damage on the cladding and the fibre core. Further impurities can be seen across the surface.

The chosen procedure was fixating the fibre inside an acrylic glass block with bores matching the fibre profile and milling the end with a sharp metal cutting head. The end surfaces were then polished manually using a polishing paste. As can be seen in figure 4.1, this procedure, too, led to core and cladding damage. Furthermore, the cutting and polishing

left some remains of fibre material or polishing paste on the end surface which could not be removed without afflicting additional damage. Nonetheless, this approach led to the best results in comparison to the others.

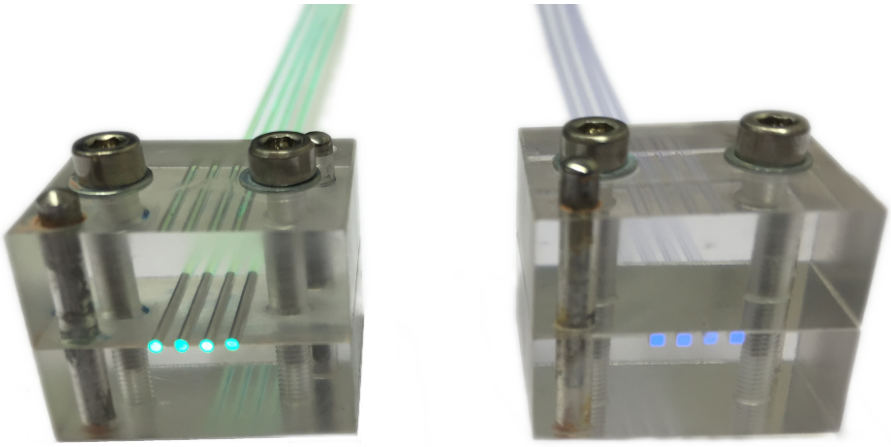

**Figure 4.2:** Photo of the acrylic glass blocks used to secure the fibres during the preparation procedure.

For each fibre type, four strands of approx. 25 cm length were prepared at the same time (see fig. 4.2). Using the pivotable camera system for the angular distribution measurements, the quality of the processed fibre ends was examined. The fibre showing the least amount of damaging and impurities of the four was then chosen for the following measurements.

## 4.2 Image Capturing Conditions and Correction

All following measurements were conducted in a darkened room. Thus, light from other sources than the examined fibre was prevented from interfering with the examination.
Since both experimental setups make use of digital camera sensors to measure the light output from the examined fibre ends, the taken images had to be corrected for sources of error originating from the electrical properties of the used sensors.

In a first step, a linear response of each sensor's signal to the amount of incident light had to be assured. An uncorrected non-linearity would have resulted in the false determination of different irradiance levels relative to one another.
The sensor response was determined for both cameras by taking a series of pictures with constant lighting conditions and varying times of exposure. At each exposure time, five frames were taken. The response of the sensor signal to the varying amount of detected light was obtained for several pixels at varying positions on the sensors. For each examined pixel, the mean signal value as well as the standard deviation was calculated from the five

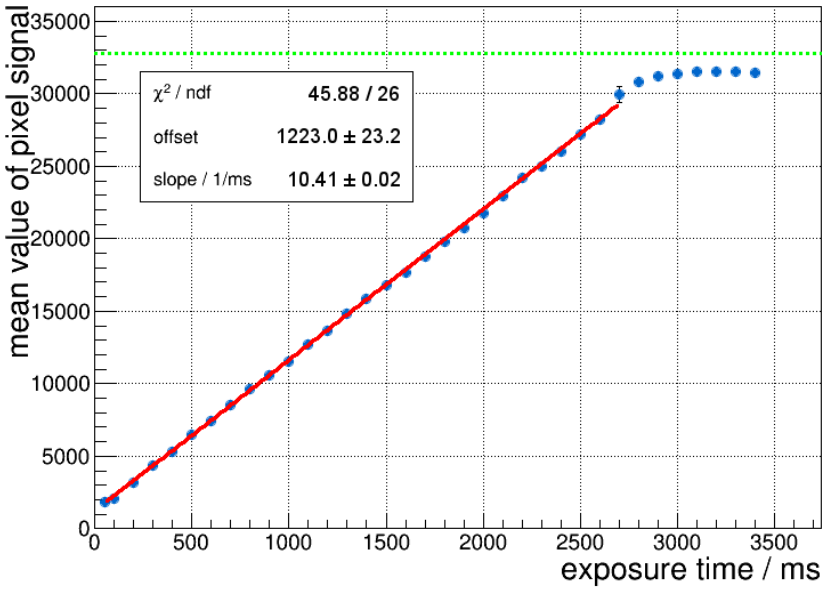


**Figure 4.3:** Response of the pixel signal to an increasing exposure time at constant lightning conditions for the central pixel $(512, 384)$ of the CCD sensor (averaged over five individual frames at each exposure time). The red line shows the conducted linear fit (results in the box). The dotted green line indicates the maximal possible value of the pixel signal. The maximal value is calculated using the bit depth of the camera. However, in this case the actual maximal possible value seems to be slightly lower than the ideal one.

individual frames. The mean pixel signal was plotted against the respective time of exposure and a linear fit was conducted. As an example, figures 4.3 and 4.4 show the results for one pixel of each sensor. Further results are shown in section A.4 of the appendix.
It can be seen that the responses follow a linear progression over the largest part of the dynamic range and that larger deviations occur only for pixel signals close to the maximal possible values of $2^{15} = 32768$ (CCD) or $2^{11} = 2048$ (CMOS), respectively. Furthermore, the slopes of the fitted linear functions are of the same order for the individual pixels of each sensor (maximal deviation between slopes of about 2%). In the measurements, the exposure time of the respective camera (as well as the intensity of the light source) was chosen in a way that only the linear part of the sensor's dynamic range was used. Therefore, a further correction of the response was not necessary.

Another possible source of error is the intrinsic random fluctuation of a pixel's signal around the actual value. To account for this, a series of three frames was taken for each measurement of the fibres' light output. Those frames were combined into one image by calculating the average value of each pixel's signal. As an uncertainty estimation on the measured amount of light, the standard deviation was calculated for each pixel as well.

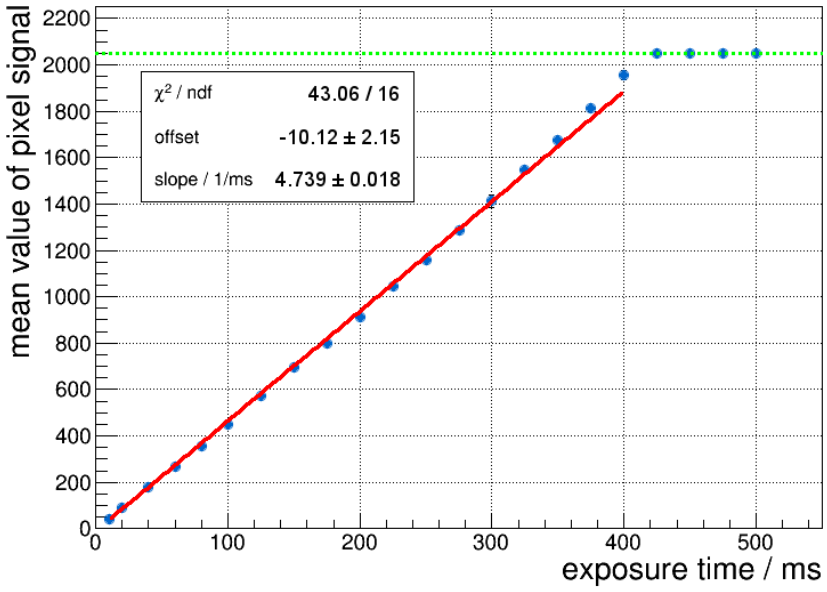


**Figure 4.4:** Response of the pixel signal to an increasing exposure time at constant lightning conditions for the central pixel (640, 480) of the CMOS sensor (averaged over five individual frames at each exposure time). The red line shows the conducted linear fit (results in the box). The dotted green line indicates the maximal possible value of the pixel signal.

In addition to that, three more frames with the fibre light source switched off were taken. Those so-called dark frames were averaged and subtracted from the image to correct the measurement for the sensors' dark noise. The standard deviation of the dark noise for each pixel was determined from the three dark-frames as well. Following Gaussian error propagation, the standard deviations from both signal and dark noise were used to obtain the total uncertainty on each pixel's value. A closer examination showed that for both cameras the uncertainty amounts to approximately 1% of the pixel value.

From here on and if not specified otherwise, a mentioned image always relates to a processed series of six frames.

## 4.3 Measurement of the Spatial Light Distribution

### 4.3.1 Experimental Procedure

In a first step, the examined fibre end was brought as close to the CCD sensor as safely possible using the fibre positioning unit. Any further approach was accomplished by moving the camera with the help of the piezo-driven translation stage in steps of 10 $\mu$m or less. As shown in fig. 3.6, the direction of the camera movement is perpendicular to the sensor

plane and towards the fibre end surface. The starting position of the sensor is used as the reference point $s = 0\,\text{nm}$ for the following determinations of the sensor's position $s$ along the axis of the camera movement.

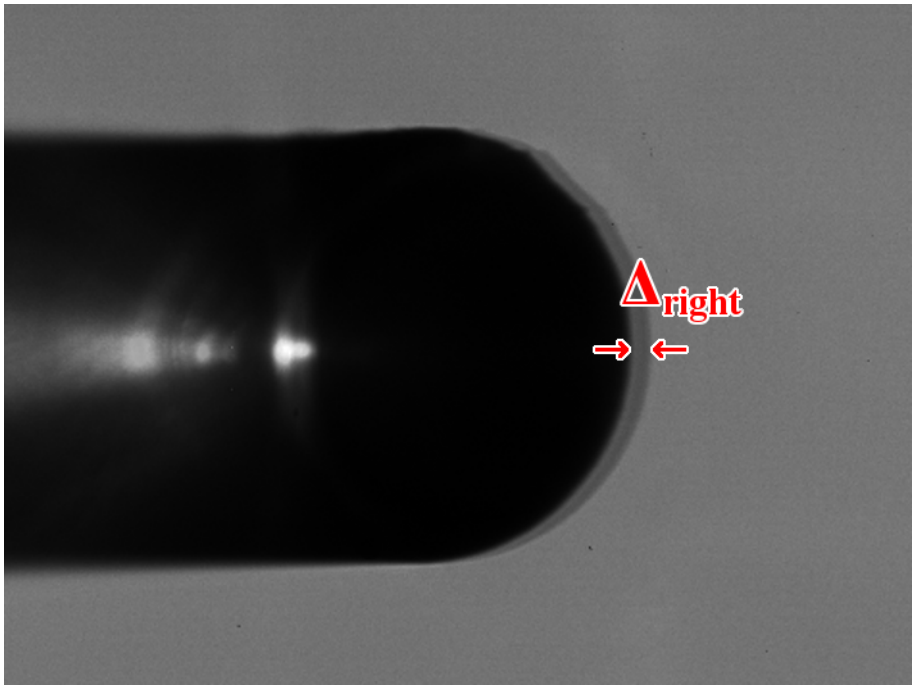


**Figure 4.5:** Superposition of two shadow frames that shows the displacement $\Delta_{\text{right}}$ for fibre shadows cast onto the CCD sensor from the LED pair right to the sensor. The arrows indicate between which points of the shadow edges the displacement was determined.

For each step towards the fibre end, the sensor position $s$ was determined with an uncertainty of $\sigma_s = 100\,\text{nm}$ from the stage driver software. At each position, an image of the approaching fibre end with light coupled from the source was taken. Furthermore, eight so-called shadow frames were obtained. For those images the light source was switched off and each of the eight LEDs attached to the camera was powered at a time, casting a fibre shadow on the CCD from a different direction and altitude. The shadow displacement $\Delta_i$ ($i$ = up, down, left and right; see fig. 3.6) was extracted from the shadow frames for each of the four LED pairs (see fig. 4.5) with an estimated accuracy of $\sigma_{\Delta_i} = \sqrt{2}\,\text{pixels} = 6.6\,\mu\text{m}$. After at least 15 steps, the determined values for $\Delta_i$ and $s$ were plotted against one another for each LED pair and a linear function $\Delta_i = m_i \cdot s + b_i$ was fitted to each data set (see fig. 4.6). The obtained parameters $m_i$ and $b_i$ were then used to calculate the stage positions $s_{0,i}$ at which the respective edge of the fibre end surface would get into contact with the CCD (resulting in $\Delta_i = 0$):

$$\Delta_i = 0 = m_i \cdot s_{0,i} + b_i \quad \Leftrightarrow \quad s_{0,i} = -\frac{b_i}{m_i} \quad . \tag{4.1}$$

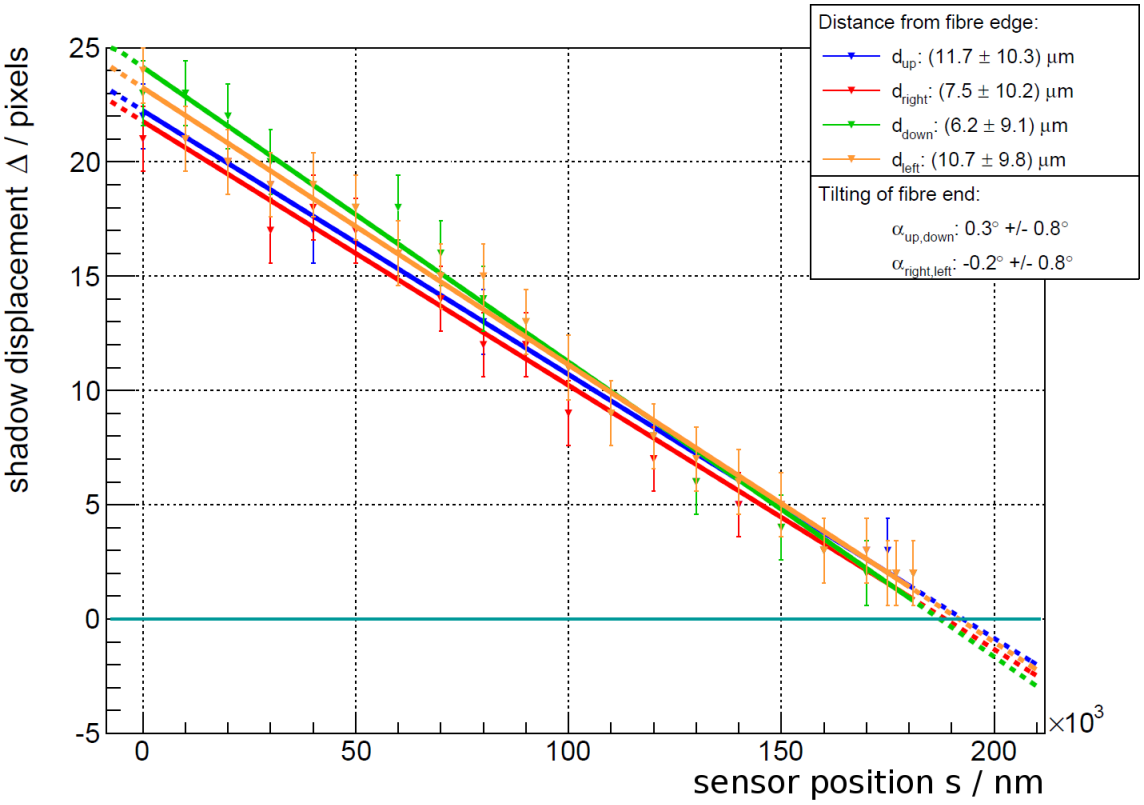


**Figure 4.6:** The shadow displacement $\Delta$ for all four LED pairs as a function of the sensor position $s$ obtained during the approach of the camera towards the round multiclad fibre. The camera is moved towards the fibre along the axis perpendicular to both the sensor plane and the fibre end surface (see fig. 3.6). The sensor's position $s$ on this axis is measured relative to its position at the start of the approach. Therefore, larger values of $s$ mean a smaller distance towards the fibre end. The distances between four points on the fibre end surface and the CCD sensor as well as the surface tilting angles are calculated from the results of a linear fit to each of the data sets.

The uncertainty on $s_{0,i}$ was calculated from the errors of the fitting parameters following

$$\sigma_{s_{0,i}} = \sqrt{\left(\frac{\sigma_{b_i}}{m_i}\right)^2 + \left(\frac{b_i}{m_i^2} \cdot \sigma_{m_i}\right)^2} \quad . \tag{4.2}$$

Then, the difference between $s_{0,i}$ and the furthest sensor position gave the current distances between CCD sensor and the four observed points on the fibre end.

To minimize the distance, the camera was translated further towards $s_{0,i}$ in steps of 10 $\mu$m (or less if necessary) while taking more images and shadow frames at each sensor position. The obtained shadow displacements were added to the linear fits for an increasingly accurate determination of the fitting parameters.

In order not to damage the sensor, the camera was only driven to the position $s_{\max}$ at which the distances $d_i = s_{0,i} - s_{\max}$ were in the order of the uncertainty $\sigma_{s_{0,i}}$ on the

extrapolated camera position. In all cases, $\sigma_{s_{0,i}}$ and, therefore, the achievable minimal distances between CCD sensor and the examined fibre amounted to approximately 10 $\mu$m.

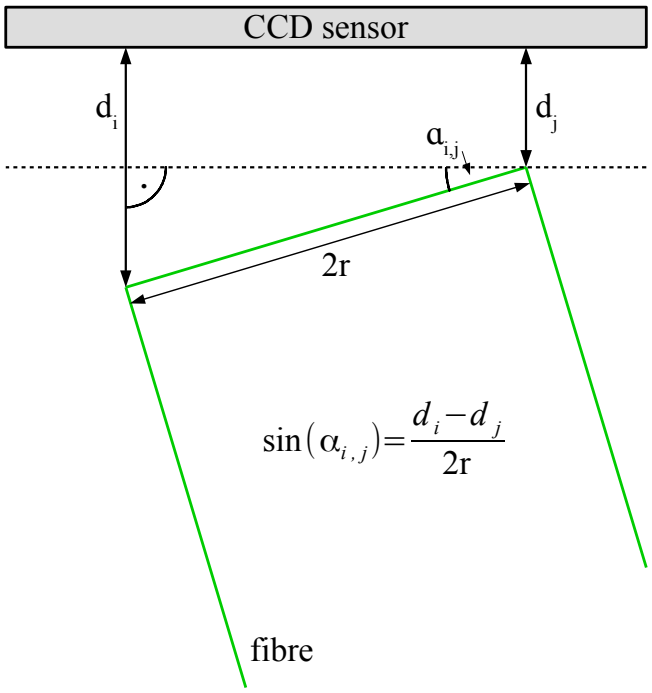


**Figure 4.7:** Schematic of how the distances $d_i$ and $d_j$ of opposing points on the fibre end surface towards the CCD sensor were used to calculate the tilting angle $\alpha_{i,j}$ of the fibre end surface with respect to the sensor plane. During the measurements two tilting angles orthogonal to one another were determined.

Figure 4.7 shows how the distances $d_i$ and $d_j$ between CCD and opposing points on the fibre end surface were then used to calculate the tilting of the fibre end. The horizontal and vertical tilting angles $\alpha_{i,j}$ ($i$,$j$ = right, left or up, down) and their uncertainty are given by

$$\alpha_{i,j} = \arcsin\left(\frac{d_i - d_j}{2 \cdot r}\right) \tag{4.3}$$

and

$$\sigma_{\alpha_{i,j}} = \sqrt{\frac{\sigma_{d_i}^2 + \sigma_{d_j}^2}{4 \cdot r^2 - (d_i - d_j)^2}} \tag{4.4}$$

where $r$ is the radius of the examined fibre.

Before correcting the tilting with the help of the gimbal mount, the camera was retracted from the fibre to protect the sensor from contact with the pivoting fibre end. After that, the procedure of approaching the fibre end was repeated from the start. The achieved

distances can be found in table 4.2).

| fibre type | round singleclad | round multiclad | square multiclad |
|---|---|---|---|
| $d_{\text{up}}$ / $\mu$m | $10.6 \pm 11.2$ | $11.7 \pm 10.3$ | $15.7 \pm 9.9$ |
| $d_{\text{down}}$ / $\mu$m | $7.2 \pm 11.7$ | $6.2 \pm 9.1$ | $13.4 \pm 8.6$ |
| $\alpha_{\text{up,down}}$ / $^\circ$ | $0.2 \pm 0.9$ | $0.3 \pm 0.8$ | $0.1 \pm 0.8$ |
| $d_{\text{right}}$ / $\mu$m | $7.4 \pm 11.7$ | $7.5 \pm 10.2$ | $12.7 \pm 9.3$ |
| $d_{\text{left}}$ / $\mu$m | $10.8 \pm 10.9$ | $10.7 \pm 9.8$ | $7.4 \pm 9.1$ |
| $\alpha_{\text{right,left}}$ / $^\circ$ | $-0.2 \pm 0.9$ | $-0.2 \pm 0.8$ | $0.3 \pm 0.7$ |

**Table 4.2:** Achieved distances $d_i$ between four points on the fibre end surface and the CCD sensor as well as the resulting tilting angles $\alpha_{i,j}$ with respect to the CCD sensor for the three examined fibres. The tilting angles were calculated using eq. 4.3 and 4.4 and a fibre radius of $r = 0.5\,\text{mm}$.

Once camera and fibre were successfully positioned and aligned, the light source was switched on and the spatial light distribution was obtained by taking an image (series) of the fibre end.

### 4.3.2 Results

Figures 4.8 through 4.10 show the obtained images (corrected for signal fluctuations and dark noise) along with a 3D visualisation of the spatial light distributions measured approximately $10\,\mu$m away from the fibre end. As a measure for the fibre light output per area of $4.65\,\mu\text{m} \times 4.65\,\mu\text{m}$ (pixel size), the (corrected) irradiance levels measured by the camera pixels were used. The distributions were normalised to the light output integrated over all pixels in the respective image. The coordinate axes were converted from pixels into micrometers using the pixel size. They were shifted as well, so that their origin lies on top of the fibre centre.

All images show signs of core and cladding damage as well as impurities[1] on the fibre end surface. Those diminish the quality of the obtained light distributions to some extent. But for each fibre, the damage is limited to only some small regions of the fibre end, and the remnants of the polishing procedure do not appear to interfere much with the overall light distribution. Therefore, conclusions about the distribution's (in)homogeneity and the principal differences between the examined fibres can still be drawn.

As expected, both round fibres show a radial symmetrical light distribution which increases towards the edge of the fibre core. This rise in the light output appears to be larger for the singleclad fibre (fig. 4.8) compared to the multiclad fibre (fig. 4.9). The distribution at the end of the square multiclad fibre seems to be rather homogeneous across the whole

[1] Those impurities could not be blown or (carefully) swiped off. They were therefore left on the end surface in order not to inflict additional damage to core and claddings during the cleaning.

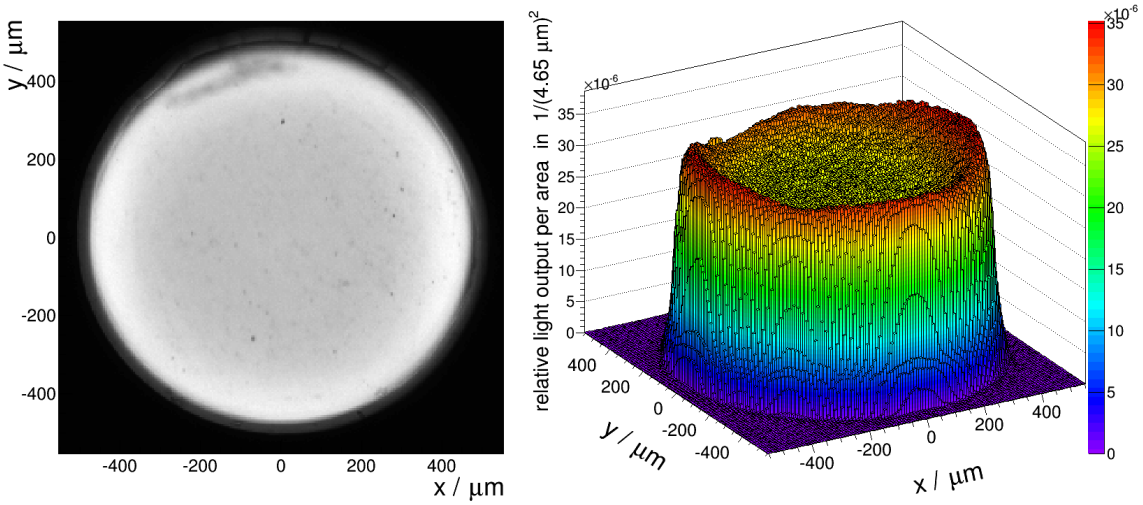


**Figure 4.8:** Left: Image of the end surface of the round singleclad light-guiding fibre at a distance of approx. $10\,\mu$m to the camera sensor. The image is corrected for dark noise and signal fluctuations (cf. section 4.2). Right: Relative light output per camera pixel (area: $(4.65\,\mu\text{m})^2$) given by the pixels' signal values divided by the integrated signal over all pixels. The plot shows an increased light output towards the fibre edges.

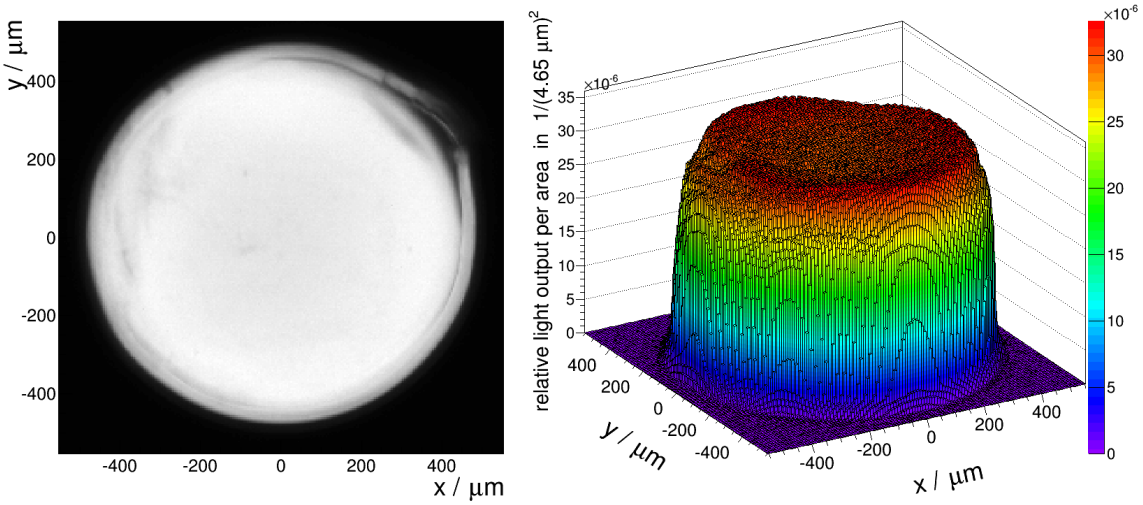


**Figure 4.9:** Left: Image of the end surface of the round multiclad WLS fibre at a distance of approx. $10\,\mu$m to the camera sensor. The image is corrected for dark noise and signal fluctuations (cf. section 4.2). Right: Relative light output per camera pixel (area: $(4.65\,\mu\text{m})^2$) given by the pixels' signal values divided by the integrated signal over all pixels. The light output increases towards the fibre edges. This increase is not as severe as for the the round singleclad fibre (fig. 4.8).

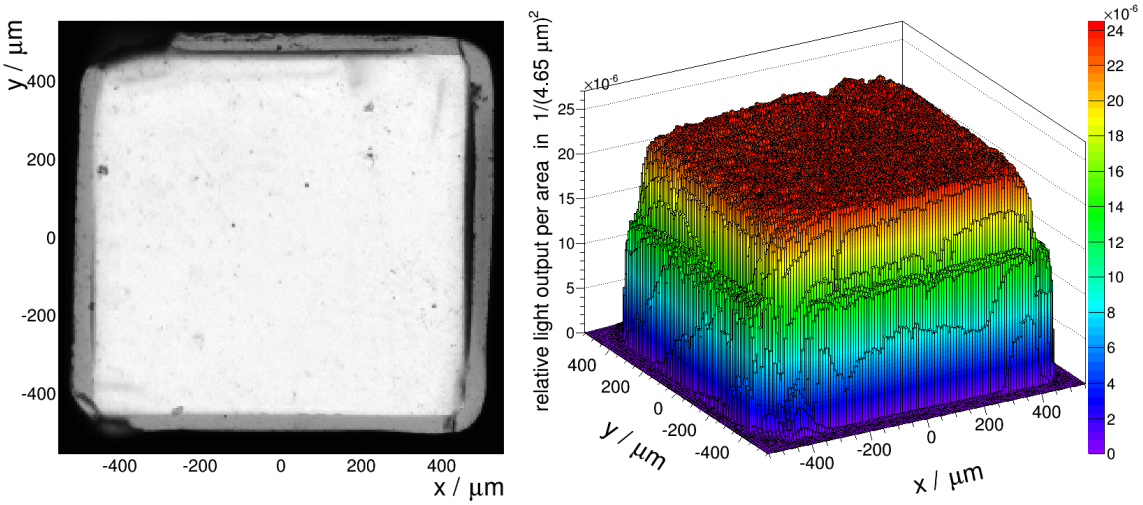


**Figure 4.10:** Left: Image of the end surface of the square multiclad scintillating fibre at a distance of approx. 10 $\mu$m to the camera sensor. The image is corrected for dark noise and signal fluctuations (cf. section 4.2). Right: Relative light output per camera pixel (area: $(4.65\,\mu\text{m})^2$) given by the pixels' signal values divided by the integrated signal over all pixels. The light output is distributed rather homogeneously across the fibre surface.

fibre core (fig. 4.10).

For a closer inspection, a profile of the spatial light output distribution through the fibre centre was determined for each fibre. It was obtained by taking the signal values of the central pixel array in x- or y-direction depending on which of those showed the least amount of core and cladding damage. The profiles were normalised to the integrated light output over the whole pixel array.

A comparison between figures 4.11 and 4.12 shows that the spatial light distribution is indeed more inhomogeneous for the round singleclad fibre. The light output per area close to the core edge is about 32% larger than at the centre for the singleclad light guide. The profile of the multiclad fibre shows a rise of only 9%.

Figure 4.13 shows the light output profile through the centre of the square fibre BCF-10MC. Apart from some minor fluctuations, the profile is flat across the whole fibre core. The peak at the edge of the profile ($x \approx 500\,\mu$m) arises from cladding damage inflicted during the fibre preparation. Here, the inner cladding is not in contact with the fibre core (cf. fig. 4.10).

To demonstrate the effect of a larger gap between sensor and fibre end, the light output profiles were obtained for selected images taken during the camera approach. Figures 4.14 to 4.16 show a comparison for each fibre between the distribution profile at the closest approach and those further away in steps of approximately 40 $\mu$m.

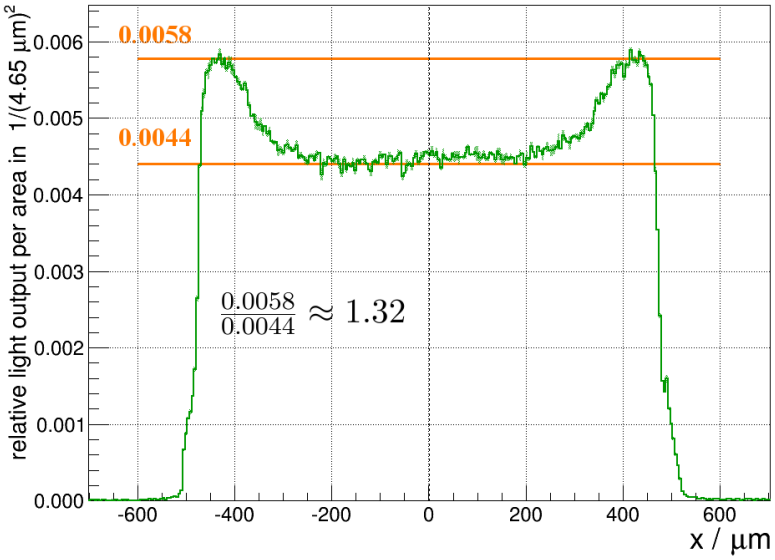


**Figure 4.11:** Light output profile through the centre of the round singleclad fibre measured with a camera sensor approx. 10 $\mu$m away from the fibre end (pixel size: $(4.65\,\mu\text{m})^2$). The plot shows the signal values along the central pixel array in x-direction ($y = 0\,\mu\text{m} = \text{const}$, see fig. 4.8) normalised to the integral over the profile. The light output per area increases towards the fibre edges and is approx. 32% higher than at the centre.

The profile progression for the round singleclad fibre (fig. 4.14) reveals that the distribution maxima decrease with larger distances. This leads to a more homogeneous illumination of the sensor. The steep rise in the light output towards the fibre edge can therefore be compensated by leaving a certain gap between sensor and fibre. However, the profile widens slightly when the fibre is retracted, resulting in a possible loss of light for small readout sensors.

For the round multiclad fibre (fig. 4.15) the maxima decrease as well when moving the fibre further away from the sensor. However, at the same time the edges of the distribution flatten severely. This leads to a more and more Gaussian trend of the profile with a small dip at the fibre centre. In this case, a gap between sensor and fibre does not lead to a more homogeneous light distribution but merely changes the type of inhomogeneity. Additionally, the widening of the profile with larger distances - and therefore the possibility of light loss between fibre and sensor - is more severe than for the singleclad fibre.

Figure 4.16 shows the progression of the light output profile for the square multiclad fibre. It can be seen that the formerly homogeneous distribution dissolves and widens with an increasing distance from the fibre. A gap between fibre and sensor therefore diminishes the efficiency of the fibre readout, if it depends on a homogeneous illumination of the used sensor. The progression shows that the effect of the previously described cladding damage

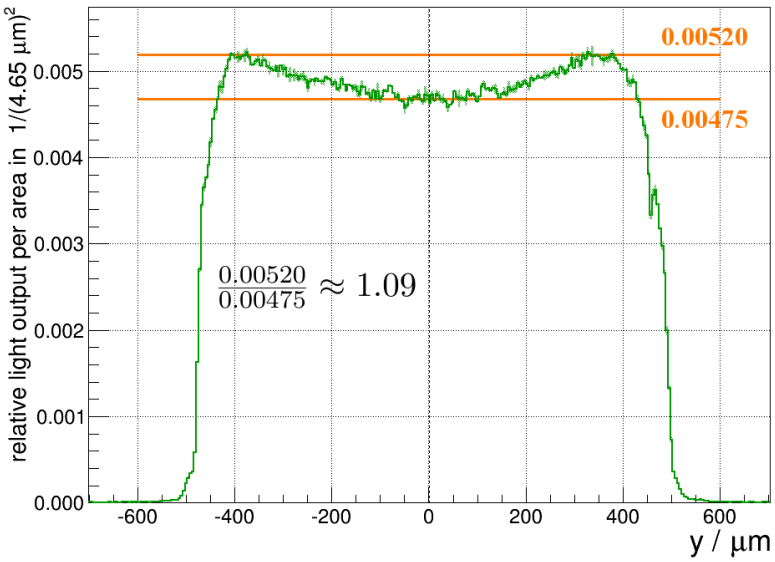


**Figure 4.12:** Light output profile through the centre of the round multiclad fibre measured with a camera sensor approx. 10 $\mu$m away from the fibre end (pixel size: $(4.65\,\mu\text{m})^2$). The plot shows the signal values along the central pixel array in y-direction ($x = 0\,\mu\text{m} = \text{const}$; see fig. 4.9) normalised to the integral over the profile. The light output per area increases towards the fibre edges. The increase is not as steep as for the round singleclad fibre (fig. 4.11). It amounts to approx. 9%.

at $x \approx 500\,\mu$m decreases with larger distances.

In conclusion it shows that the spatial light distributions of round optical fibres feature an inhomogeneity in the form of an increased light output towards the edges of the fibre. In the case of the singleclad fibre, the outer area of the fibre end surface is approx. 29% brighter than the centre. Using a round multiclad fibre can reduce the inhomogeneity down to approximately 10%. When interested in a light distribution as uniform as possible, a gap between readout sensor and the end of the singleclad fibre can be utilized to compensate the steep maxima in the light output.
The square multiclad fibre shows a flat spatial light distribution across the end surface. Therefore, a homogeneous illumination of a readout sensor can be achieved without the use of light mixers, if the fibre end is placed as close to the sensor as possible. A further advantage is that the fibre's square cross section matches the form of commonly used photo sensitive sensors (e.g. silicon photomultipliers [6]). In contrast to round optical fibres, this allows the use of the sensor's whole active area.
Based on the measured spatial light distributions, it shows that square multiclad fibres are the best candidates for an efficient fibre readout.

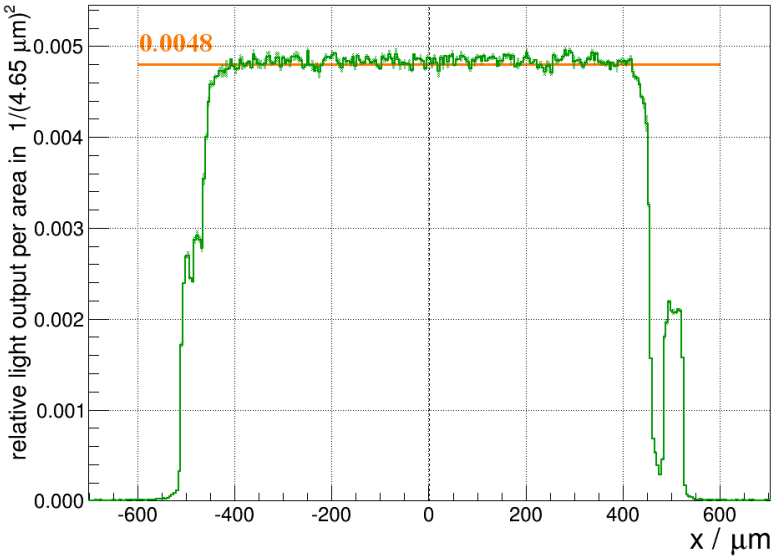


**Figure 4.13:** Light output profile through the centre of the square multiclad fibre measured with a camera sensor approx. $10\,\mu$m away from the fibre end (pixel size: $(4.65\,\mu\text{m})^2$). The plot shows the signal values along the central pixel array in x-direction ($y = 0\,\mu\text{m} = \text{const}$; see fig. 4.10) normalised to the integral over the profile. The light is very evenly spread across the fibre profile. The peak at $x \approx 500\,\mu$m results from damage inflicted on the cladding during the fibre preparation.

Unfortunately, an absolute comparison of the amount of light transported by the three examined fibres could not be conducted since the total amount of light coupled into each fibre could not be determined as a point of reference. This determination was prevented by the use of two different uncalibrated source LEDs as well as by the difference in the way the light was coupled into the light-guide or the WLS and scintillating fibre, respectively (cf. section 3.1). However, an absolute comparison between fibres of the same type but with different geometrical properties (shape and number of claddings) was conducted on simulated fibres. The results are shown in chapter 5.

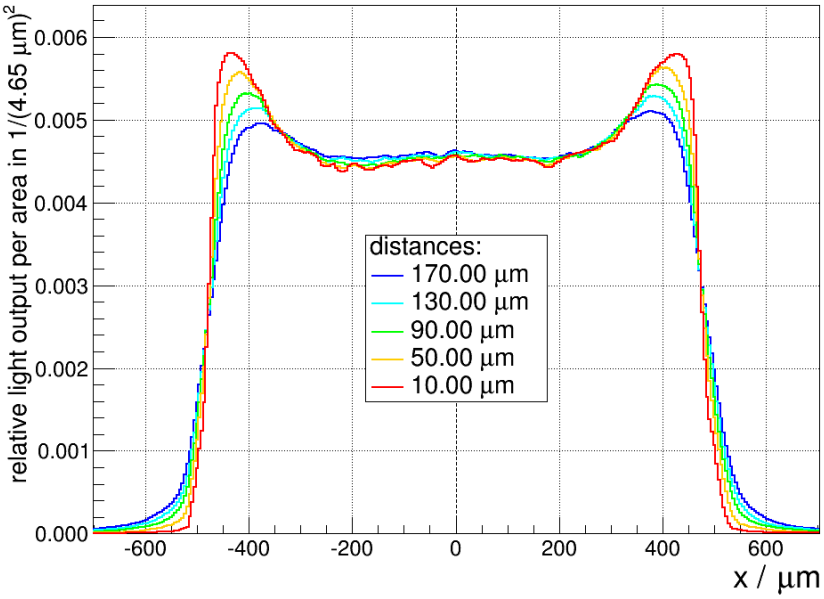


**Figure 4.14:** Light output profile through the centre of the round singleclad fibre measured with a camera sensor at varying distances towards the fibre end (pixel size: $(4.65\,\mu\text{m})^2$). Each graph shows the signal values along the central pixel array in x-direction ($y = 0\,\mu\text{m} = \text{const}$; see fig. 4.8) normalised to the integral over the respective profile. For a better comparison the uncertainties are not shown and the profiles are slightly smoothed. The comparison shows that the profile maxima decrease and the profile widens slightly for larger distances.

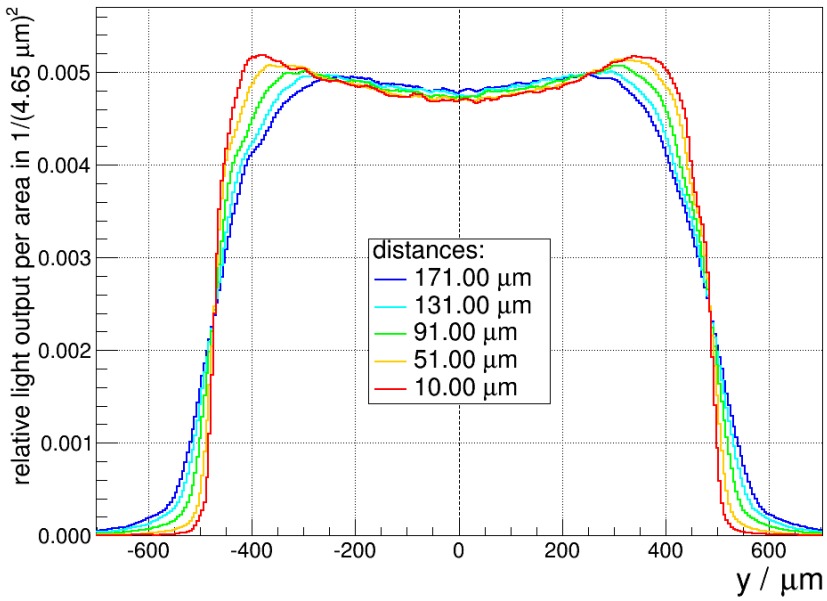


**Figure 4.15:** Light output profile through the centre of the round multiclad fibre measured with a camera sensor at varying distances towards the fibre end (pixel size: $(4.65\,\mu\mathrm{m})^2$). Each graph shows the signal values along the central pixel array in y-direction ($x = 0\,\mu\mathrm{m} = \text{const}$, see fig. 4.9) normalised to the integral over the respective profile. For a better comparison the uncertainties are not shown and the profiles are slightly smoothed. The profile maxima at the fibre edges decrease for larger distances and the profile assumes a more Gaussian trend with a small dip at the centre. The shown widening of the profile with larger distances is more rigorous than in the case of the singleclad fibre (fig. 4.14).

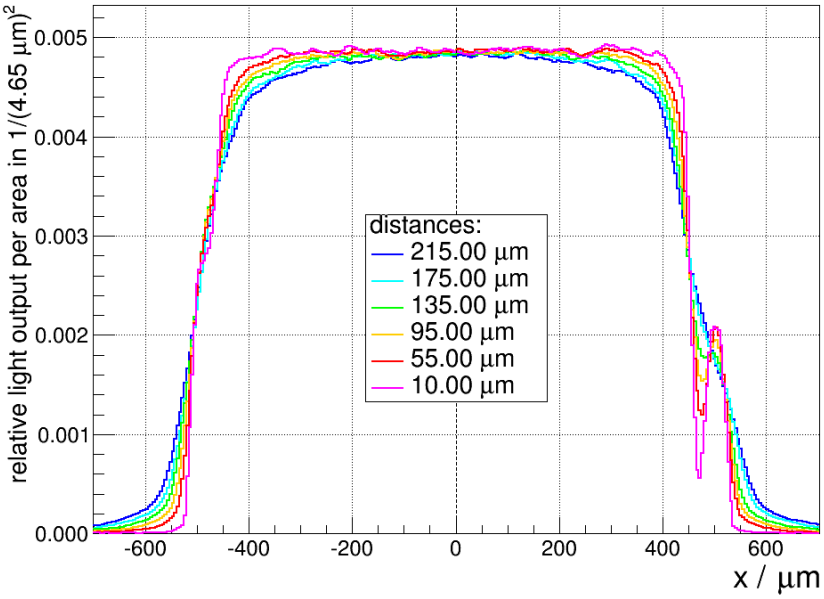


**Figure 4.16:** Light output profile through the centre of the square multiclad fibre measured with a camera sensor at varying distances towards the fibre end (pixel size: $(4.65\,\mu\text{m})^2$). Each graph shows the signal values along the central pixel array in x-direction ($y = 0\,\mu\text{m} = \text{const}$, see fig. 4.10) normalised to the integral over the respective profile. For a better comparison the uncertainties are not shown and the profiles are slightly smoothed. The homogeneous light distribution washes out and widens for increasing distances. Furthermore, the effect on the light distribution of the cladding damage at $x \approx 500\,\mu\text{m}$ decreases.

## 4.4 Measurement of the Angular Light Distribution

### 4.4.1 Experimental Procedure

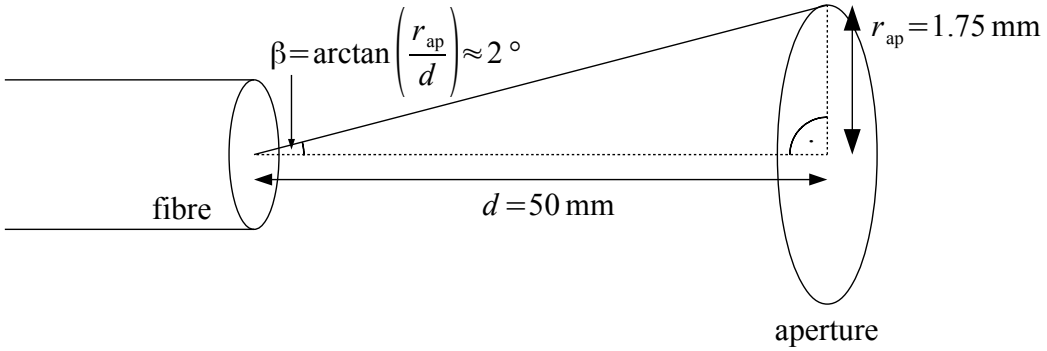


**Figure 4.17:** Schematic showing the construction of the angular acceptance $\beta$ of the aperture and, therefore, the angular resolution of the measurements of the angular light distribution. Not to scale.

To measure the angular distribution of the fibre light output with a good resolution, the angular acceptance of the camera system had to be kept as small as possible. As mentioned above, an adjustable aperture was therefore placed in front of the lens system at a distance of $d = 50\,\text{mm}$ to the examined fibre end (see fig. 3.12). The radius of the aperture was set to $r_{\text{ap}} = 1.75\,\text{mm}$ which leads to an angular acceptance of $\beta = 2°$ (see fig. 4.17). This means that when looking at the fibre end at an angle $\delta$, rays exiting at angles between $\delta \pm 2°$ were detected. Assuming a uniform distribution of the exiting angles within the angular acceptance, the uncertainty on all measured exiting angles is given by $\sigma_\delta = 4°/\sqrt{12} = 1.15°$. As can be seen in figure 4.18, decreasing the aperture radius any further leads to a blurring of the image due to diffraction on the aperture's edges.
From the fibre end's point of view, the round aperture covers a solid angle $\omega$ of

$$\omega = 2\pi \cdot \int_0^\beta \sin(\theta')\mathrm{d}\theta' = 2\pi \cdot (1 - \cos(\beta)) \tag{4.5}$$

which is used later on in the analysis.
After setting the aperture, the camera system was aligned parallel to the fibre axis ($\delta = 0°$). Using the positioning unit the fibre was then brought into focus. Starting there, the camera was pivoted in steps of 2° up to an angle of $\delta = 90°$. The step size was chosen to match the angular acceptance of the camera system. At each angular step the fibre position was re-adjusted and a series of three frames and three dark frames was taken.
For the square fibre two measurement series were conducted. One with the fibre edges aligned parallel to the sensor axes and one with the fibre rotated by 45° about the fibre

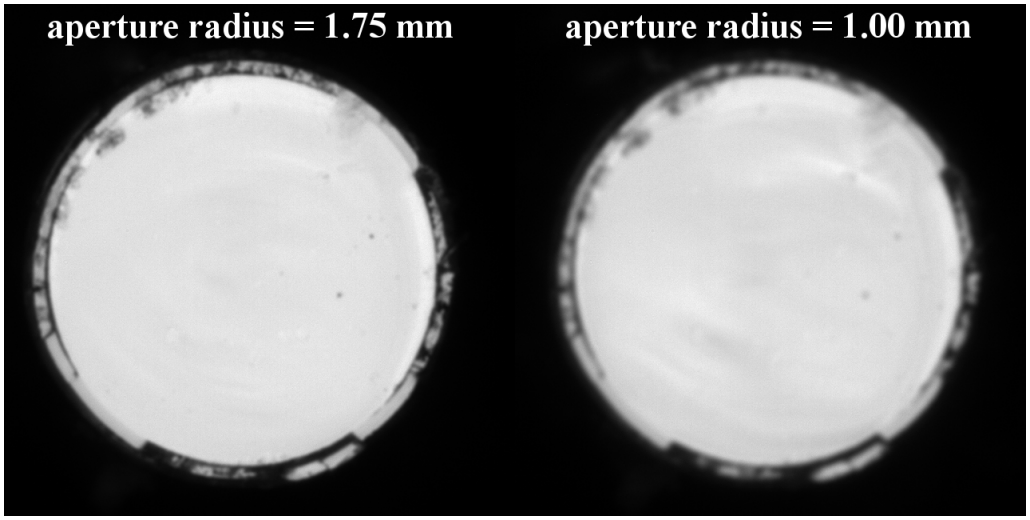


**Figure 4.18:** Photos of a fibre end (frontal view, $\delta = 0°$) taken with an aperture radius of 1.75 mm and 1.00 mm. The right image is notably blurred due to light diffraction on the aperture's edges. This sets a limit on the minimal aperture radius and, therefore, the angular acceptance of the camera system used to measure the angular light distribution.

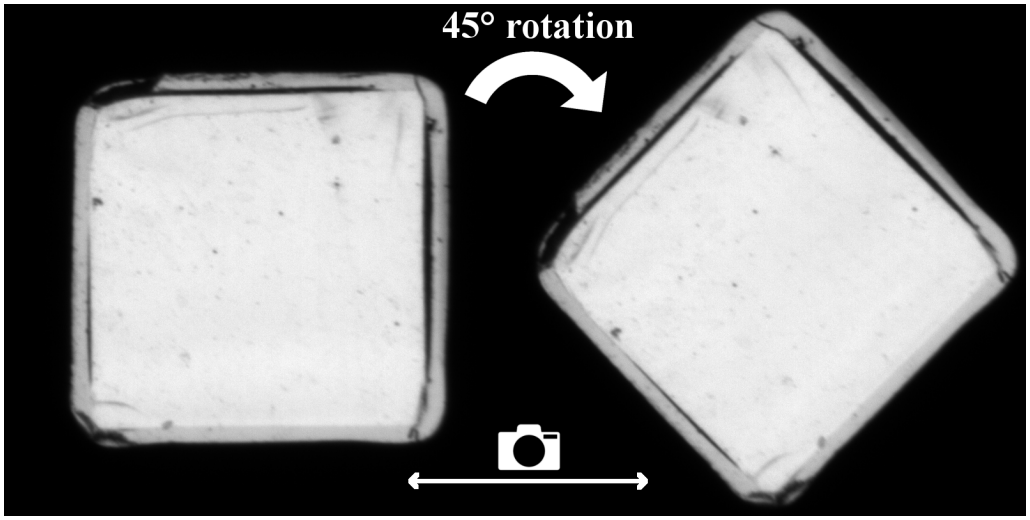


**Figure 4.19:** The two orientations of the square fibre for which the angular light distribution was determined to examine possible deviations from a radial symmetry (frontal view, $\delta = 0°$).

axis (see fig. 4.19). This was done to examine possible deviations from a radial symmetry of the angular light distribution.

The magnification of the lens system was set to 3× for the round fibres to get full-frame images of the fibre end. For the square fibre the magnification was decreased to 2× so that the rotated fibre end was still fully visible.

### 4.4.2 Results

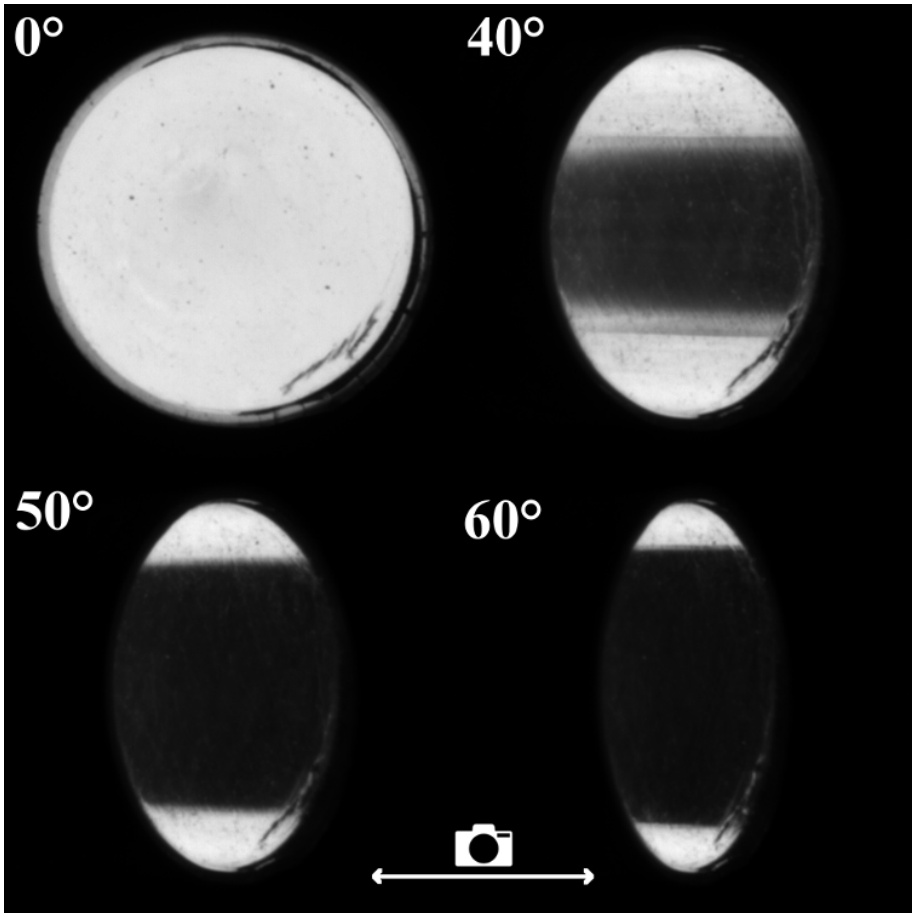


**Figure 4.20:** Image series of the end surface of the round singleclad fibre taken at increasing angles during the measurement of the angular light distribution (fibre distance to camera: 50 mm). The increasing dark area along the horizontal axis shows that meridional rays are suppressed for larger exiting angles (see fig. 4.24).

Figures 4.20 to 4.23 show obtained images of the examined fibres at the angles $\delta = 0°, 40°, 50°$ and $60°$. In case of the round fibres the light output decreases at the fibre centre when observing the end surface at increasing angles. This can be understood when considering the schematic shown in figure 4.24. It shows two light rays exiting the fibre end towards the camera at different points on the surface. The distance between the exit point and the horizontal axis correlates to their minimal approach $\rho$ to the fibre centre (cf. section 2.3.1). Light rays exiting at the horizontal axis are therefore meridional rays while those exiting at a distance are skew rays.

The dark surface area parallel to the horizontal axis shows that meridional rays are not propagated inside the fibre, if their exiting angle would be larger than the acceptance angle of the examined fibre. For increasing angles only skew rays spiralling along the fibre closer

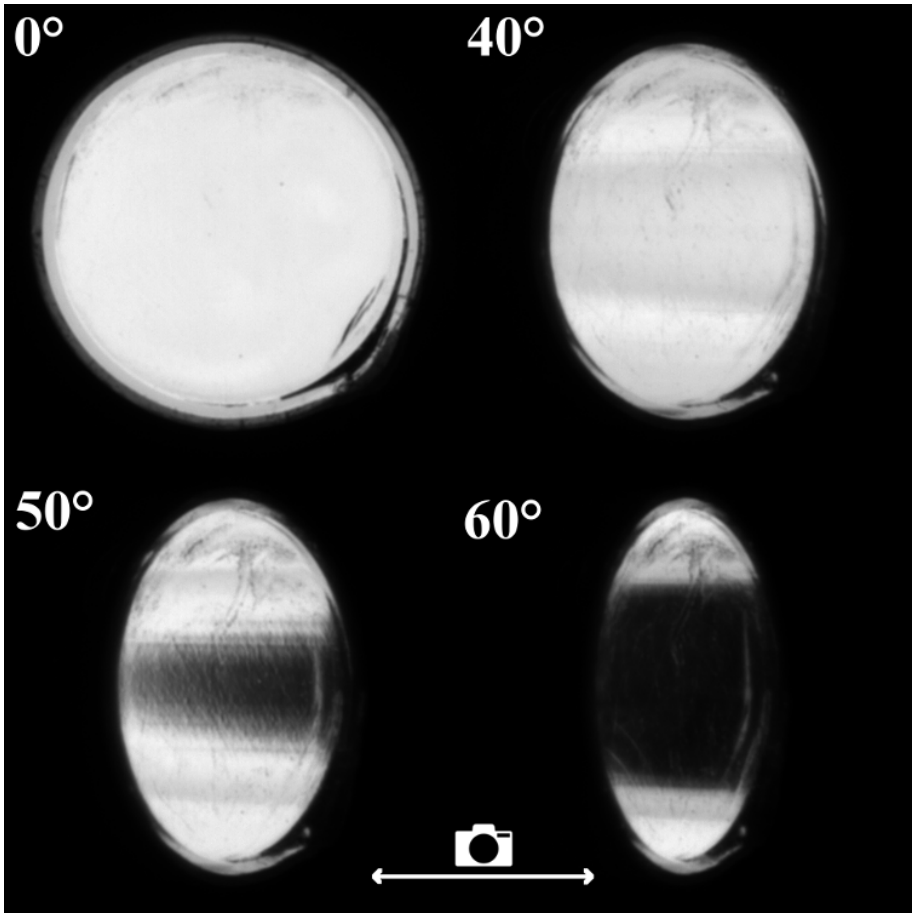


**Figure 4.21:** Image series of the end surface of the round multiclad fibre taken at increasing angles during the measurement of the angular light distribution (fibre distance to camera: 50 mm). In comparison to the round singleclad fibre (fig. 4.20), the dark area along the horizontal axis increases more slowly. This shows that additional meridional rays are propagated as cladding modes.

to the edges can be transported.
For the round multiclad fibre the dark area increases more slowly than for the singleclad fibre which means that its numerical aperture is increased by the additional cladding.
The square fibre shows an even light output across the fibre core at all angles for both orientations. The uniform light distribution shows that, in this case, meridional and skew rays are not confined to specific areas of the fibre profile and can therefore not be distinguished by the point of exiting relative to the horizontal axis. The observations match with the considerations in section 2.3.

As a measure of a fibre's light output per exiting angle interval $\delta \pm 2°$ (set by the readout system's angular acceptance $\beta = 2°$) the sum $I'(\delta)$ of all (corrected) irradiance levels $l_i$ measured by the $N_{\mathrm{px}}$ individual camera pixels was calculated for each angular camera

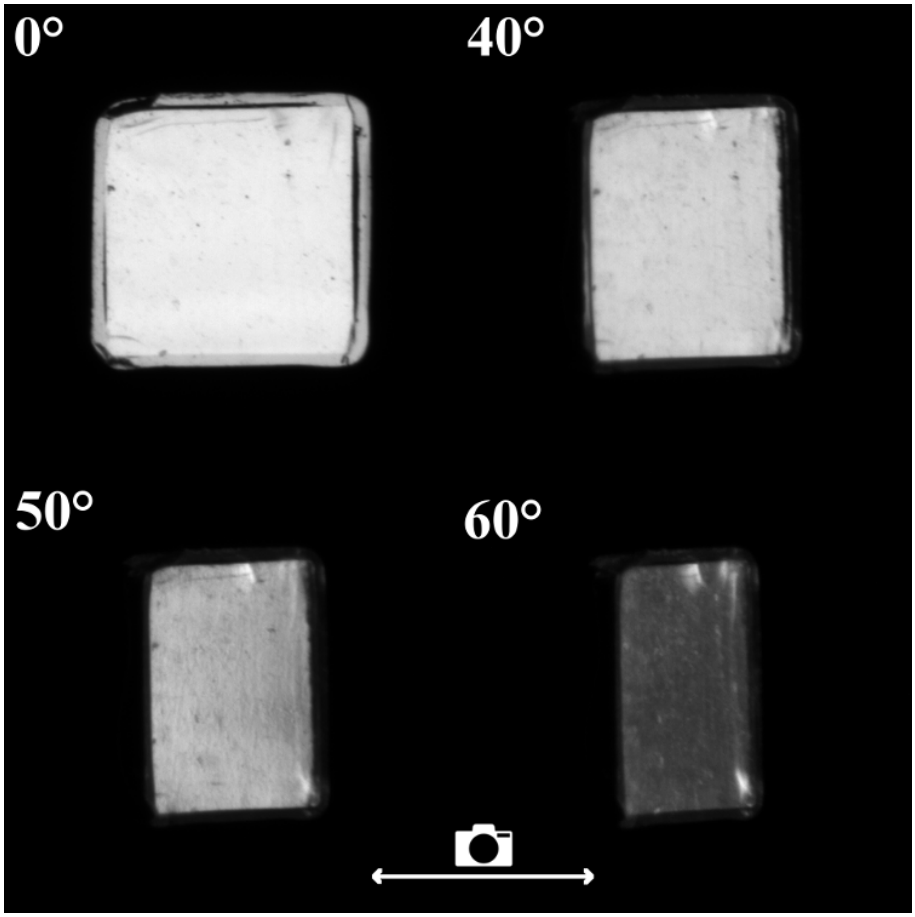


**Figure 4.22:** Image series of the end surface of the square multiclad fibre taken at increasing angles during the measurement of the angular light distribution (fibre distance to camera: 50 mm). The surface shows an evenly spread light output for all shown examination angles.

position $\delta$ using

$$I'(\delta) = \sum_{i=1}^{N_{\mathrm{px}}} l_i \quad . \tag{4.6}$$

This sum had to be re-weighted to account for light that exits the fibre at angles between $\delta \pm 2°$, but misses the aperture because of its azimuthal orientation.

Figure 4.25 shows the construction of the re-weighting factor $g(\delta)$. The red area indicates the camera system's aperture covering the already mentioned solid angle $\omega$ (see eq. 4.5 and fig. 4.24). All light rays exiting the fibre inside this solid angle are detected by the camera.

The blue sphere segment shows the solid angle $\Omega(\delta)$ including both detected and missed light rays with an exiting angle $\delta \pm 2°$. It is confined by an imagined rotation of the aperture by $2\pi$ about the fibre axis. It can be calculated to

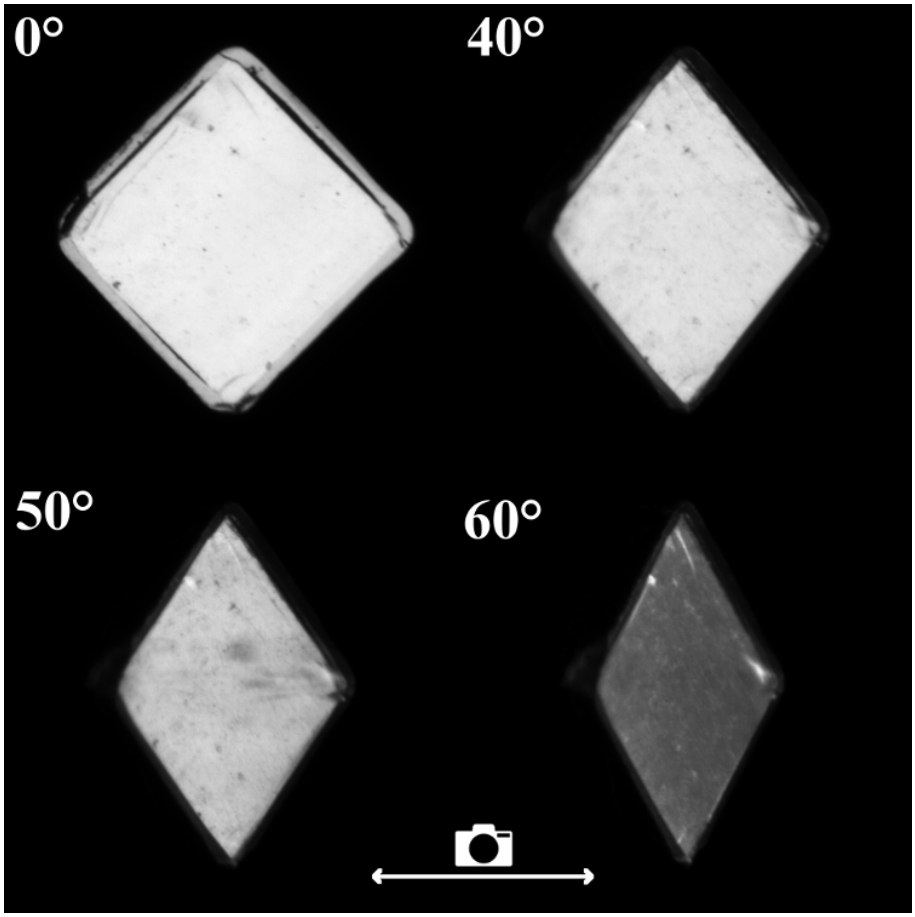


**Figure 4.23:** Image series of the rotated end surface of the square multiclad fibre taken at increasing angles during the measurement of the angular light distribution (fibre distance to camera: 50 mm). Similar to the un-rotated fibre end (fig 4.22), the surface shows a rather homogeneously distributed light output for all shown examination angles.

$$\Omega(\delta) = \begin{cases} 2\pi \cdot \int_{\delta-\beta}^{\delta+\beta} \sin(\theta')\mathrm{d}\theta' = 2\pi \cdot (\cos(\delta-\beta) - \cos(\delta+\beta)) & \text{for } \delta > 0° \\ 2\pi \cdot \int_{0}^{\beta} \sin(\theta')\mathrm{d}\theta' = 2\pi \cdot (1 - \cos(\beta)) = \omega & \text{for } \delta = 0° \end{cases} . \quad (4.7)$$

The ratio of those two solid angles gives the re-weighting factor

$$g(\delta) = \frac{\omega}{\Omega(\delta)} = \begin{cases} \frac{1-\cos(\beta)}{\cos(\delta-\beta)-\cos(\delta+\beta)} & \text{for } \delta > 0° \\ 1 & \text{for } \delta = 0° \end{cases} . \quad (4.8)$$

The azimuthally integrated light output per polar exiting angle interval $\delta \pm 2°$ is then determined by calculating the weighted sums

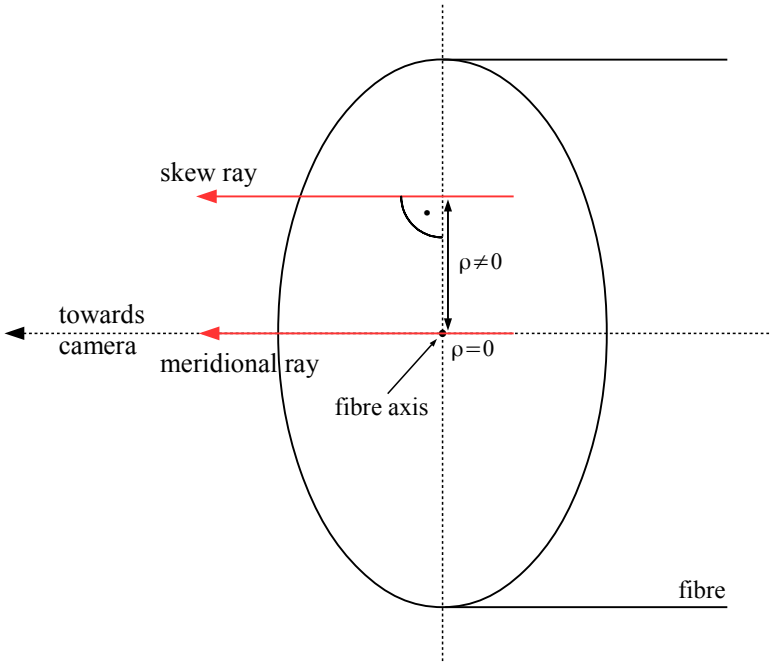


**Figure 4.24:** Schematic of a meridional ray and a skew ray exiting the fibre end towards the camera. They can be distinguished by their distance to the horizontal axis at the exit point (cf. section 2.3.1).

$$I(\delta) = \frac{I'(\delta)}{g(\delta)} \tag{4.9}$$

and plotting them against the respective $\delta$. The uncertainty on each sum was calculated by using Gaussian error propagation on the signal uncertainties of all camera pixels (see section 4.2). Due to the large number of pixels, this statistical uncertainty on the light output at each exiting angle (interval) becomes very small (usually in the order of 0.01%) and is therefore not shown in the following plots.

Figures 4.26, 4.27 and 4.28 show the determined light output per exiting angle interval $\delta\pm2°$ for each fibre as a function of the angular camera position $\delta$. The plots are normalised to the total light output integrated over all exiting angles. Each figure also features a cumulative plot of the light output which shows the fraction of the fibre light with an exiting angle smaller than a given $\delta$. For the square fibre the distributions for both orientations of the fibre end were averaged since they have a very similar shape as can be seen in figure 4.29.

The vertical lines plotted together with the angular distributions represent the maximal exiting angles $\delta_{\text{max}}^{\text{core}}$ and $\delta_{\text{max}}^{\text{clad}}$ for meridional core and cladding modes, respectively. They were calculated using equations 2.13 and 2.14 and the refractive indices shown in table 4.1. All three fibres show a global maximum in their light output per angle at $\delta_{\text{max}}^{\text{core}}$ (slight

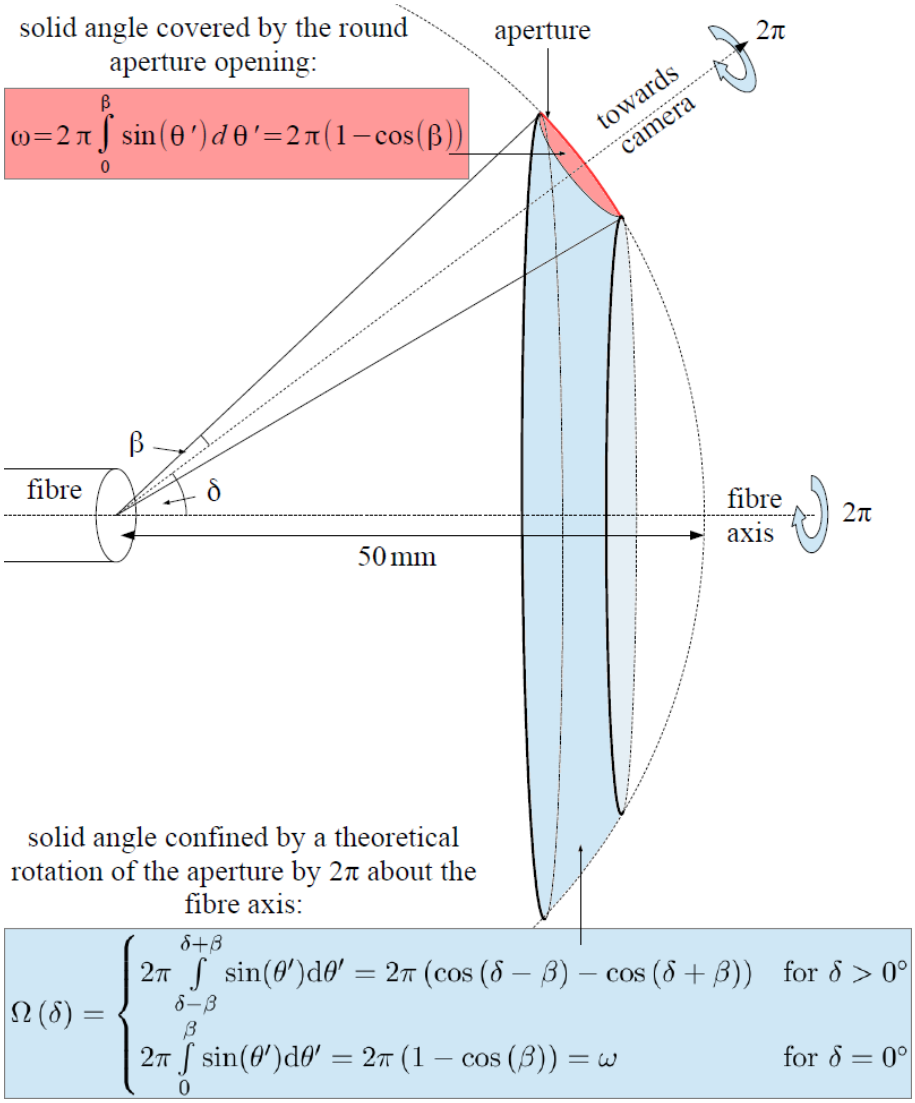


**Figure 4.25:** Schematic that shows the solid angles used in the re-weighting (eq. 4.9) of the measured fibre light output per exiting angle interval $\delta \pm \beta$ ($\beta = 2°$ being the camera system's angular acceptance, see fig. 4.17). The red area indicates the round aperture which covers the (constant) solid angle $\omega$ from the fibre end's point of view. It includes all detected light rays with polar exiting angles $\delta \pm \beta$. The blue sphere segment represents the solid angle $\Omega(\delta)$ which includes both detected and missed light rays with the same exiting angle but a possible different azimuthal orientation. It increases with larger exiting angles.

deviations in the order of 1° are compatible with the estimated uncertainty $\sigma_\delta = 1.15°$ on the measured exiting angle). Beyond this, all distributions decrease monotonously towards larger exiting angles eventually reaching zero at the maximal possible angle $\delta = 90°$.
The distribution maximum at $\delta_{\max}^{\text{core}}$ is composed of both skew rays and meridional core modes. The steep decrease in the light output for exiting angles exceeding $\delta_{\max}^{\text{core}}$ - which

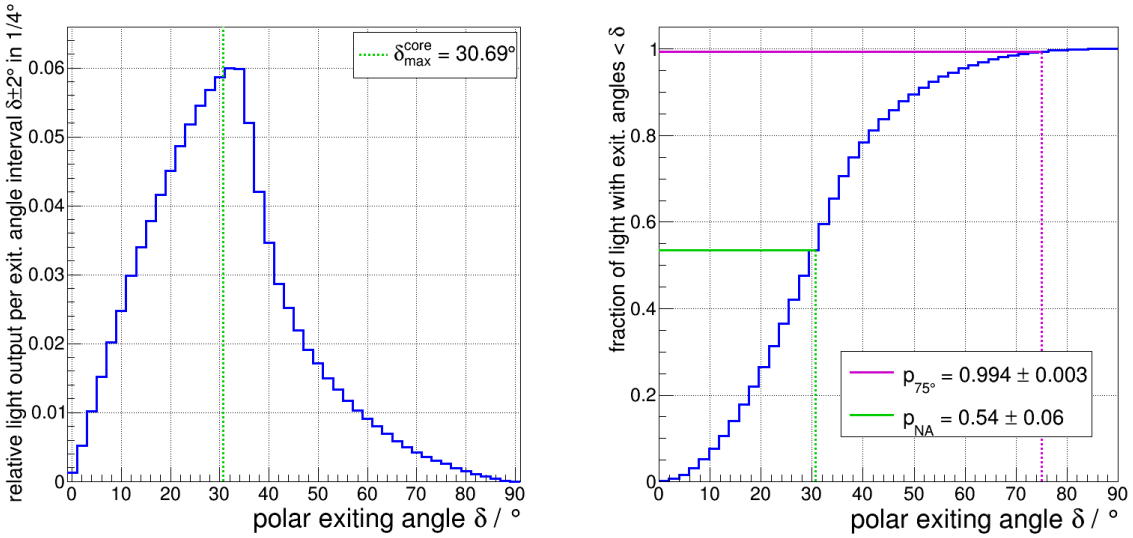


**Figure 4.26:** Left: Light output per polar exiting angle interval $\delta \pm 2°$ (azimuthally integrated; see eq. 4.9) of the round singleclad fibre (measured in angular steps of 2°) relative to the integral over all examined angles. The maximum lies at the maximal exiting angle $\delta_{\text{max}}^{\text{core}}$ of meridional core modes. Right: The corresponding integrated light output. It shows that more than 99% of the transported light exits the fibre at angles smaller than 75°. Only $(54 \pm 6)\%$ of the light exits at angles inside the fibre's numerical aperture $(0° - \delta_{\text{max}}^{\text{core}})$.

means a suppression of the meridional rays - shows that the majority of light transported in an optical fibre is propagated via meridional core modes with the maximal possible polar angle.

At angles around $\delta_{\text{max}}^{\text{clad}}$, the multiclad fibres feature a higher light output in comparison to the singleclad fibre. This increased light output is expected since the additional cladding allows for meridional and skew cladding modes with larger exiting angles to contribute to the light output in this angular region. The bump in the distribution is more shallow for the square fibre than for the round one.

That the bump at $\delta_{\text{max}}^{\text{clad}}$ is not as distinct as the maximum at $\delta_{\text{max}}^{\text{core}}$ means, that cladding modes are suppressed in comparison to rays confined to the fibre core. This can be understood when considering that the core-cladding interface is not perfectly smooth. This may lead to the scattering of light at imperfections when intersecting with the interface. Those deflections can result in angles too steep for TIR in the following progression of a light ray. Cladding modes intersect with the core-cladding interface more often than core modes (twice for every reflection at the cladding-cladding interface) and are therefore more prone to leak out of the fibre due to the microscopic roughness of the interface (see also fig. 5.10 and 5.11 which show comparisons between measured results and simulated fibres with an ideal core-cladding interface).

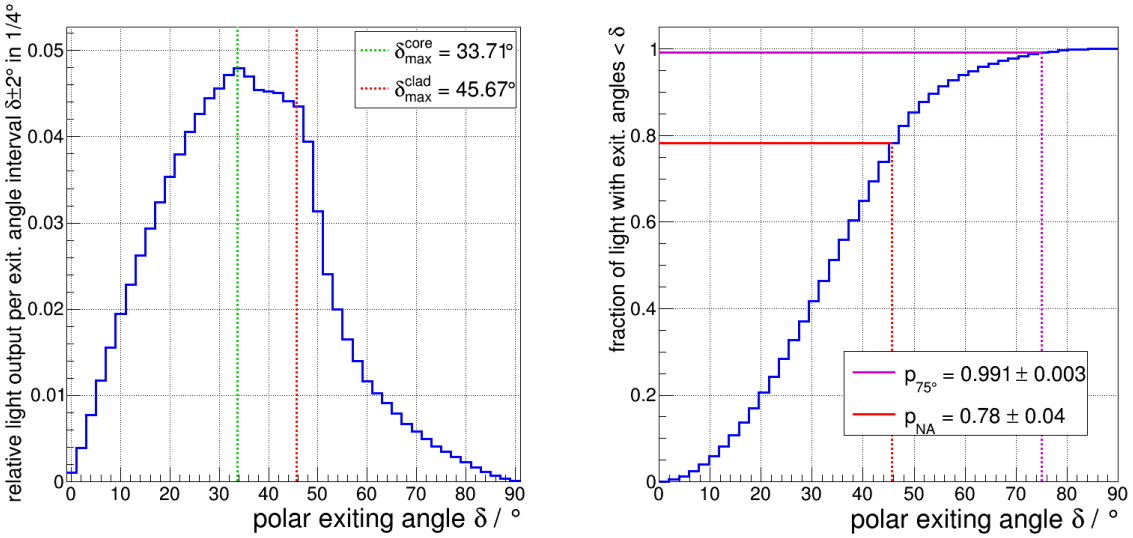


**Figure 4.27:** Left: Light output per polar exiting angle interval $\delta \pm 2°$ (azimuthally integrated; see eq. 4.9) of the round multiclad fibre (measured in angular steps of 2°) relative to the integral over all examined angles. The maximum lies at the maximal exiting angle $\delta_{\text{max}}^{\text{core}}$ of meridional core modes. In comparison to the singleclad fibre (fig. 4.26), the light output for angles around $\delta_{\text{max}}^{\text{core}}$ is increased since cladding modes contribute to the light output in this angular region. Right: The corresponding integrated light output. It shows that about 99% of the transported light exits the fibre at angles smaller than 75°. Only $(78 \pm 4)\%$ of the light exits at angles inside the fibre's numerical aperture $(0° - \delta_{\text{max}}^{\text{clad}})$.

To estimate how efficiently each examined fibre can be read out with silicon photomultipliers (SiPMs), the percentage $p_{75°}$ of light exiting the fibre at angles smaller than 75° was obtained. As concluded in [7], the relative detection efficiency for photons hitting the sensitive surface at angles larger than 75° deceeds 90% for an SiPM manufactured by Hamamatsu. The relative PDE decreases rapidly for even larger angles of incidence. Therefore, $p_{75°}$ is an estimator for how much of the exiting light can be detected by an SiPM.

For each fibre, $p_{75°}$ was obtained from the respective cumulative angular distribution. Since the angular step size used during the measurements is 2°, the uncertainty $\sigma_{p_{75°}}$ was determined by calculating $|p_{75°} - p_{73°}|$ and $|p_{75°} - p_{77°}|$ and choosing the larger of the two values. The obtained values are shown together with the cumulative angular distributions and are listed in table 4.3 as well.

It was found that for all three examined fibres, $p_{75°}$ is about 99%. Thus, almost the entirety of the propagated light exits the fibre at angles with a corresponding SiPM photon detection efficiency above 90%. Therefore, light losses due to the angular dependency of PDE are minimal and the examined types of fibre can be read out efficiently with SiPMs.

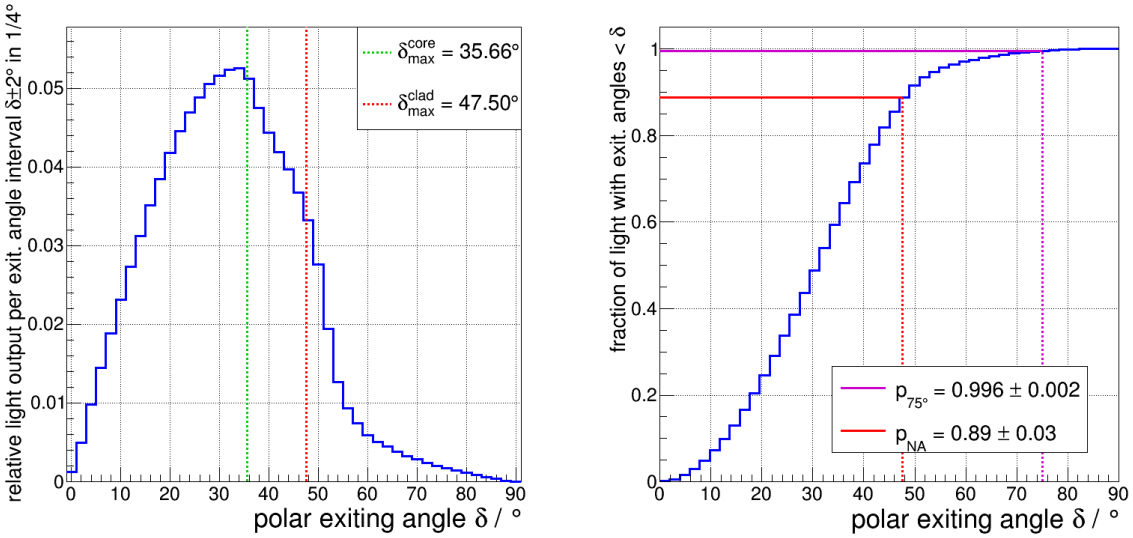


**Figure 4.28:** Left: Light output per polar exiting angle interval $\delta \pm 2°$ (azimuthally integrated; see eq. 4.9) of the square multiclad fibre (measured in angular steps of 2°) relative to the integral over all examined angles. The maximum lies at the maximal exiting angle $\delta_{\text{max}}^{\text{core}}$ of meridional core modes. In comparison to the singleclad fibre (fig. 4.26), the light output for angles around $\delta_{\text{max}}^{\text{core}}$ is increased since cladding modes contribute to the light output in this angular region. Right: The corresponding integrated light output. It shows that more than 99% of the transported light exits the fibre at angles smaller than 75°. Only $(89 \pm 3)\%$ of the light exits at angles inside the fibre's numerical aperture $(0° - \delta_{\text{max}}^{\text{clad}})$.

| fibre type | $p_{75°}$ | $p_{\text{NA}}$ |
|---|---|---|
| round singleclad | $0.994 \pm 0.003$ | $0.54 \pm 0.06$ |
| round multiclad | $0.991 \pm 0.003$ | $0.78 \pm 0.04$ |
| square multiclad | $0.996 \pm 0.002$ | $0.89 \pm 0.03$ |

**Table 4.3:** $p_{75°}$ represents the percentage of light that exits the respective fibre at angles smaller than 75°. $p_{\text{NA}}$ is the percentage of light that exits at angles inside the fibre's numerical aperture (cf. section 2.3.1).

In many setups, optical fibres are not directly read out by a sensor but coupled to further fibres (usually light guides) or other devices like collimators or diffusers. Those are commonly designed to match the numerical aperture of the coupled fibre. It is therefore of interest to know how much of the transported light exits at angles smaller than the fibre's acceptance angle. This percentage $p_{\text{NA}}$ was obtained from the integrated angular light distribution for each fibre. The acceptance angle is $\delta_{\text{max}}^{\text{core}}$ or $\delta_{\text{max}}^{\text{clad}}$ for single- and multiclad fibres, respectively (cf. section 2.3.1). The uncertainties on the percentages $p_{\text{NA}}$ are calculated similar to those of $p_{75°}$. The determined values are given in table 4.3.

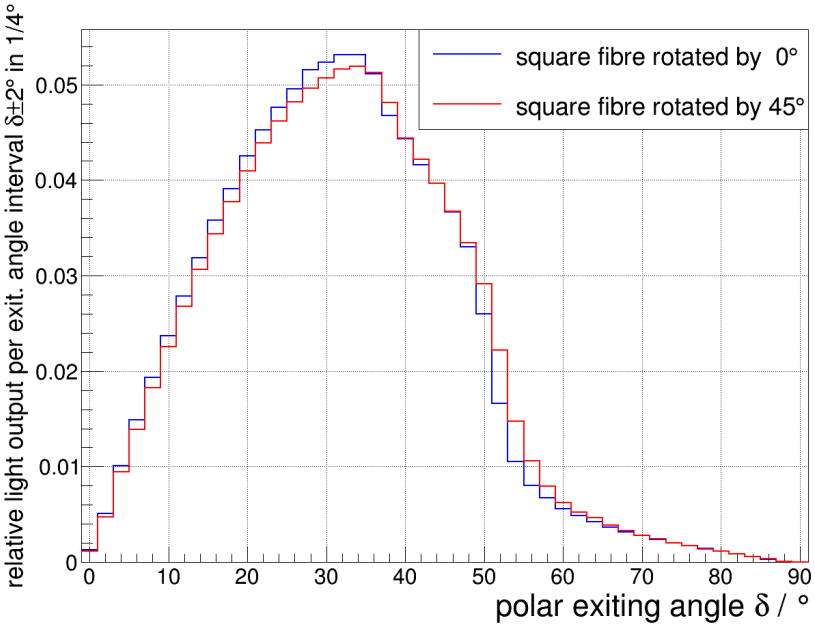


**Figure 4.29:** Comparison of the angular light output distribution for different orientations of the square multiclad fibre (cf. fig. 4.28). Since their shape is very similar, the average of the two distributions was used for any analysis of the characteristics of the square fibre.

It can be seen that for the round singleclad fibre only $(54 \pm 6)\%$ of the light exits at angles in its numerical aperture. Adding a second cladding to the fibre can increase this percentage up to $(78 \pm 4)\%$. For the square multiclad fibre, $p_{\mathrm{NA}}$ reaches an even higher value of $(89 \pm 3)\%$. This shows that the later type of fibre is the best choice for coupling light into a device with a maximal angular acceptance matching the fibre's numerical aperture. But even in this case about 10% of the transported light might be lost.

In conclusion it shows that for all three examined fibres the majority of the fibre light exits at the acceptance angle $\delta_{\mathrm{max}}^{\mathrm{core}}$ of meridional core modes. Adding a second cladding to a fibre increases the light output at angles around $\delta_{\mathrm{max}}^{\mathrm{clad}}$ due to the propagation of cladding modes. It seems that cladding modes are not propagated as efficiently as core modes due to light losses at the core-cladding interface.
For each fibre type almost the entire light exits at angles smaller than 75° which allows a fibre readout with a photon detection efficiency higher than 90% when using SiPMs.
When coupling light from a fibre into another device, it has to be kept in mind, that only a fraction of the light is successfully transmitted if the angular acceptance of the device at hand is limited to the respective fibre's numerical aperture. For the square multiclad fibre more light is coupled in comparison to the round fibres. The light loss, however, is still significant. Therefore, the numerical aperture of a fibre is not a good parameter to design

experimental setups when preserving as much of a light signal as possible is a crucial point, because for all examined fibres a noticeable percentage of the transported light exits at angles larger than the respective acceptance angle.

# 5 Fibre Simulation

As mentioned above, it is a vital part of almost any modern particle physics experiment to simulate the used detector. This helps to reveal flaws in the design and gives the scientists a beforehand estimation of how the detector will behave during the actual experiment later on. For example, a simulation can show in which energy region the detector will be sensitive, what level of efficiency it will reach, or how the outgoing signal will look like. Simulations are an important part of the data analysis as well.
Detailed simulations usually require high programming abilities and a lot of time in order to be correctly setup and run. A collection of C++ classes that simplifies these tasks was developed at our institute (III$^{rd}$ Physics Institute A, RWTH Aachen University). This package named GODDeSS[1] provides physicists with the software tools to easily create simulations of experimental setups including scintillator tiles and different types of optical fibre inside the widely used Geant4 simulation framework [10].
The simulation can only lead to reliable results when the GODDeSS classes are correctly implemented. To test the proper functionality of the classes used to simulate optical fibres and reveal improvement possibilities, the previously examined fibres and their light exiting characteristics were simulated. The results were then compared to the measured properties and occuring differences were examined and discussed.

## 5.1 Setup of the Simulation

The simulated setup for each fibre consisted of three parts: A representation of the examined fibre, a light source that reproduces the actual light coupling, and a sensor detecting the light exiting the fibre (see fig. 5.1). All these components can be defined using the GODDeSS classes.
In each case the simulated fibre was defined with the help of a properties file which could later be read by the simulation program. The properties file features the respective fibre type, its geometrical properties and the qualities of the used materials and dopants.
The properties were obtained from the respective specification sheet (see table 4.1). Unfortunately, the materials' refractive indices were given as constant values only. In the actual case, the refractive indices are wavelength dependent. To get a more accurate simulation of the WLS and scintillating fibres, the wavelength dependencies were obtained from [30]. For the FP claddings the dependency could not be determined. Since both FP and PMMA

[1] Geant4 Objects for Detailed Detectors with Scintillators and SiPMs. URL: https://forge.physik.rwth-aachen.de/projects/goddess-package

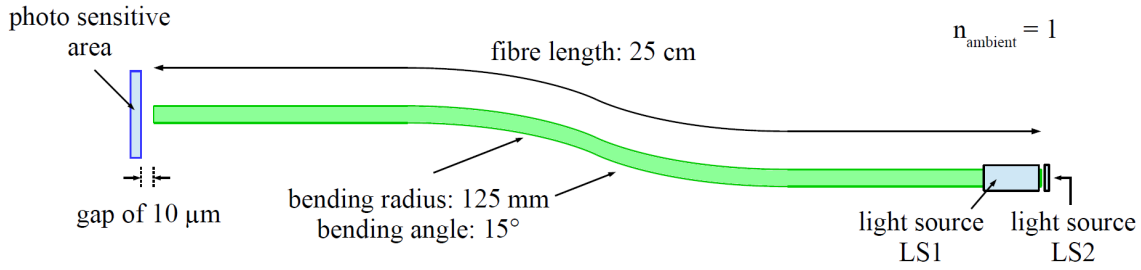


**Figure 5.1:** Schematic of the simulation setup. The slight s-shape of the simulated fibre accounts for any bending of the real fibre. The gap between fibre and photo sensor matches the gap between camera and fibre end surface during the measurements of the spatial light distribution. Either light source LS1 or LS2 is used for indirect or direct light coupling (see fig. 5.2). The simulated fibres were surrounded by a vacuum with a refractive index of $n_{\text{ambient}} = 1$.

are acrylate polymers, one expects the refractive index of FP to change similar to that of PMMA. As can be seen in table 4.1, the difference of the refractive indices for FP and PMMA amounts to $-0.09$ for both WLS and scintillating fibre. Therefore, the obtained values of the wavelength-dependent refractive index of PMMA were subtracted by 0.09 and used as a substitute for the FP cladding. The attenuation length of propagated photons was set to 3.5 m.
In case of the light guide, the constant refractive indices given in the specification sheet were used. Here, light is coupled directly into the fibre (without getting absorbed and re-emitted) by a monochromatic light source. Therefore, wavelength and corresponding refractive indices are the same for each simulated photon. For the light guide, the photon attenuation length was set to 19.3 m.

To match the actually examined fibres, the simulations involved 25 cm long pieces of fibre (cf. section 4.1) surrounded by a vacuum with a refractive index of $n_{\text{ambient}} = 1$. As can be seen in figure 5.1 those were arranged with a slight s-shaped bending which hinders light from being propagated inside the fibre without being reflected at one of the interfaces at least once. In the real case the fibres were bent by the long storage on fibre spools as well as by a movement of the examined fibre end with the positioning unit relative to the integrating sphere port that held the opposing fibre end. The exact shape of the bending differed from measurement to measurement and was not determined. The shape as well as the values for bending radius and angle used in the simulation could therefore only be estimated to resemble the conditions during the measurements. However, the simulated light exit characteristics for a bent and a straight fibre (shown in fig. A.7 in the appendix) differ only slightly compared to the later presented deviations between simulations and measurements. Adding or omitting the bending was therefore not essential for the simulations and comparisons described in the following.

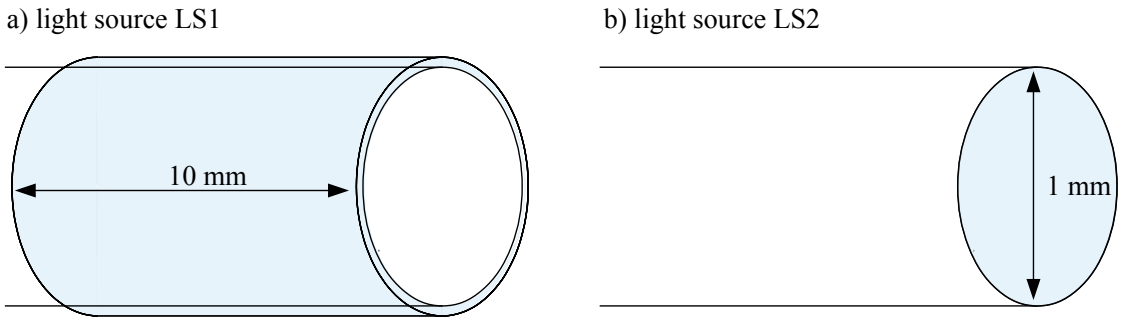


**Figure 5.2:** Simulated light sources used to reproduce the indirect (LS1) and direct (LS2) light coupling in the actual measurements. The blue areas indicate the surfaces over which the starting point of the simulated photons are distributed homogeneously. LS1 is used for the simulation of WLS and scintillating fibres while LS2 is used in case of light guides.

The light source of the experimental setup was modelled by simulating optical photons entering the fibre at one of its end tips. The photon distribution was designed to match the uniform spread of light across the fibre tip achieved by the integrating sphere (cf. section 3.1). In the case of the WLS and scintillating fibres, the starting position of the photons were allocated homogeneously over a cylindrical surface surrounding the last 1 cm of the fibre (see fig 5.2a). For the light guide the simulated photons were distributed evenly across the fibre end surface (fig. 5.2b). In both cases the direction of the photons were assigned randomly in the $2\pi$ hemisphere between the respective photon starting point and the fibre. The photon energy matched the peak wavelength of the LEDs used in the actual setup.

To detect the exiting light, a photo sensitive area was simulated at the fibre end opposing to the light source. It registered the position and direction of the detected photons from the fibre which were saved as a text file for further analysis. A small gap of $10\,\mu$m between fibre end and sensor was used to approximate the approach in the measurement of the spatial light distribution.

## 5.2 Initial Results and Comparison

To compare the simulations to the measurements, the simulated data had to be evaluated and plotted in a similar way as the measured distributions. The spatial distribution of the exiting light was determined by filling the positions of the detected photons in a two-dimensional histogram with a bin size of $(4.65\,\mu\text{m})^2$ which represent the camera pixels in the measurements. The count of each bin then gave the light output per (pixel) area.
To achieve higher statistics and, therefore, lower uncertainties on the photon count, the light output profile along the centre of a fibre was not obtained by simply plotting the

central bin array of the corresponding spatial distribution, but it was calculated as shown and described in figure 5.3 by averaging over larger areas of the fibre end surface (set by the given symmetry) for each step along the profile.
The azimuthally integrated angular light output distribution was obtained by calculating the polar exiting angles $\delta$ from the detected photons' directions and determining the number of photons with $\delta \pm 2°$ for exiting angles between 0° and 90° in steps of 2°. This binning accounts for the angular acceptance of the the camera system used in the measurements. The uncertainties (given by the square root of the corresponding bin counts) are very small (typically 0.1%) and are therefore not shown in the plots.

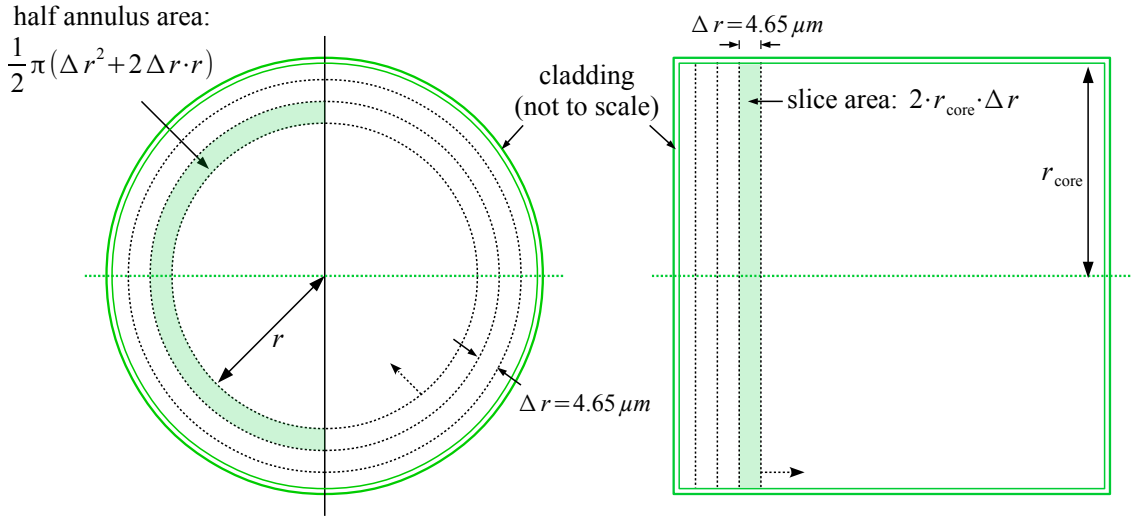


**Figure 5.3:** Schematics of how the light output profile along the fibre centre (green dotted lines) in steps of $\Delta r = 4.65\,\mu$m was calculated for round and square fibres. For each step the number of all photons detected in the corresponding half annulus (round fibres) or slice (square fibres) was determined. The square root of this number then gave the uncertainty on the photon count. The number of photons was further divided by the area of the corresponding half annulus or slice and multiplied by $\Delta r^2$ to get the average photon count per area of $(4.65\,\mu\text{m})^2$ for each segment of the profile. The uncertainties were re-calculated in the same way. This averaging could be done because round fibres show a radially symmetrical spatial distribution of the exiting photons while square fibres feature a flat distribution (see fig. 5.8). For square fibres the vertical slices only extend to the fibre core so that a different light output from the claddings parallel to the profile direction do not falsify the averaging across the fibre core or the perpendicular claddings, respectively.

In a first run the round multiclad WLS fibre was simulated. Figure 5.4 shows the simulated spatial distribution of the light output per area as well as the light output profile through the fibre centre compared to the measurement results. The dotted lines indicate the edges of the fibre core. It shows that in the case of the simulation most of the light exits at the

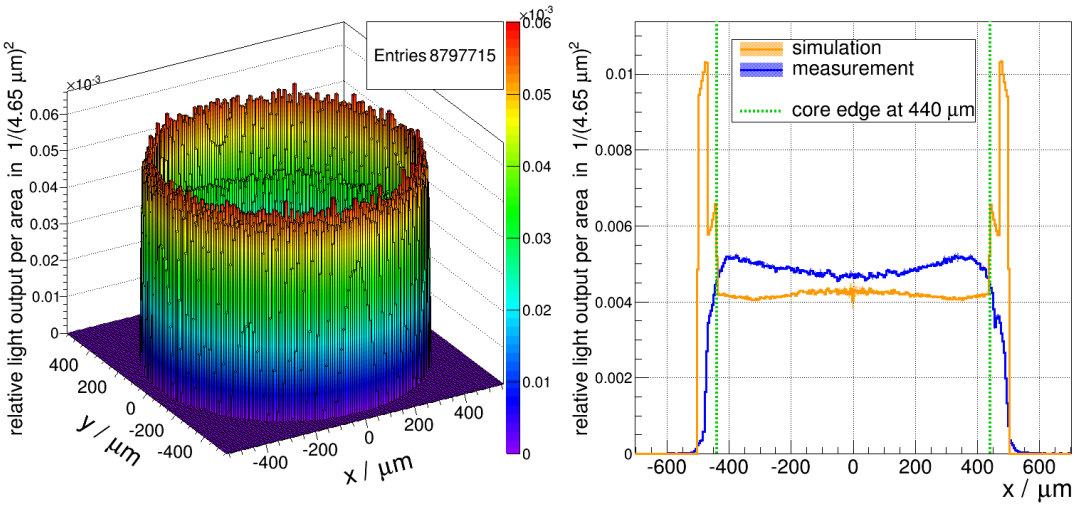


**Figure 5.4:** Left: Simulated spatial distribution of the light output (photon count) per area relative to the total photon count for the round multiclad WLS fibre (at a distance of 10 $\mu$m towards the fibre end surface). Right: The corresponding light output profile through the fibre centre for the initial simulation (orange; cf. fig. 5.3) and measurement (blue; see fig. 4.12). It shows that the profiles do not match. For the simulation, the fibre claddings feature a much higher light output per area than the fibre core.

fibre claddings. This is in strong contrast with the measurement.

A further severe difference between simulation and measurement shows in the angular light distribution. It can be seen in figure 5.5 that the maximum of the distribution is shifted to much larger exiting angles in the case of the simulation.

The differences in the angular and spatial light distribution show that in the simulation the majority of light is transported by reflections at the cladding-vacuum interface at the fibre edges. Said interface allows TIR at steeper incident angles due to the large difference between the refractive indices $n_{clad2} = 1.42$ and $n_{ambient} = 1$. This leads to larger possible exiting angles of the propagated light rays. As mentioned in section 2.3, these modes are suppressed in real fibres due to imperfections of the cladding-air interface.

In the simulation the fibre edges are perfectly smooth. Light that would leak out of a real fibre during propagation is therefore trapped inside the simulated fibre over the whole length and contributes to the obtained distributions.

For a more accurate simulation, the GODDeSS classes which represent the optical fibres and the light propagation inside them were extended to allow the possibility of adding a certain roughness to the outer interface. The following section describes how the roughness was implemented and how suitable parameters for it were determined.

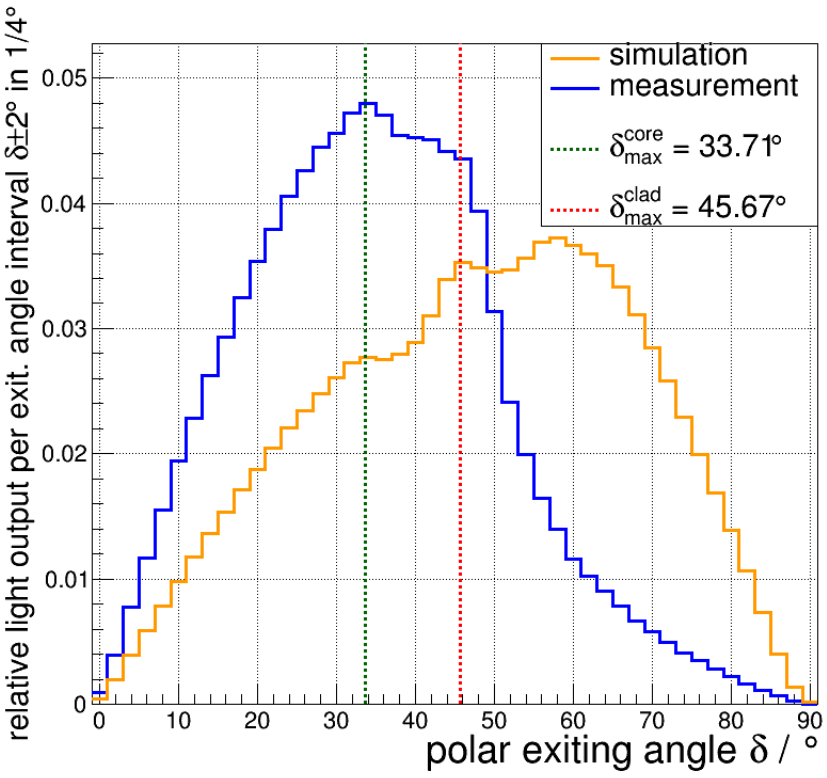


**Figure 5.5:** Comparison of the fibre light output (photon count) per polar exiting angle interval (azimuthally integrated) for the initial simulation (orange) and the measurement (blue; see fig. 4.27) of the round multiclad WLS fibre (individually normalised to the total photon count/light output). The distributions do not match. The maximal light output of the simulated fibre is at a much larger angle ($\approx 58°$) than actually measured ($\approx 34°$).

## 5.3 Implementation of the Fibre Surface Roughness

For every intersection of a photon on an interface between two media, the simulation program determines the angle between the incoming photon and the respective surface normal to calculate whether the photon is transmitted or reflected and at which outgoing angle. For a perfectly smooth fibre the surface normal is always orthogonal to the plane tangent to the fibre edge at the point of intersection. Incoming photons with the same angle of incidence are therefore always reflected (or transmitted) at a constant outgoing angle.

To simulate the roughness of the interface, the calculation of the photon intersection was modified. Namely, for each interaction of a photon with the outer surface of a fibre the orientation of the surface normal is varied. All angles contributing to the photon intersection are then calculated with respect to the varied surface normal. The incidence angle can therefore be steeper or more shallow than in the case of a smooth interface (see fig.

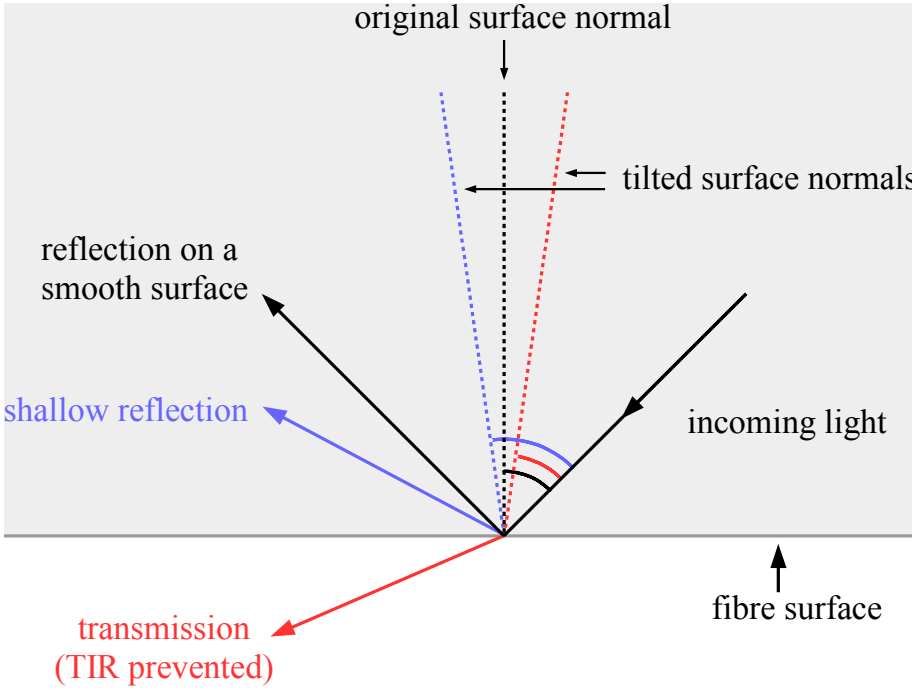


**Figure 5.6:** Schematic principle of the simulated fibre surface roughness. The original surface normal is tilted for each point of intersection of a simulated photon with the outer fibre surface. All angles are calculated towards the tilted normal which may lead to steeper incidence angles and a prevention of TIR at the cladding-air interface. On the other hand, the tilting may also lead to a more shallow reflection of the photon back into the fibre.

5.6). In the case of a steeper angle, TIR might be obstructed which simulates light leakage out of the fibre at a surface imperfection.

To get an estimation on how much and following which distribution the surface normal has to be varied for a proper simulation of the actual fibre roughness, results from [31] were considered. In that work, the surface of a plastic scintillating tile (Saint-Gobain BC-404 [32]) was analysed with the help of an atomic force microscope. It showed that for scanning resolutions of 300 nm − 600 nm the surface slope $\alpha$ deviates from the average surface following a Gaussian distribution with a mean value of $\mu_\alpha = 0°$ and a width of $\sigma_\alpha = 2.0° - 4.5°$. The scanning resolutions match the wavelength of optical photons which sets the size scale for surface imperfection to notably affect the light intersection.
Since the examined fibres are made of plastics similar to the material of the scintillator, one expects comparable properties for the roughness of the fibre surface. The Gaussian trend of the slope distribution was therefore used to simulate the fibre surface roughness. For this purpose, the orientation of the surface normal at each point of a photon intersection with the fibre surface is varied following a two-dimensional Gaussian distribution which

centres around the original surface normal. The width $\sigma_\alpha$ of the distribution is defined as the fibre surface roughness and can be set by the user. The roughness applies to photons intersecting with the fibre surface from inside the fibre as well as from the outside (i. e. photons from the simulated light source(s)).

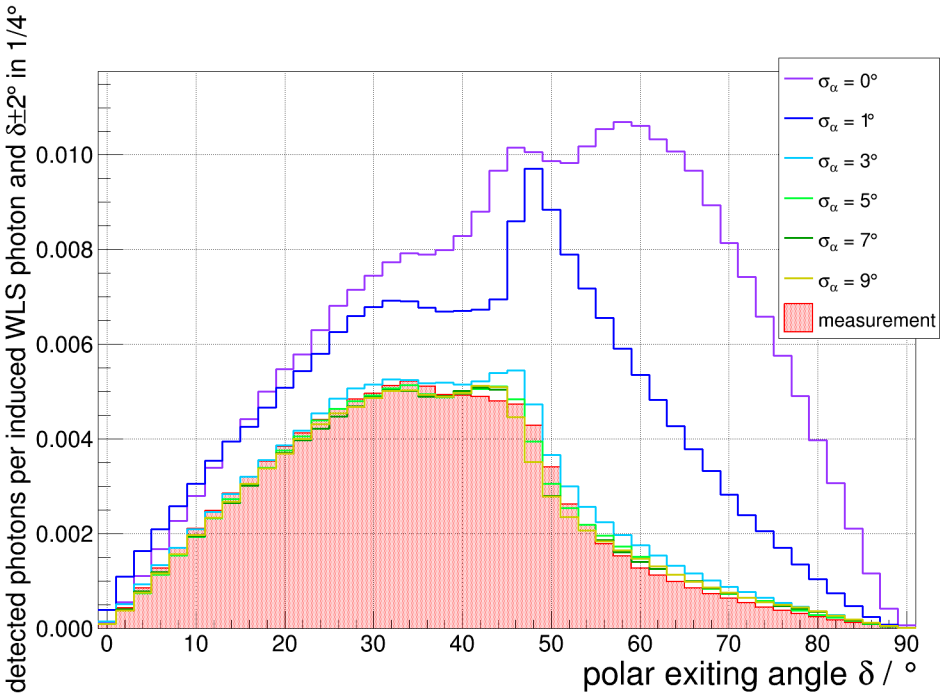


**Figure 5.7:** Comparison of the photon count per exiting angle interval (azimuthally integrated) simulated for varying values of the fibre surface roughness $\sigma_\alpha$ (fibre: round multiclad WLS). Each graph is individually normalised to the number of fluorescence photons induced into the core of the WLS fibre. The actually measured distribution (red, see fig. 4.27) is shown as well. Since the number of detected and induced photons is not known, it is scaled in a way that the integral over all exiting angles matches that of the simulated angular distribution with $\sigma_\alpha = 5°$ for comparison. For an increasing roughness the shape of the simulated distribution changes and approaches a trend similar to the measured one. For a roughness larger than 5°, the changes in the distribution's shape become minimal.

To verify the implementation of the roughness and study the effect of different values, the simulation of the round multiclad fibre was repeated with $\sigma_\alpha$ between 1° and 9° in steps of 2°. This range covers the order of magnitude of $\sigma_\alpha$ determined in [31].
Figure 5.7 shows the angular photon count distributions calculated from the simulated data sets. Each graph is individually normalised to the number of fluorescence photons induced into the core of the WLS fibre. It can be seen that for an increasing roughness the shape of the distribution changes and it approaches a trend similar to the actually

measured distribution (cf. section 4.4.2). This supports the correct modelling of the fibre roughness in the simulation program.
For a roughness larger than 5°, the changes in the angular distribution become minimal. Therefore, $\sigma_\alpha = 5°$ leads to a sufficient suppression of light reflected by the cladding-air interface and is a well working parameter for simulating the roughness of the examined fibres. This value was used in all following simulations.
The effect of the surface roughness on the light transmission is shown in table 5.1. It features the total number $N_{\mathrm{det}}$ of detected photons at the fibre end and the amount $N_{\mathrm{WLS}}$ of induced WLS photons for each examined value of the fibre surface roughness. The ratio between those numbers gives a measure for the transmission efficiency of the fibre. It can be seen that the number of WLS photons increases with the roughness, meaning that actually more light from the source is coupled into the fibre. However, the number of successfully transported and, therefore, detected photons per induced WLS photon decreases due to light losses at the cladding-vacuum interface. For a roughness of 5° the transmission efficiency is only about 38% of that of the ideal fibre.

| $\sigma_\alpha$ | $N_{\mathrm{det}}/10^6$ | $N_{\mathrm{WLS}}/10^6$ | $N_{\mathrm{det}}/N_{\mathrm{WLS}}$ |
|---|---|---|---|
| 0° | 0.44 | 3.07 | 0.143 |
| 1° | 0.32 | 3.18 | 0.101 |
| 3° | 0.20 | 3.42 | 0.058 |
| 5° | 0.20 | 3.65 | 0.055 |
| 7° | 0.21 | 3.86 | 0.054 |
| 9° | 0.22 | 4.05 | 0.054 |

**Table 5.1:** The number $N_{\mathrm{det}}$ of detected photons at the fibre end as well as the number $N_{\mathrm{WLS}}$ of WLS photons induced into a simulated round multiclad WLS fibre for different values of the fibre surface roughness $\sigma_\alpha$. The ratio between those numbers gives a measure for the transmission efficiency of the fibre. For each simulation, the same number of primary photons was generated ($20 \cdot 10^6$). While the number of induced WLS photons increases with the roughness (which also affects photons entering the fibre), the relative transmission drops. For $\sigma_\alpha = 5°$ the amount of detected photons per WLS photon is only about 38% of the ideal fibre's ratio.

## 5.4 Results and Comparison of the Updated Fibre Simulations

After adding the fibre surface roughness of $\sigma_\alpha = 5°$ to the fibre properties files, updated simulations of all three fibres were run. The determined spatial light distributions at a distance of 10 $\mu$m from the fibre end are shown in figure 5.8. The corresponding light output profiles through the fibre centre as well as the angular light distributions are compared to the measurements in the figures 5.9 to 5.11. For all fibres the simulated distributions show

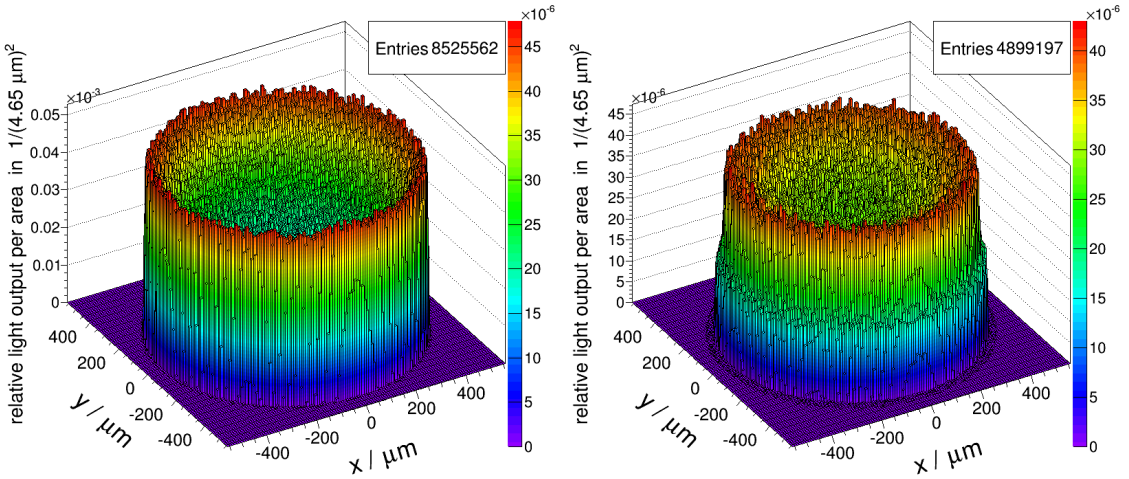


**(a)** Round singleclad light guide.

**(b)** Round multiclad WLS fibre.

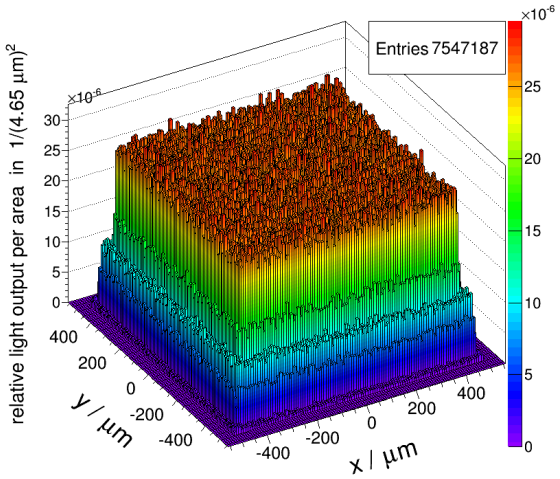


**(c)** Square multiclad scintillating fibre.

**Figure 5.8:** Simulated spatial light output distributions (given by the count of detected photons in each $(4.65\,\mu\text{m})^2$-bin relative to the total photon count) at a distance of $10\,\mu$m towards the end surface of the respective fibre. The simulated fibre edge roughness is $\sigma_\alpha = 5°$ for all three fibres.

trends similar to the measured ones.

The light output profiles of the simulated round fibres (fig. 5.9 and 5.10) feature the expected and also measured increase in light output per area towards the fibre edges. In both cases, the raise is much steeper than the measured one, but similar to the real fibres the inhomogeneity decreases for the multiclad fibre. Here, the light output per area at the edges of the singleclad fibre is about 159% higher than at the centre while the multiclad

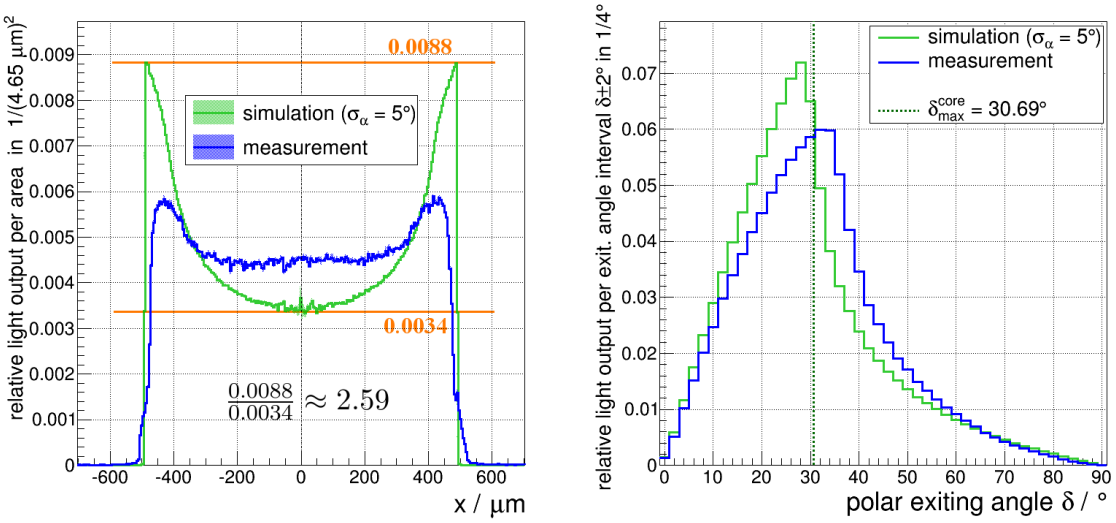


**Figure 5.9:** Comparison of the measured light exit characteristics (green) of the round singleclad fibre to the simulation with a fibre edge roughness of $\sigma_\alpha = 5°$ (blue). Left: Light output profile through the fibre centre (see fig. 4.11, 5.3) with (very small) uncertainty bands. Both simulation and measurement show an increased irradiance towards the fibre edges. For the simulation, the difference in the light output per area (approx. 159%) is much larger compared to the measurement. Right: Angular light distribution (see fig. 4.26). The distributions show a similar progression.

fibre shows an increase of approximately 45%.

To understand the difference between the simulated and measured irradiance profiles, one has to consider that the skew rays contributing to the light output closer to the fibre edges propagate at larger polar angles and are therefore reflected more often over the same length of fibre than rays with smaller polar angles. The probability to leak out of the fibre at impurities of the core-cladding or cladding-cladding interface is therefore larger for those rays in a real fibre. The simulated fibres feature ideal internal interfaces (core-cladding and cladding-cladding) and photons are therefore propagated independent from the number of reflections. Hence, more skew rays add to the increased light output towards the fibre edges. For a further improvement of the simulation, a roughness similar to the implemented fibre surface roughness has to be added to the internal interfaces. Well working parameters for this additional roughness would have to be obtained in further examinations which go beyond the scope of this thesis.

Another possible cause for the deviations between measurement and simulation could be that the simulated photons do not get absorbed or scattered at potential material imperfections as they do in the actual fibres. For the simulation this would also lead to a more efficient propagation of skew rays which travel a longer distance inside the fibre than meridional rays. Again, the examination of this possibility and a correct implementation of the fibres imperfections requires thorough investigations which could be a main topic

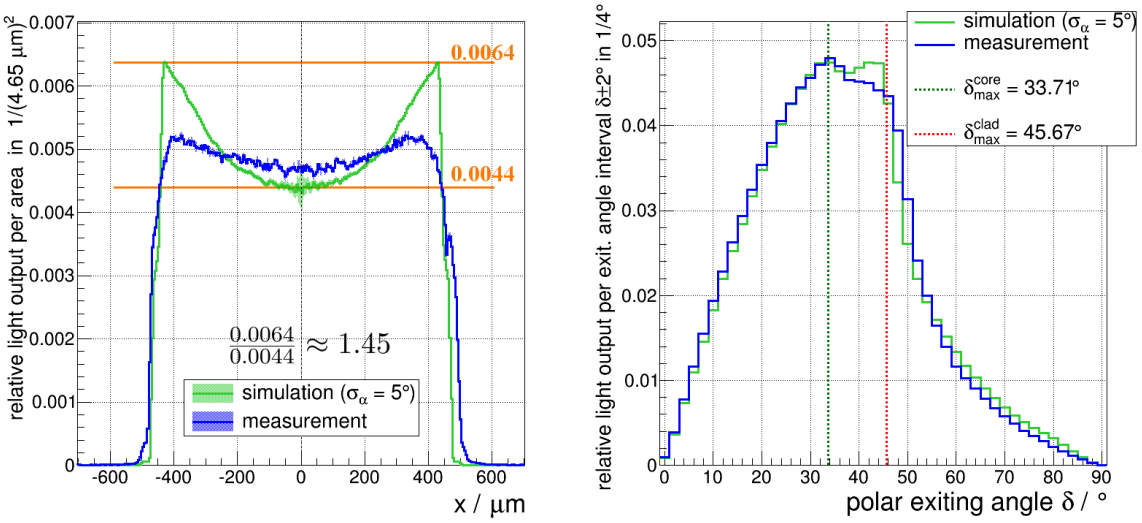


**Figure 5.10:** Comparison of the measured exit characteristics (green) of the round multiclad fibre to the simulation with a fibre edge roughness of $\sigma_\alpha = 5°$ (blue). Left: Light output profile through the fibre centre (see fig. 4.12, 5.3) with (very small) uncertainty bands. Both simulation and measurement show an increased light output per area towards the fibre edges. For the simulation, the difference in the light output (approx. 45%) is much larger compared to the measurement. Right: Angular light distribution. The simulation features a slightly higher light output for exiting angles close to $\delta_{\text{max}}^{\text{clad}}$ which shows a more efficient propagation of cladding modes than actually measured. Otherwise the distributions match to a great extent.

for a further thesis on optical fibres.

For the square multiclad fibre (fig 5.11) the simulated light output profile matches the measured results to a great extent. The light output per area fluctuates along the profile, but only little and around a constant value. Overall, the simulated fibre shows a steady light output across the fibre core similar to the real one.

Comparing the angular light distributions, it shows that in the case of the round singleclad fibre (fig 5.9) simulated and measured distribution progress rather similar. For the simulation the maximum lies at a smaller angle than the calculated acceptance angle $\delta_{\text{max}}^{\text{core}}$ even though simulated photon wavelength and refractive indices are constant in this case. As shown in fig. A.8 and A.9 in the appendix, this is due to the fibre bending but more so to the chosen binning of the angular distribution (which accounts for the angular acceptance of the camera system used in the measurements). In general, the binning shifts the position of the asymmetric maxima to smaller angles. The reason why the measured maximum does match the simulation could be a difference between the actual values of the fibre's refractive indices and those given in the specification sheet. If the true refractive

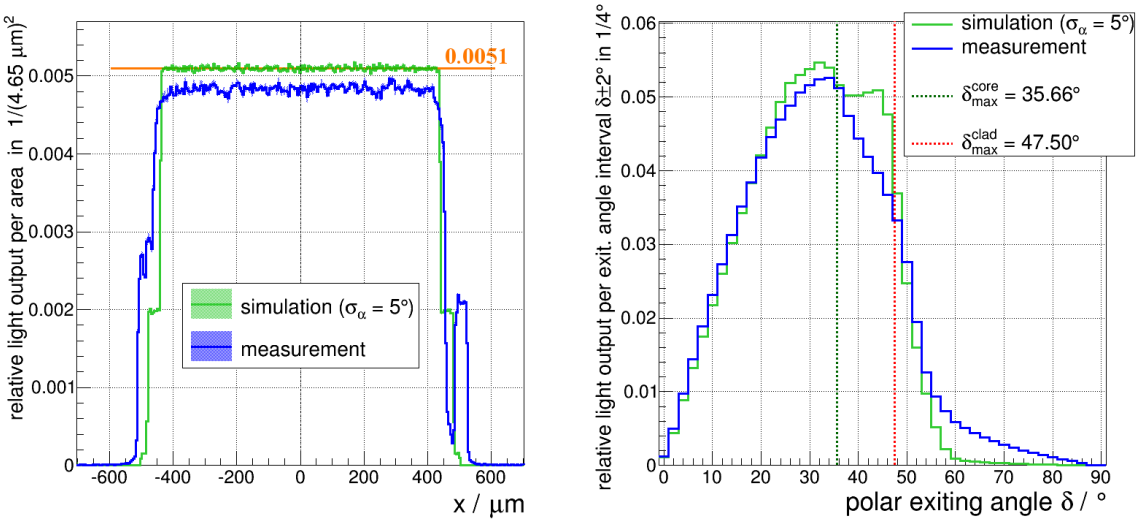


**Figure 5.11:** Comparison of the measured light exit characteristics (green) of the square multiclad fibre to the simulation with a fibre edge roughness of $\sigma_\alpha = 5°$ (blue). Left: Light output profile through the fibre centre (see fig. 4.13, 5.3) with (very small) uncertainty bands. The simulation shows a homogeneous light output across the end surface similar to the measurement. Right: Angular light distribution (see fig. 4.28). The simulation features a higher light output for exiting angles close to $\delta_{\max}^{\text{clad}}$ which shows a more efficient propagation of cladding modes than actually measured. For the simulation almost no light exits at angles larger than 60° while the measurement shows continuing exiting angles up to 90°.

index of the cladding is only 1% smaller than stated, the acceptance angle for meridional core modes increases by approx 2.5°.

The angular distributions of the simulated multiclad fibres (fig. 5.11 and 5.10) show trends comparable to the measured results as well. As can be seen, the light output for exiting angles in the vicinity of $\delta_{\max}^{\text{clad}}$ is increased in comparison to the real fibres. This shows that in the simulation cladding modes are propagated more efficiently. Again, the most plausible reason for this deviation from the measurements is the simulation of ideal internal fibre interfaces and fibre materials.

Another difference between simulation and measurement is, that in the case of the simulated square fibre almost no light exits at angles larger than 60°. The measured distribution, however, shows continuing exiting angles up to 90°. This is most likely due to differences in the shape of real and simulated fibre. Figure 5.12 shows a comparison of the respective cross sections. It can be seen that the simulated fibre features a perfectly square fibre profile whereas the actual fibre shows a rounding at the corners. This rounding might allow propagation modes and exiting angles which are prohibited in the simulation.

Additionally, damage and impurities on the fibre cladding and the end surface might increase the deviation from the simulation to some extent. At those imperfections light might

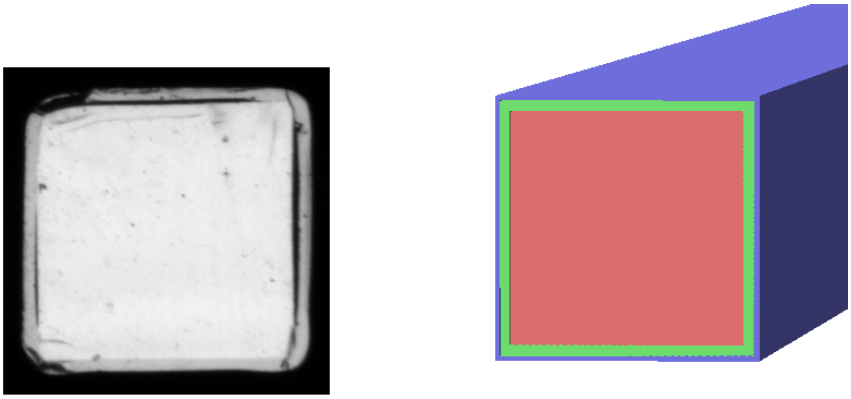

**Figure 5.12:** Left: Picture of the end surface of the square fibre. Right: Visualisation of the simulated square fibre. It shows that the real fibre has slightly rounded corners while the cross section of the simulated fibre has a perfect square shape. At this point, the GODDeSS simulation software is not yet equipped with the tools to simulate the rounding of the corners.

get deflected towards exiting angles that do not correspond to transportable light modes inside the fibre.

To compare the effect of the fibres' geometrical properties (shape and number of claddings) on the total amount of successfully propagated light, two further simulations were done including a round singleclad and a square multiclad WLS fibre (with a diameter of 1 mm) which share their materials with the already simulated round multiclad WLS fibre. The cladding thickness was set to 6% of the fibre radius for the round fibre and 8% (inner cladding) and 4% (outer cladding) for the square one. Those settings correspond to typical values for WLS fibres [13, 14]. This approach was chosen so that the same light source (LS1 in fig. 5.2) could be used in each simulation. Thus, the results do not depend on varying fibre materials or the way the light is coupled into the fibres.
For each simulation the same total amount of $N_{\text{prim}} = 500 \cdot 10^6$ primary source photons were generated. The number $N_{\text{det}}$ of detected photons on each fibre's end gives a measure of the amount of light that is successfully transported inside the given fibre and shows the differences between the varying geometries. The results of the simulations are listed and compared in table 5.2. For the used light source the round multiclad fibre transports 42% more light than the singleclad one. The square multiclad fibre shows an even higher efficiency which is 87% above the one for the round singleclad fibre. Uncertainties on the transportation efficiencies are not useful at this point since the simulated results only allow a rough estimation of the actual conditions for real fibres (as shown, the simulation still needs further improvement).
Figure 5.13 shows the simulated light exit characteristics for the three WLS fibres. The

| fibre geometry (type: WLS) | $N_{\text{prim}}/10^6$ | $N_{\text{det}}/10^6$ | $N_{\text{det}}/N_{\text{det}}^{\text{round singleclad}}$ |
|---|---|---|---|
| round singleclad | 500.00 | 3.45 | 1.00 |
| round multiclad | 500.00 | 4.90 | 1.42 |
| square multiclad | 500.00 | 6.44 | 1.87 |

**Table 5.2:** Comparison of the transported light in simulated wavelength-shifting fibres (see fig. 5.1) with different shapes and number of claddings. For each fibre the same amount $N_{\text{prim}}$ of primary photons was generated (using light source LS1 in fig. 5.2). $N_{\text{det}}$ gives the number of successfully propagated photons which got detected at the fibre end. In comparison to the singleclad fibre the round multiclad fibre transports 42% more light. The square multiclad fibre allows 87% more photons to be propagated when exposed to the same light source than the round singleclad one.

plots are not normalized so that the absolute effect of the fibre geometries can be studied. The light output profiles and angular distributions show the already discussed trends. It can be seen that the square fibre has the highest light output per area across the whole fibre profile followed by the round multiclad fibre. For exiting angles below approx. 50° the square fibre has the highest light output, too. Above that, the number of photons per exiting angle interval drops below those of the round fibres. For all exiting angles the round multiclad fibre features a higher (or equal) light output than the singleclad one.

All in all, the comparison between measured and simulated data shows that the updated GODDeSS package allows a well functioning simulation of optical fibres with varying geometries and types. They simulated spatial and angular light distributions show trends similar to the measured distributions for all examined fibres.
The differences show room for improvement for both simulation and measurement. The most profound cause for the deviations seems to be the smoothness of the simulated core-cladding and cladding-cladding interfaces and the absence of imperfections in the fibre materials. Those result in an efficient propagation of skew rays and cladding modes. In the case of the simulated round fibres, this leads to a steeper increase of the spatial light distribution towards the fibre edge. For the simulated multiclad fibres, it results in a higher light output at angles close to $\delta_{\text{max}}^{\text{clad}}$ in comparison to the measurements. Therefore, the implementation of a core and cladding roughness as well as of material imperfections could lead to a more accurate simulation. A correct implementation requires further examinations of the internal fibre interfaces and the material purity followed by the determination and fine-tuning of usable simulation parameters.
A further improvement of the simulation might be achieved if the square fibres were modelled with a slight rounding of the corners. Examining this possibility could be part of a subsequent thesis.

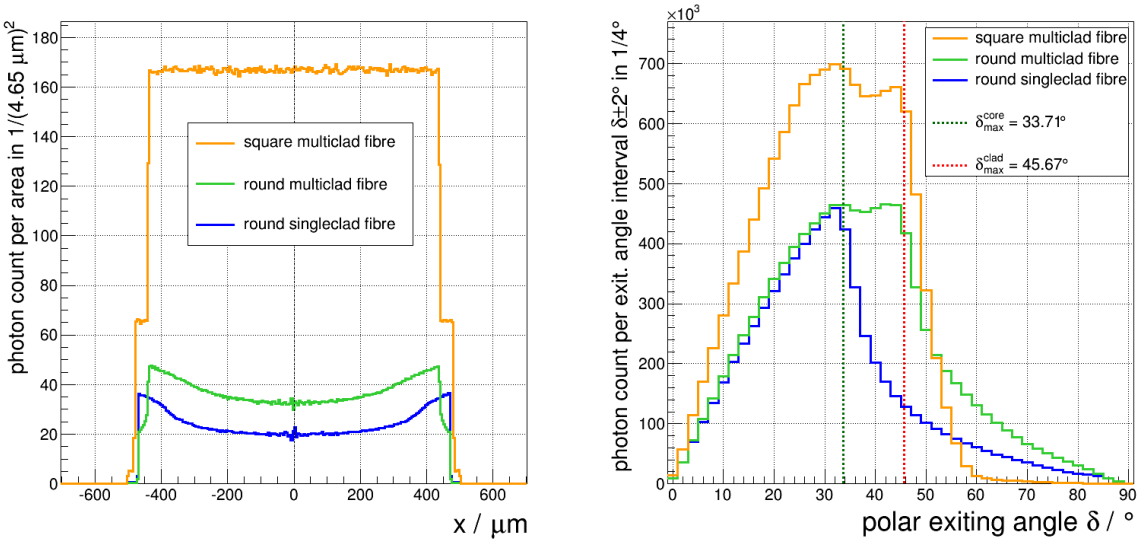


**Figure 5.13:** Absolute comparison of the light exit characteristics for three simulated WLS fibres with different shapes and number of claddings. For each fibre the same amount of primary photons was generated (see tab. 5.2). Left: Profile of the photon count per area through the fibre centre (cf. fig. 5.3). The square multiclad fibre (orange) shows the highest light output across the whole profile followed by the round multiclad fibre (green). The higher light output of the round singleclad fibre (blue) at the profile edges results from a larger fibre core (same fibre diameter but only one cladding). Right: Angular light distribution (cf. section 4.4.1). For exiting angles below approx. 50° the square fibre has the highest light output. Above that, the number of photons per (polar) exiting angle interval drops below those of the round fibres. For all exiting angles the round multiclad fibre features a higher (or equal) light output than the singleclad one.

For the conducted experiments, the deviations from the simulations show that the fibre damage inflicted during the cutting procedure influences the measurements to a measurable extent. Usable conclusions about the exit characteristics of light from optical fibres can be drawn, but a higher quality of the fibre end surfaces would result in a more accurate determination of the light exit characteristics.

The absolute comparison between three simulated fibres of the same type (WLS) but different geometries showed that a round multiclad fibre can collect and transport notably more light than a comparable round singleclad one. A square multiclad fibre has an even higher transportation efficiency.

# 6 Summary and Outlook

In the course of this thesis two experimental setups to measure the exit characteristics of light from optical fibres were developed.
One of the setups was used to examine the spatial light distribution at the fibre end surface. Minimal distances in the order of $10\,\mu$m between the observed fibre end and the readout camera sensor could be achieved. The close approach allowed the measurement of the spatial distribution with a resolution better than $5\,\mu$m set by the square pixel pitch of the used CCD sensor.
The other setup was used to obtain the distribution of the exiting angles of the fibre light. This angular distribution could be measured for all angles between 0° and 90° with an angular acceptance of 2°.

The exit characteristics were examined for three different optical multimode plastic fibres with a diameter of 1 mm: a round singleclad light guide, a round multiclad WLS fibre, and a square multiclad scintillating fibre.
It was found that for round fibres more light per area exits close to the fibre edges than it does at the centre of the end surface. The difference in light output amounts to approximately 32% for the singleclad fibre and 9% for the multiclad one. The square multiclad fibre features a uniform light distribution across the entire end surface.
The measurements of the angular light distribution showed that for all fibre types the majority of the transported light consists of core modes propagating at the maximal possible polar angle. In the case of multiclad fibres, cladding modes add to the light output at higher angles. In comparison to light transported inside the fibre core, the cladding modes are suppressed due to light losses at the core-cladding interface.
For all fibre types almost the entire propagated light ($> 99\%$) exits at angles smaller than 75°. Therefore, all examined fibres can be efficiently read out by SiPMs which feature a relative PDE above 90% for photons at those incidence angles.
The percentage of light that exits at angles smaller than the fibre's acceptance angle amounts to $(54 \pm 6)\%$ for the round singleclad fibre and $(78 \pm 4)\%$ for the multiclad one. In the case of the square multiclad fibre this percentage was measured to be $(89 \pm 3)\%$. Those results show that devices coupled to the examined types of fibre should be designed with a large enough angular acceptance to prevent a notable light loss.

The determined exit characteristics were compared to simulated data obtained with the help of the GODDeSS toolkit for the Geant4 simulation framework. The functionality

of the simulation was verified and enhanced by adding an adjustable roughness to the fibre surface. The remaining differences between measurement and simulation show that the toolkit has to be improved further by adding a roughness to the core-cladding and cladding-cladding interfaces, thus decreasing the propagation efficiency of the cladding modes. Other possible enhancements are simulating imperfections of the fibre materials and a slight rounding of the edges of simulated square fibres.
Comparing results of simulated WLS fibres with different shapes and number of claddings, it was shown that a round multiclad fibre can be used to collected and transport about 42% more light than a comparable round singleclad fibre when exposed to the same light source. Under the same circumstances, the square multiclad fibre showed an even higher transportation efficiency which is approx. 87% larger than that of the round singleclad one. The comparison also showed that the square fibre features - at least in the simulations - a lower light output than the round fibres at polar exiting angles above approx. 50°. Those results - in combination with the homogeneous spatial light output at the fibre end - renders the square multiclad fibre the best choice of the three examined fibres for experimental setups where high light collection and an efficient fibre readout (e.g. with SiPMs) is crucial.

The developed experimental setups can now be used for the examination of further types of optical fibres. Moreover, they could be used as part of an extended setup to measure additional fibre characteristics. For example, by adding a light coupling system with a calibrated light source, the effective attenuation length of different fibres could be obtained. In addition to that, light losses due to fibre bending could be determined. Another possible application is the measurement of the exit characteristics for different light sources (varying wavelength and/or coupling angles). It could also be investigated if the light exit characteristics of optical fibres could be optimized for a more efficient detector coupling by - for example - preparing a convex fibre end surface instead of the plane one examined in this thesis. This surface could work as a focal lens which decreases the maximal possible exiting angle for meridional rays and, therefore, the fibre's numerical aperture (at least for readout distances smaller than the focal length).
To improve the resolution of the angular distribution measurements, the readout system has to be modified to achieve a decreased angular acceptance. For a further enhancement of all measurements, new ways of preparing fibre end surfaces with a higher quality need to be studied.

# A Appendix A

## A.1 Emission Spectra of Light Source LEDs

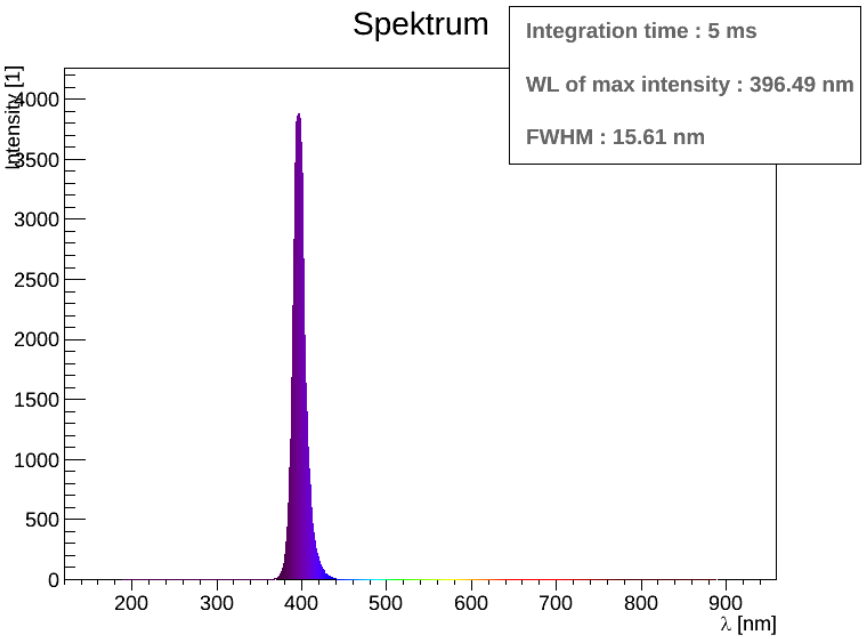


**Figure A.1:** Emission spectrum of the used UV/blue LED (in arbitrary units) with a peak wavelength of $\lambda_{\mathrm{UV}} = 396\,\mathrm{nm}$. Obtained with an Ocean Optics USB2000UV spectrometer.

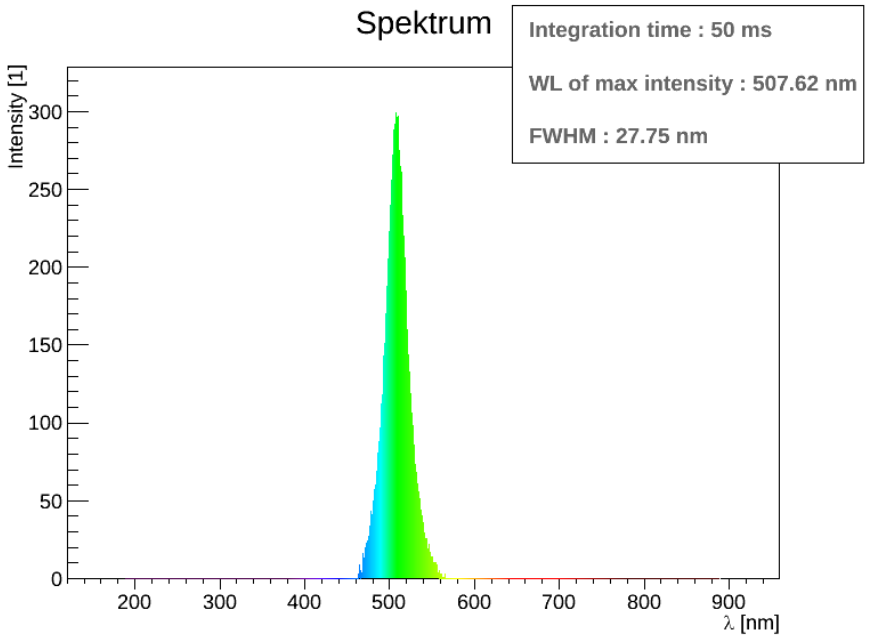


**Figure A.2:** Emission spectrum of the used green LED (in arbitrary units) with a peak wavelength of $\lambda_{\text{green}} = 508\,\text{nm}$. Obtained with an Ocean Optics USB2000UV spectrometer.

## A.2 Emission Spectra of the WLS and Scintillating Fibre

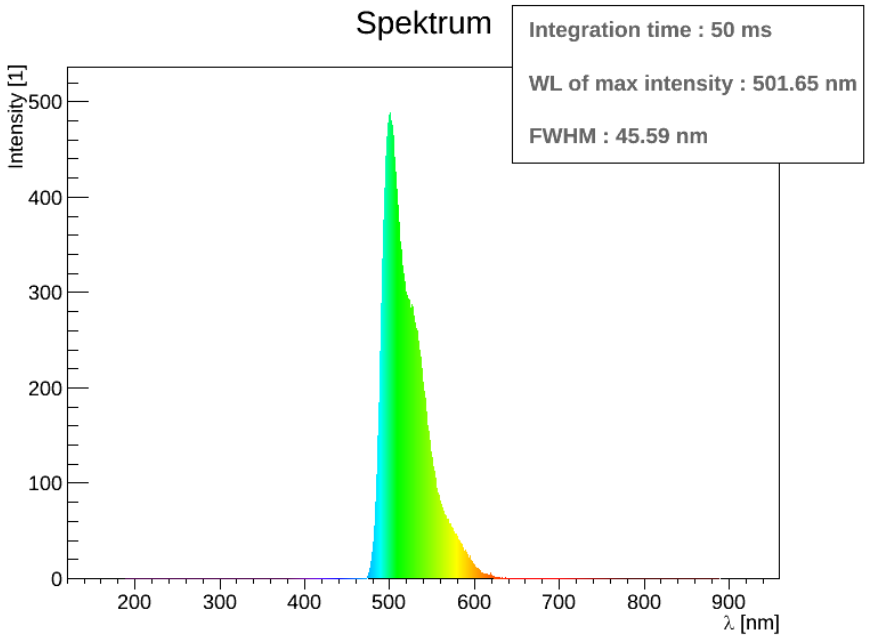


**Figure A.3:** Emission spectrum (in arbitrary units) of the examined wavelength-shifting fibre Y-11M. Obtained with an Ocean Optics USB2000UV spectrometer.

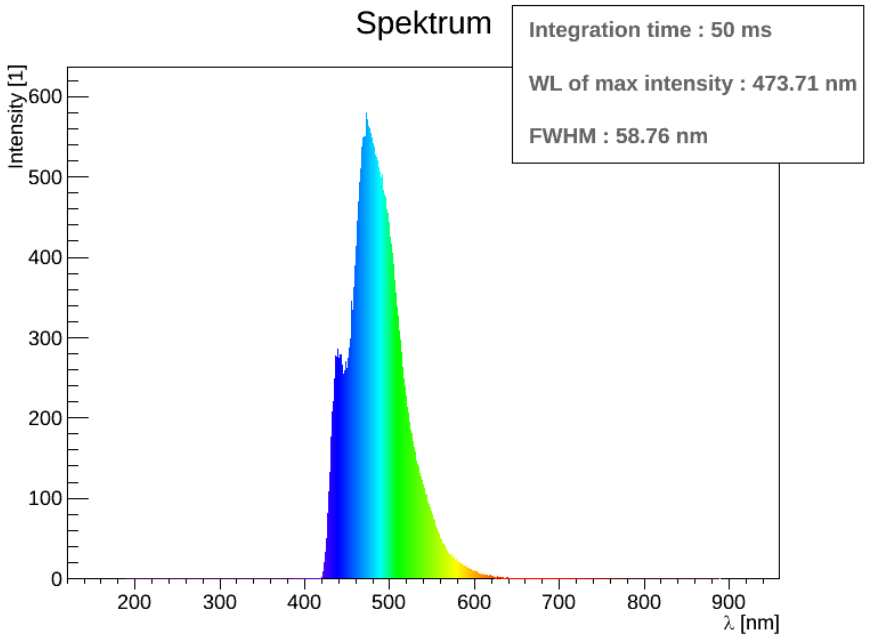


**Figure A.4:** Emission spectrum (in arbitrary units) of the examined scintillating fibre BCF-10MC. Obtained with an Ocean Optics USB2000UV spectrometer.

## A.3 Fibre Distance Determination via Shadow Cast

As described in section 3.3.1, the distance between fibre end and CCD sensor during the spatial distribution measurements is determined with the help of LED pairs which cast shadows of the approaching fibre end from different positions onto the CCD. The schematic in fig 3.6 shows how the shadow displacement $\Delta(d)$ depends on the fibre distance $d$, the position $x_\mathrm{f}$ of the illuminated fibre edge, and the vertical distances $D_1$ and $D_2$ of the LEDs from the sensor plane.
Using the theorem of intersecting lines one can calculate the positions $x_i(d)$ $(i = 1, 2)$ of the two shadow edges. It follows

$$\frac{D_i}{d} = \frac{x_i(d)}{x_i(d) - x_\mathrm{f}} \Leftrightarrow x_i(d) = x_\mathrm{f} \cdot \left( \frac{1}{1 - \frac{d}{D_i}} \right) \tag{A.1}$$

and

$$\Delta(d) = x_1(d) - x_2(d) = x_\mathrm{f} \cdot \left( \frac{1}{1 - \frac{d}{D_1}} - \frac{1}{1 - \frac{d}{D_2}} \right) \quad . \tag{A.2}$$

The Taylor series for $1/(1-x)$ at $x = 0$ is

$$\frac{1}{1-x} = 1 + x + x^2 + \mathcal{O}\left(x^3\right) \quad . \tag{A.3}$$

Therefore, one gets the following approximation for close distances between fibre and sensor in respect to the LED positions ($d \ll D_i$):

$$\Delta\left(d\right) = x_{\mathrm{f}} \cdot \left(1 + \frac{d}{D_1} + \frac{d^2}{D_1^2} + \mathcal{O}\left(\frac{d^3}{D_1^3}\right) - \left(1 + \frac{d}{D_2} + \frac{d^2}{D_2^2} + \mathcal{O}\left(\frac{d^3}{D_2^3}\right)\right)\right) \quad . \tag{A.4}$$

During the experiments, the camera approach starts at a distance of 1 mm or less while the LED distances are in the order of 1 cm. Thus, the terms $d^2/D_i^2$ (and higher orders) amount to less than 1% of the result. In a good approximation, the shadow displacement is therefore given by

$$\Delta(d) \approx x_f \cdot \left(\frac{1}{D_1} - \frac{1}{D_2}\right) \cdot d \Rightarrow \Delta(d) \propto d \tag{A.5}$$

which shows a linear progression of $\Delta\left(d\right)$ for close approaches. After several measurements of $\Delta$ at different camera positions with known step sizes, the shadow displacement can therefore be extrapolated towards $\Delta = 0$ (meaning contact between CCD and fibre end) from the results of a linear fit (cf. 4.3.1).

## A.4 Camera Sensor Response

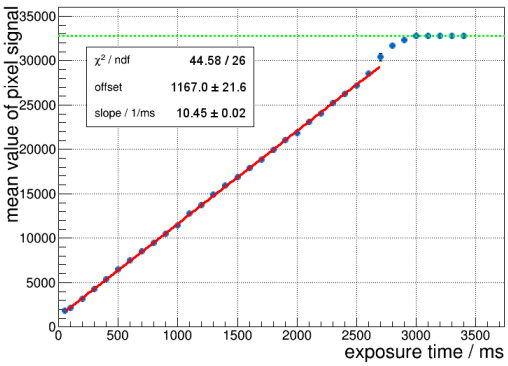


**(a)** Pixel at $(256, 384)$.

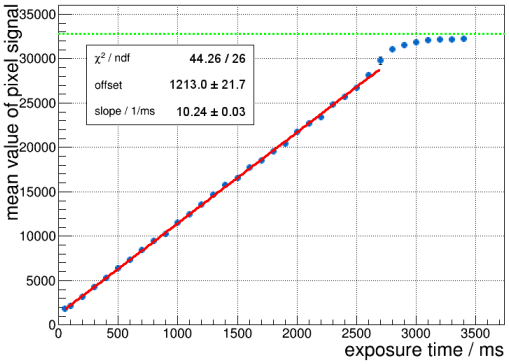


**(b)** Pixel at $(512, 192)$.

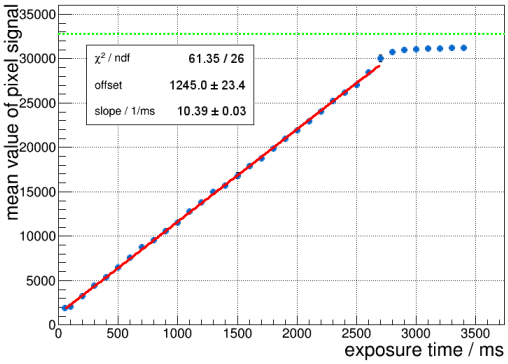


**(c)** Pixel at $(512, 576)$.

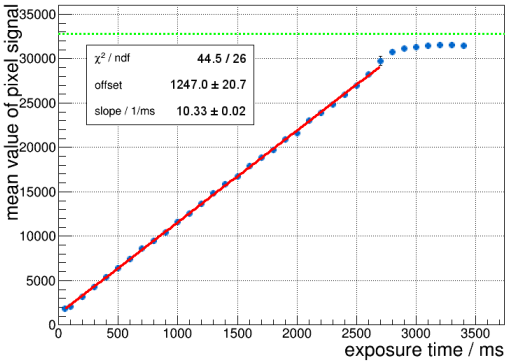


**(d)** Pixel at $(768, 384s)$.

**Figure A.5:** Sensor response measured for several pixels across the CCD sensor (see section 4.2). All examined pixels show a linear response over most part of the sensor's dynamic range. The slopes of the fitted linear functions lie in the same order of magnitude.

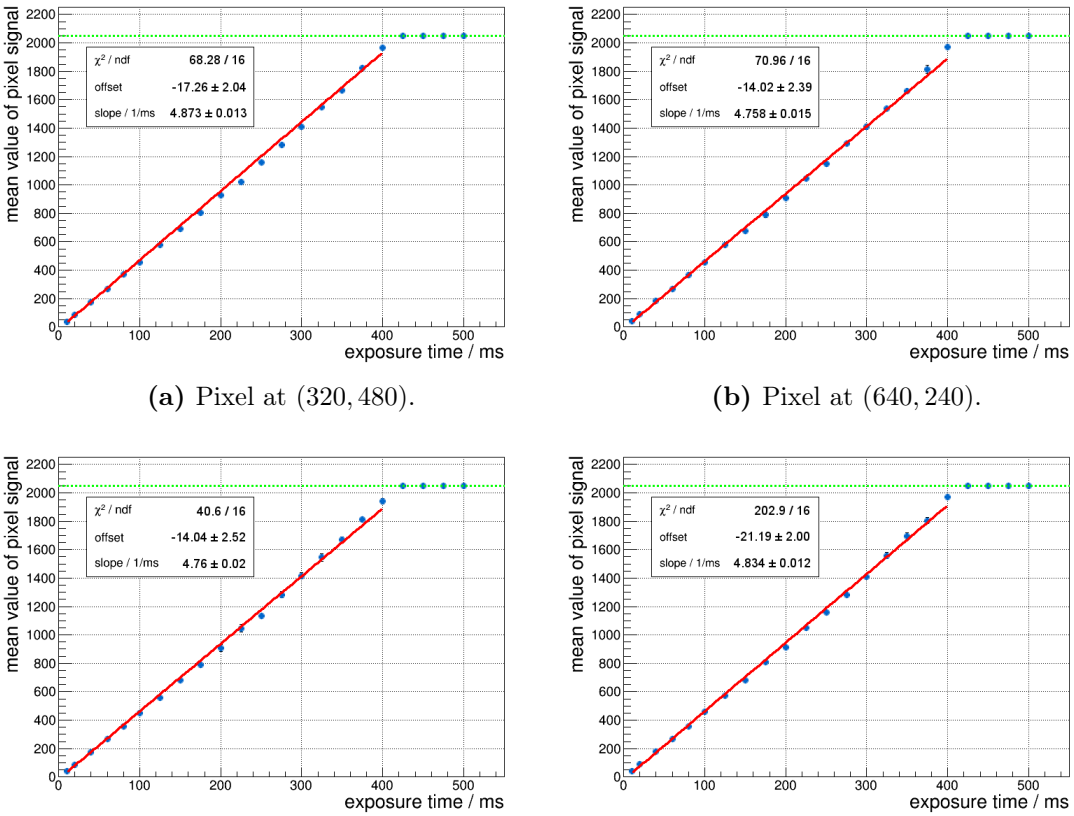


**(a)** Pixel at $(320, 480)$.

**(b)** Pixel at $(640, 240)$.

**(c)** Pixel at $(640, 720)$.

**(d)** Pixel at $(960, 480)$.

**Figure A.6:** Sensor response measured for several pixels across the CMOS sensor (see section 4.2). All examined pixels show a linear response over most part of the sensor's dynamic range. The slopes of the fitted linear functions lie in the same order of magnitude.

## A.5 Straight and Bent Fibre Simulation

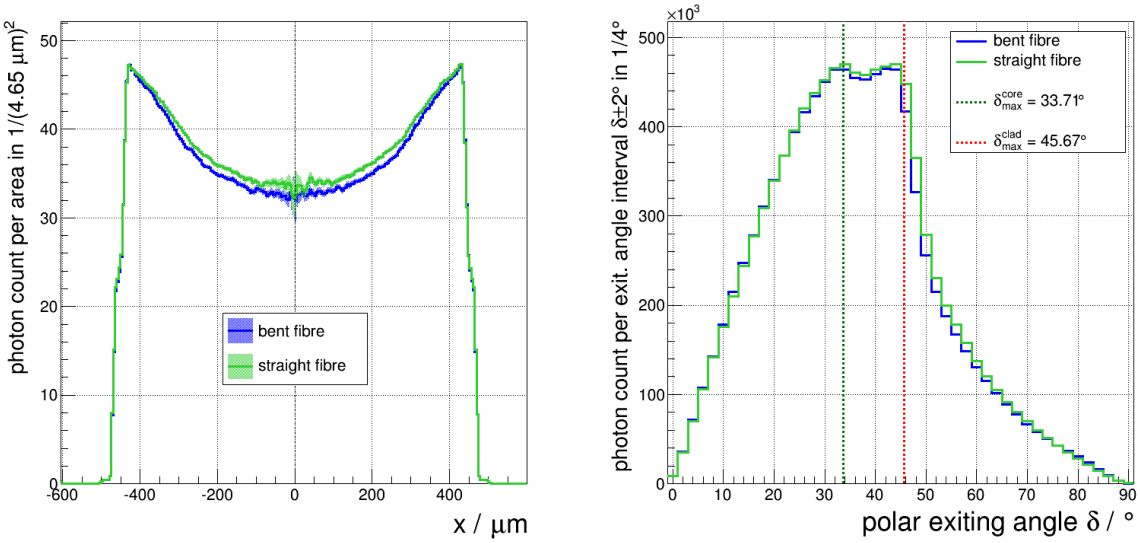


**Figure A.7:** Comparison of the simulated light exit characteristics of a bent fibre (blue; see fig. 5.1) and a perfectly straight one (green) with the same length (fibre: round multiclad WLS). Left: photon count per area of $(4.65\,\mu\text{m})^2$ along the centre of the fibres with uncertainty bands (see fig. 5.3). Right: photon count per polar exiting angle interval $\delta \pm 2°$ (azimuthally integrated; see section 4.4.1). The simulated distributions differ only slightly when compared to the deviations between simulations and measurements (presented in section 5.4).

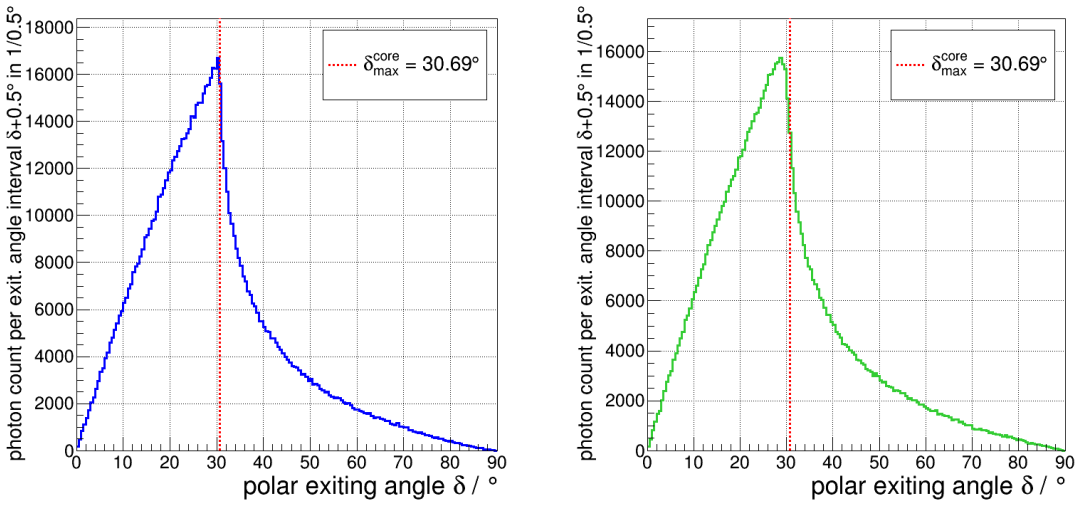


**Figure A.8:** Distribution of the polar exiting angle of light from a straight (left) and a bent (right, cf. fig. 5.1) simulated round singleclad light guide. The plots are not re-binned to simulate the angular acceptance of the camera system used in the measurement. For the straight fibre the maximum of the distribution lies at the maximal exiting angle $\delta_{\text{max}}^{\text{core}} = 30.69°$ of meridional core modes. The bent fibre shows a maximum at a smaller angle ($\approx 28.5°$). This results from possible steeper incidence angles preventing TIR at the core-cladding interface when a photon is reflected at the bent segment of the fibre.

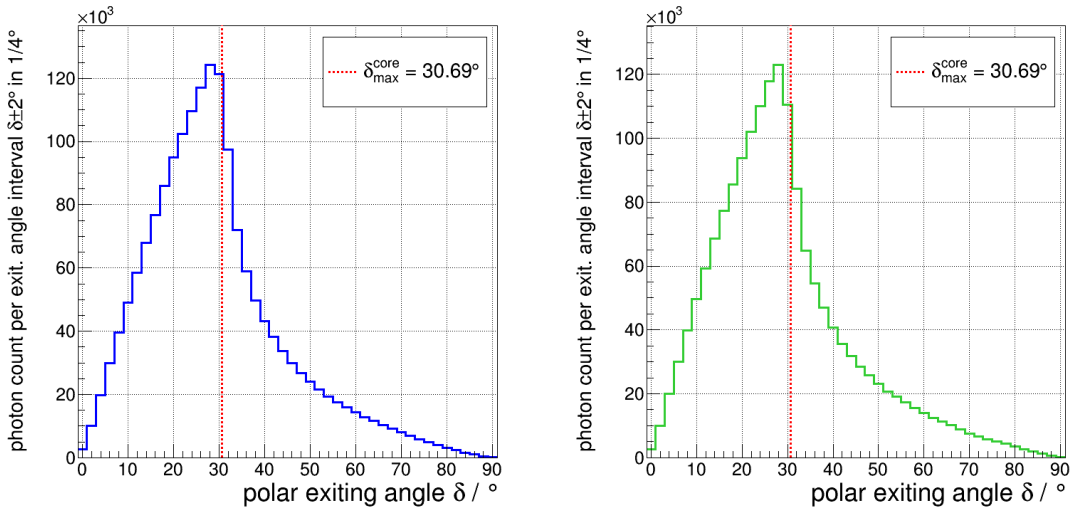


**Figure A.9:** Distribution of the polar exiting angle of light from a straight (left) and a bent (right, cf. fig. 5.1) simulated round singleclad light guide. The plots are re-binned to simulate the angular acceptance $\delta \pm 2°$ of the camera system used in the measurement. Both distributions feature a similar trend and a maximum at approx. 28° even though fig. A.8 shows that the actual maxima lie at different angles for the straight and the bent fibre. This means that the bending has an effect on the angular light output distribution of a fibre but the experimental setup is not precise enough to examine this effect closely. Knowing and simulating the exact parameters of the actual fibre bending is therefore not essential for a comparison of measured and simulated trends of the light exit characteristics.

# Bibliography


[1] C. Adloff et al. *The AMS-02 lead-scintillating fibres Electromagnetic Calorimter*. NIM A 714 147-154, 2013.

[2] S. Abdullin et al. *Design, performance, and calibration of the CMS hadron-outer calorimter*. The European Journal C 57: 653-663, 2008.

[3] Dr. rer. nat. M. Merschmeyer, F. Scheuch, M. Sc. RWTH. III. Physics Institute A, RWTH Aachen University. *Private communication*, November 2014.

[4] B. Glauß. *Optical Test Stand and SiPM characterisation studies*, master thesis, III. Phys. Inst. A, RWTH Aachen University, 2012.

[5] J. Schumacher. *Characterization Studies of Silicon Photomultipliers: Noise and Relative Photon Detection Efficiency*, bachelor thesis, III. Phys. Inst. A, RWTH Aachen University, 2011.

[6] Hamamatsu Photonics. *MPPC Technical Information*. Available online http://www.edm.ethz.ch/content/dam/ethz/special-interest/phys/particle-physics/precisionphysicsatlowenergy-dam/TeachingContent/mppc.pdf, visited 13.10.2014.

[7] D. Wilson. *Angular Dependence of the Relative Photon Detection Efficiency of Silicon Photomultipliers*, bachelor thesis, III. Phys. Inst. A, RWTH Aachen University, 2012.

[8] B. Baumbaugh et al. *Studies of the Pattern of Light Emitted from Waveshifting, Scintillating, and Waveguide Fibers Used in Detectors for Particle Physics*. IEEE Nuclear Science Symposium Conference Record, pages 847–851, 2010.

[9] S. Agostinelli et al. *Geant4 - a simulation toolkit*. Nuclear Instruments and Methods in Physics Research A506, pages 250–303, 2003.

[10] E. Dietz-Laursonn. *Detailed Studies of Light Transport in Optical Components of Particle Detectors*, doctoral thesis to be published, III. Phys. Inst. A, RWTH Aachen University, 2014.

[11] W. Demtröder. *Experimentalphysik 2 - Elektrizität und Optik*. Springer-Verlag, 3th edition, 2004.

[12] LEONI Fiber Optics GmbH. *Central Catalog: Fiber Optics*. Available online http://www.leoni-fiber-optics.com/fileadmin/bu/fo/produkte/pageflip/de/gesamtkatalog_de/downloads/livebook.pdf, visited 12.12.2014.

[13] Saint Gobain Crystals. *Technical Information: Scintillating Optical Fibres*. Available online http://www.crystals.saint-gobain.com/uploadedFiles/SG-Crystals/Documents/SGC%20Fibers%20Brochure.pdf, visited 23.11.2014.

[14] Kuraray Co., Ltd. *Specification Sheet: Plastic Optical Fibers*. Available online http://kuraraypsf.jp/psf/index.html, visited 23.11.2014.

[15] H. Leutz. *Scintillating fibres*. Nuclear Instruments and Methods in Physics Research A364, pages 422–448, 1995.

[16] T.O. White. *Scintillating Fibres*. Nuclear Instruments and Methods in Physics Research A273, pages 820–825, 1988.

[17] Particle Data Group. *The Review of Particle Physics*. Chin. Phys. C, 38, 090001. URL: http://pdg.lbl.gov/, 2014.

[18] O. Ziemann, J. Krauser, P. E. Zamzow, W. Daum. *POF Handbook - Optical Short Range Transmission Systems*. Springer-Verlag, 2nd edition, 2008.

[19] J. Zubia, J. Arrue. *Plastic Optical Fibers: An Introduction to Their Technological Processes and Applications*. Optical Fiber Technology, vol. 7, pages 101–140, 2001.

[20] R. C. Ruchti. *Performance of multiclad scintillating and waveguide optical fibers read-out with visible light photon counters*. Proc. SPIE 2007, Scintillating Fiber Technology and Applications, pages 101–140, 1993.

[21] Astrolumina. *Technical Information: CCD Camera ALccd IMG0S-M*. Available online http://www.astrolumina.de/kamerasysteme/alccd-qhy/img/alccd-img0s-1.php, visited 23.11.2014.

[22] Sony. *Specification Sheet: CCD Sensor ICX204AL*. Available online http://www.eureca.de/pdf/optoelectronic/sony/ICX204AL.PDF, visited 23.11.2014.

[23] QHYCCD. *EZPlanetary - Planetary Video and Image Capturing Software*. Available online http://qhyccd.com/en/top/manual/ezplanetary/, visited 23.11.2014.

[24] Newport. *Specification Sheet: Piezo-Driven Linear Stage CONEX-AG-LS25-27P*. Available online http://assets.newport.com/webDocuments-EN/images/CONEX-AG-LS25-27P_Data_Sheet_MC.pdf, visited 23.11.2014.

[25] QHYCCD. *Specification Sheet: CMOS Camera QHY5L-IIm*. Available online http://qhyccd.com/en/left/page3/qhy5-ii-series/, visited 23.11.2014.

[26] Aptina. *Specification Sheet: CMOS Sensor MT9M034*. Available online http://ghgtechn.com/admin/upload/634912822373126250MT9M034_DS_B.pdf, visited 23.11.2014.

[27] Edmund Optics. *Specification Sheet: Light-Guiding Fibre*. Available online http://www.edmundoptics.de/optics/fiber-optics/optical-grade-fiber-optics/02534, visited 23.11.2014.

[28] Dipl.-Phys. O. Fitzau. Fraunhofer-Institut für Lasertechnik ILT. *Private communication*, September 2014.

[29] Dr.-Ing. A. Olowinsky. Fraunhofer-Institut für Lasertechnik ILT. *Private communication*, April 2014.

[30] RefractiveIndex.INFO. *Online refractive index database*. URL: http://refractiveindex.info, visited 23.11.2014.

[31] P. Papacz. *Optimisation of the Particle Detection Efficiency for Scintillation Detectors with SiPM Readout*, diploma thesis, III. Phys. Inst. A, RWTH Aachen University, 2010.

[32] Saint Gobain Crystals. *Technical Information:Organic Scintillation Materials*. Available online http://www.crystals.saint-gobain.com/uploadedFiles/SG-Crystals/Documents/SGC%20Organics%20Brochure.pdf, visited 23.11.2014.

## Acknowledgements - Danksagung

Hiermit möchte ich mich bei allen Leuten bedanken, die mir das Erstellen dieser Arbeit ermöglicht haben. Da ich hier nicht alle helfenden Personen namentlich aufführen kann, sei an dieser Stelle mein Dank gegenüber denjenigen Leuten ausgedrückt, die hier nicht erwähnt werden.
Besonderer Dank geht an Herrn Prof. Dr. Thomas Hebbeker, dafür, dass er mir die Möglichkeit gegeben hat, meine Masterarbeit an seinem Institut anzufertigen, und an Herrn Dr. Oliver Pooth, der sich für die Erstellung des Zweigutachtens bereit erklärt hat.
Des Weiteren bedanke ich mich bei meinem Betreuer Herrn Dr. Markus Merschmeyer, der mir von Anfang an sowohl bei der Entwicklung und Duchführung der Experimente, als auch beim Schreiben der Arbeit jederzeit hilfreich zur Seite stand und auch bei mehrmaligem Erklären eines Sachverhalts nie die Geduld verlor.
Weiterhin geht mein Dank an Erik Dietz-Laursonn, mit dem ich im Rahmen der Faser-Simulationen eng zusammengearbeitet habe, und an Carsten Heidemann, der stets für jegliche Fragen offen war und mir mit der Erstellung von auomatisierten Bild-Aufnahmeprogrammen für die Versuchsreihen sehr geholfen hat.
Für das Bereitstellen der untersuchten optischen Fasern sei hiermit Herrn Georg Schwering vom I. Physikalischen Institut B gedankt.
Bedanken möchte ich mich auch bei allen Mitarbeitern der CMS-Arbeitsgruppe, die immer bereit waren, Fragestellungen zu den verschiedensten Themen zu diskutieren. Diese Personen einschließend geht mein Dank auch an alle anderen Büropartner und -nachbarn, die mir die Zeit am Institut durch ihre offene und freundliche Art sehr angenehm gestaltet haben und die immer für Fragen aller Art bereitstanden.
Repräsentativ für die Mitarbeiter der mechanischen und der elektronischen Werkstatt, möchte ich mich bei Herrn Philipps und Herrn Frohn sowie bei Herrn Zantis und Herrn Adamczyk bedanken, ohne deren Hilfe und Beratung die Realisierung der Versuchsaufbauten nicht möglich gewesen wäre.
Für das Korrekturlesen meiner Arbeit danke ich noch einmal Herrn Prof. Dr. Thomas Hebbeker, Herrn Dr. Markus Merschmeyer und Carsten Heidemann.
Abschließend bedanke ich mich bei meiner Familie und meinen Freunden für die mentale Unterstützung während der sehr lehrreichen und interessanten aber manchmal auch sehr stressigen Zeit des vergangenen Jahres.

# Erklärung

Hiermit versichere ich, dass ich diese Arbeit einschließlich beigefügter Darstellungen und Tabellen selbstständig angfertigt und keine anderen als die angegebenen Hilfsmittel und Quellen verwendet habe. Alle Stellen, die dem Wortlaut oder dem Sinn nach anderen Werken entnommen sind, habe ich in jedem Fall unter genauer Angabe der Quellen deutlich als Entlehnung kenntlich gemacht.
Aachen, Dezember 2014

**Simon Nieswand**